PASJ: Publ. Astron. Soc. Japan **62**, 811–870, 2010 June 25

LoCuSS: Subaru Weak Lensing Study of 30 Galaxy Clusters*

Nobuhiro OKABE,[1,3] Masahiro TAKADA,[2] Keiichi UMETSU,[3,4] Toshifumi FUTAMASE,[1] and Graham P. SMITH [5]
[1]*Astronomical Institute, Tohoku University, Aramaki, Aoba-ku, Sendai 980-8578*
okabe@astr.tohoku.ac.jp
[2]*Institute for the Physics and Mathematics of the Universe (IPMU)*
The University of Tokyo, 5-1-5 Kashiwa-no-Ha, Kashiwa City, Chiba 277-8582
[3]*Academia Sinica Institute of Astronomy and Astrophysics (ASIAA), P.O. Box 23-141, Taipei 10617, Taiwan*
[4]*Leung Center for Cosmology and Particle Astrophysics, National Taiwan University, Taipei 10617, Taiwan*
[5]*School of Physics and Astronomy, University of Birmingham, Edgbaston, Birmingham, B15 2TT, UK*

(Received 2009 February 24; accepted 2010 April 16)

Abstract

We use high-quality Subaru/Suprime-Cam imaging data to conduct a detailed weak lensing study of the distribution of dark matter in a sample of 30 X-ray luminous galaxy clusters at $0.15 \leq z \leq 0.3$. A weak lensing signal is detected at high statistical significance in each cluster, the total signal-to-noise ratio of the detections ranging from 5 to 13. Comparing spherical models to the tangential distortion profiles of the clusters individually, we are unable to discriminate statistically between a singular isothermal sphere (SIS) and Navarro, Frenk, and White (NFW) models. However, when the tangential distortion profiles are combined and then models are fitted to the stacked profile, the SIS model is rejected at 6σ and 11σ, respectively, for low ($M_{\rm vir} < 6 \times 10^{14} h^{-1} M_\odot$) and high ($M_{\rm vir} > 6 \times 10^{14} h^{-1} M_\odot$) mass bins. We also used individual cluster NFW model fits to investigate the relationship between the cluster mass and the concentration, finding that the concentration ($c_{\rm vir}$) decreases with increasing cluster mass ($M_{\rm vir}$). The best-fit $c_{\rm vir}$–$M_{\rm vir}$ relation is: $c_{\rm vir}(M_{\rm vir}) = 8.75^{+4.13}_{-2.89} \times (M_{\rm vir}/10^{14} h^{-1} M_\odot)^{-\alpha}$ with $\alpha \approx 0.40 \pm 0.19$: i.e., a non-zero slope is detected at 2σ significance. This relation gives a concentration of $c_{\rm vir} = 3.48^{+1.65}_{-1.15}$ for clusters with $M_{\rm vir} = 10^{15} h^{-1} M_\odot$, which is inconsistent at 4σ significance with the values of $c_{\rm vir} \sim 10$ reported for strong-lensing-selected clusters. We have found that the measurement error on the cluster mass is smaller at higher over-densities, $\Delta \simeq 500$–2000, than at the virial over-density, $\Delta_{\rm vir} \simeq 110$; typical fractional errors at $\Delta \simeq 500$–2000 are improved to $\sigma(M_\Delta)/M_\Delta \simeq 0.1$–$0.2$ compared with 0.2–0.3 at $\Delta_{\rm vir}$. Furthermore, comparing the 3D spherical mass with the 2D cylinder mass, obtained from the aperture mass method at a given aperture radius, θ_Δ, reveals $M_{\rm 2D}(< \theta_\Delta)/M_{\rm 3D}(< r_\Delta = D_{\rm l}\theta_\Delta) \simeq 1.46$ and 1.32 for $\Delta = 500$ and $\Delta_{\rm vir}$, respectively. The amplitude of this offset agrees well with that predicted by integrating an NFW model of cluster-scale halos along the line-of-sight.

Key words: cosmology: observations — dark matter — galaxies: clusters — gravitational lensing

1. Introduction

The mass and internal structure of galaxy clusters reflect the properties of primordial density perturbations and the nature of dark matter. A most striking prediction from numerical simulations based on the cold dark matter (CDM) model of structure formation is that dark matter halos can be described by a universal mass density profile, as found by Navarro, Frenk, and White (1996, 1997, hereafter NFW; also see Moore et al. 1999; Fukushige & Makino 2001; most recently Navarro et al. 2010 and references therein). These results have shown that cluster-scale halos should have relatively shallow, low-concentration mass profiles, where the power-law slope of the density profile becomes more negative with increasing radius, approaching an asymptotic slope of -3 around the virial radius. The dark matter halo mass function, of which galaxy clusters represent the high mass tail, is also sensitive to cosmological parameters, including for example the dark energy equation of state parameter, w (e.g., White et al. 1993; Kitayama & Suto 1997; Haiman et al. 2001; Vikhlinin et al. 2009b). Testing predictions from numerical dark matter simulations and probing dark energy require precise measurements of galaxy cluster masses; however, it is non-trivial to define what is meant by the mass of a cluster, because clusters do not have any clear boundary between themselves and the surrounding large-scale structure. By convention, the cluster mass is therefore defined as the mass enclosed within a three-dimensional sphere of a given radius with respect to the halo center, such as the virial mass (e.g., White 2002). Given a working definition of mass, a method of mass measurement must be chosen, each of which suffers a number of advantages and disadvantages, as discussed below.

The deep potential well of a galaxy cluster causes weak shape distortions of background galaxy images due to differential deflection of light rays, resulting in a coherent distortion pattern around the cluster center, known as weak gravitational lensing (Narayan & Bartelmann 1996; Bartelmann & Schneider 2001; Schneider 2006). Measuring this coherent distortion pattern allows us to directly map the mass distribution in a cluster without requiring any assumptions on the dynamical/physical state of the system (e.g., Kaiser

* Based in part on data collected at Subaru Telescope and obtained from the SMOKA, which is operated by the Astronomy Data Center, National Astronomical Observatory of Japan.

& Squires 1993; Fahlman et al. 1994). Other methods rest on some assumptions: the velocity dispersion of the member galaxies invokes as assumptions on the velocity anisotropies, dynamical equilibrium of the cluster, and the geometry of the system. Methods based on observations of X-rays and the Sunyaev–Zel'dovich (SZ) effect usually rest on assumptions of hydrostatic equilibrium and spherical symmetry. However, lensing-based methods also suffer several limitations. First, lensing observables are sensitive to the total mass distribution projected along the line of sight from an observer to the source galaxies. Therefore, mass concentrations along the line of sight through a given cluster, which are not physically associated with the cluster, increase the uncertainty on cluster mass measurements from the lensing observables (Metzler et al. 2001; White & Kochanek 2001; Hoekstra 2001; Hamana et al. 2004). Second, exhaustive spectroscopic redshift information is not available for cluster lensing observations. The limited information on source galaxy redshifts derived from the available broad-band photometry results in degeneracies between the cluster parameters and the estimated source galaxy redshifts. Furthermore, in practice it is not straightforward to isolate the background; lensed galaxies are based on photometric data alone. In fact, including unlensed galaxies (mostly cluster members for low-z clusters of interest) into the lensing analysis appears to cause a significant dilution of the lensing distortion signals, thereby yielding biased estimations on the cluster parameters (e.g., Broadhurst et al. 2005; Medezinski et al. 2007; Limousin et al. 2007; Hoekstra 2007; Umetsu & Broadhurst 2008).

Recently, a possible tension between the CDM model predictions and the lensing observations has been reported: anomalously high concentration parameter estimates have been obtained for A 1689, Cl 0024, and MS 2137 (Gavazzi et al. 2003; Kneib et al. 2003; Broadhurst et al. 2005, 2008; Oguri et al. 2009). However, before a serious problem with CDM may be claimed, it is important (among other things) to carefully address the selection bias inherent in studying strong lensing clusters. Specifically, strong lensing clusters are likely to be biased towards clusters with high concentrations and/or a significantly non-spherical mass distributions (e.g., Oguri et al. 2005; Hennawi et al. 2007; Corless et al. 2009). A systematic weak lensing study of a large cluster sample is therefore an essential step towards resolving, or confirming, this tension. An important aspect of such a study is to minimize possible selection biases towards clusters with simpler (presumably "relaxed") or more complex (presumably "unrelaxed") gravitational potentials. A selection function that is blind to such factors would support an increased understanding of possible biases in cluster mass estimates as a function of the dynamical state and shape of clusters (Dahle et al. 2002; Smith et al. 2005; Clowe et al. 2006; Bardeau et al. 2007; Hoekstra 2007; Okabe & Umetsu 2008).

Such a systematic weak lensing study would also be invaluable as the foundation for a careful comparison of lensing-based mass estimates with those from other methods, en route to measuring precisely the shape, scatter, and normalization of mass-observable scaling relations and to calibrating the systematic errors inherent in each mass measurement method (Smith et al. 2003, 2005; Hicks et al. 2006; Zhang et al. 2006, 2007, 2008; Mahdavi et al. 2008; Miyazaki et al. 2007; Hamana et al. 2008; Vikhlinin et al. 2009a; Henry et al. 2009; Bergé et al. 2008; Umetsu et al. 2009). In particular, well-calibrated mass-observable scaling relations are critically important for the use of cluster counting experiments to constrain the nature of dark energy (e.g., Lima & Hu 2005). Such studies are complementary to the cross-correlation method of background galaxy shapes around clusters binned on cluster richness, X-ray luminosity, etc. — the so-called stacked lens (Mandelbaum et al. 2008; Sheldon et al. 2009a, 2009b; Johnston et al. 2007), where the average properties of cluster mass profiles as well as the average mass-observable relation can be obtained, but information on individual clusters is lost.

In this paper, we use Subaru/Suprime-Cam observations of 30 galaxy clusters at $0.15 \leq z \leq 0.3$ to study in detail the dark matter density profile of the clusters. These clusters are a sub-set of those studied by the Local Cluster Substructure Survey (LoCuSS) project[1] (PI: G. P. Smith; also see G. P. Smith et al. in preparation), and have therefore been selected in a manner blind to the dynamical status and cluster morphology — see section 2 for more details. The superb image quality, wide-field capability, and 8-m aperture of Subaru/Suprime-Cam (Miyazaki et al. 2002) allow us to investigate in detail the accuracy achievable on cluster mass measurements with ground-based weak lensing data. It is also important to note that the redshift range of the clusters in this study is well-matched to the field-of-view of Suprime-Cam (about one-quarter square degrees) — one pointing spans the entire virialized region of each cluster (cluster-centric radii of ~ 1–$2\,r_{\rm vir}$), which is essential to achieve robust constraints on cluster virial masses. We explore different methods of cluster mass estimation, specifically the fitting of several different parametric mass profiles and the model-independent lensing aperture mass method. We discuss the pros and cons of each method, and compare the results quantitatively. We also identify the optimal radial scale at which to measure cluster masses with weak lensing data. In studying all of these issues, we pay particular attention to possible systematic errors inherent in the lensing methods. Most importantly, we demonstrate the importance of correcting for dilution of the lensing signal by faint cluster galaxies when seeking to measure robustly cluster mass and concentration.

The structure of this paper is as follows. We describe the details of our cluster sample and lensing analysis in section 2, and define background galaxy samples to use for the lensing analysis in section 3. After describing our methods to estimate cluster parameters from the lensing observables in section 4, we present the main results in section 5. Section 6 is devoted to a summary and a discussion of our findings. To improve the readability of the paper for the non-lensing expert, several technical discussions are presented in the appendices; for example, appendix 1 describes details of how the background galaxy samples are defined based on the available broad-band photometry. We also present the two-dimensional mass maps and distortion profiles of all the clusters in appendix 3. Throughout this paper we will assume a concordance ΛCDM model that is specified by $\Omega_{m0} = 0.27$, $\Omega_\Lambda = 0.73$, and

[1] ⟨http://www.sr.bham.ac.uk/locuss⟩.

$H_0 = 72.0\,\mathrm{km\,s^{-1}\,Mpc^{-1}}$ (Komatsu et al. 2009).

2. Cluster Sample and Data Analysis

2.1. LoCuSS

The Local Cluster Substructure Survey (LoCuSS: G. P. Smith et al. in preparation; also see Zhang et al. 2008) is a systematic multi-wavelength survey of X-ray luminous clusters ($L_X[0.1\text{–}2.4\,\mathrm{keV}] \gtrsim 2 \times 10^{44}\,\mathrm{erg\,s^{-1}}$) at redshifts of $0.15 \leq z \leq 0.3$ and declinations of $-70° \leq \delta \leq +70°$, selected from the ROSAT All Sky Survey (RASS: Ebeling et al. 1998, 2000; Böhringer et al. 2000, 2004). The LoCuSS selection function is deliberately blind to the physical properties of clusters, other than the requirement to be bright enough in the X-ray band to lie above the RASS flux limit. The sample is therefore expected to span a broad range of dynamical stages of cluster evolution, including extreme merger and extreme "relaxed" systems. One of the main goals of the survey is to calibrate mass-observable scaling relations, and to identify the main astrophysical systematic uncertainties in the use of these relations for cluster cosmology, in a similar vein to Smith et al.'s (2003) preliminary results on σ_8. The Subaru data presented in this paper form the backbone of the scaling relation aspects of the survey. More generally, studies of the LoCuSS sample are in progress combining data from a wide range of ground-based (Gemini, Keck, VLT, Subaru, SZA, Palomar, MMT, NOAO, and UKIRT) and space-based (HST, GALEX, Spitzer, Chandra, and XMM-Newton) facilities.

The Subaru prime focus camera, Suprime-Cam (Miyazaki et al. 2002), has the widest field-of-view (FoV) ($27' \times 34'$) among 8-m class telescopes, and can cover the entire region of a cluster at a low redshift of $z \simeq 0.2$ (up to a few megaparsecs in radius) with one pointing. The large telescope aperture, wide FoV, and superb image quality of Subaru/Suprime-Cam therefore mean that this is a uniquely powerful facility for an efficient ground-based weak lensing study of a large sample of low redshift galaxy clusters.

2.2. Sample and Observations

Clusters at declinations of $-20° \leq \delta \leq +60°$ are observable with Subaru at sufficiently high elevations ($\gtrsim 50°$) to ensure that high quality data suitable for faint galaxy shape measurements can be obtained. Through an open use program (S05B, S06A, and S07A; PI: T. Futamase) we collected Suprime-Cam data for 20 clusters, selected solely on the observability on the allocated observing nights. We also added 10 cluster data from the Subaru archive (SMOKA: Baba et al. 2002). In total we study 30 clusters, as described in this paper.

Figure 1 shows our cluster sample in the $L_X/E(z)^{2.7}$–redshift plane, where the vertical axis is plotted in units of $L_X/E(z)^{2.7}$ [$E(z)$ is the normalized Hubble expansion rate at redshift z: $E(z) \equiv H(z)/H_0$]. Note that the vertical axis roughly scales with cluster masses as $L_X/E(z)^{2.7} \propto M$, as studied in Popesso et al. (2005). The L_X distribution of our cluster sample appears to be similar to that of an X-ray luminosity limited sample with $L_X/E(z)^{2.7} \gtrsim 4.2 \times 10^{44}\,\mathrm{erg\,s^{-1}}$ (figure 1). To test this quantitatively, we drew 3000 random samples of 29 clusters[2] from the parent sample

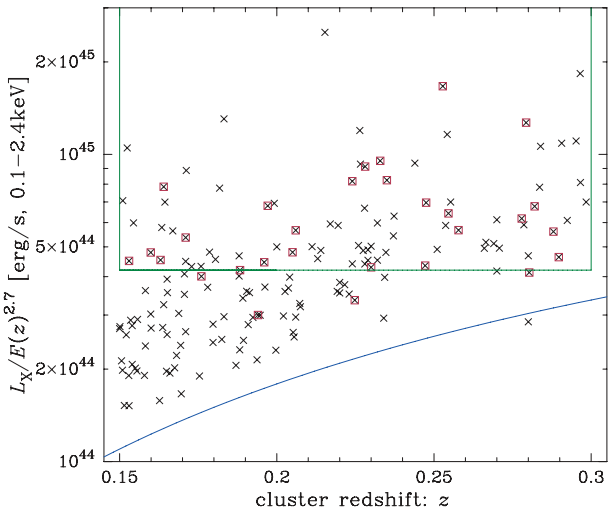

Fig. 1. Open square symbols denote the cluster sample studied in this paper in the 2D plane of the ROSAT X-ray luminosity and cluster redshift, while the cross symbols show all samples of the LoCuSS clusters. The box denotes our "High-L_X" sample, defined by $L_X/E(z)^{2.7} > 4.2 \times 10^{44}\,\mathrm{erg\,s^{-1}}$ as $0.15 < z < 0.3$, where $E(z)$ is the redshift evolution of the Hubble expansion rate. Also, for a comparison the solid curve denotes the luminosity with a constant flux of $f_X = 3 \times 10^{-12}\,\mathrm{erg\,s^{-1}\,cm^{-2}}$, assuming our fiducial cosmological model.

(cross symbols), defined by $L_X/E(z)^{2.7} \geq 4.2 \times 10^{44}\,\mathrm{erg\,s^{-1}}$. The average luminosity distribution of these samples is statistically indistinguishable from our representative sample of 29 clusters: the 3000 samples have $\langle L_X/E(z)^{2.7}\rangle = 6.22 \times 10^{44}\,\mathrm{erg\,s^{-1}}$ and $\sigma(L_X/E[z]^{2.7}) = 0.53 \times 10^{44}\,\mathrm{erg\,s^{-1}}$ for the average and the standard deviation, respectively, which contain the average of the Subaru sample, $\langle L_X/E(z)^{2.7}\rangle = 6.12 \times 10^{44}\,\mathrm{erg\,s^{-1}}$ within the $1\,\sigma$ range. Our sample is therefore statistically indistinguishable from a volume-limited sample. The observed clusters and the basic parameters of the observations are listed in table 1.

As discussed in detail in section 3 and appendix 1, we use two filter data, if available, in order to minimize, via color selection, a dilution of the weak lensing signal caused by contamination of the background galaxy catalog by faint cluster and foreground galaxies.

2.3. Image Processing and Photometry

The data were reduced using the same algorithm as that described by Okabe and Umetsu (2008). Briefly, the standard pipeline reduction software for Suprime-Cam, SDFRED (Yagi et al. 2002; Ouchi et al. 2004), was used for flat-fielding, instrumental distortion correction, differential refraction, PSF matching, sky subtraction, and stacking. The size of the seeing disk in the final reduced data is very important for successful weak lensing measurements. The width (in FWHM) of point sources in the reduced data is listed for each cluster in table 1. A small seeing disk of FWHM $\simeq 0.''7$ was achieved. An astrometric solution was obtained for each cluster observation by comparing the final mosaicked image

[2] All 30 clusters minus ZwCl 0740 — see below for the details.

Table 1. Cluster sample.*

Cluster	RA (J2000)	Dec (J2000)	Redshift z	L_X (10^{44} erg s^{-1})	i' (min)	V (min)	Seeing ($''$)
(1)	(2)	(3)	(4)	(5)	(6)	(7)	(8)
A 68	00 37 05.28	+09 09 10.8	0.2546	8.81	16.0‡	30.0‡	0.83
A 115	00 55 59.76	+26 22 40.8	0.1971	8.63	25.0‡	9.0#	0.71
ZwCl 0104.4+0048	01 06 48.48	+01 02 42.0	0.2545	5.80	35.0‡	—	0.65
A 209	01 31 53.00	−13 36 34.0	0.2060	7.27	22.0#	30.0#	0.63
RX J0142.0+2131	01 42 02.64	+21 31 19.2	0.2803	5.86	40.0‡	30.0‡	0.67
A 267	01 52 48.72	+01 01 08.4	0.2300	8.11	40.0‡	30.0‡	0.61
A 291	02 01 44.20	−02 12 03.0	0.1960	5.65	36.0‡	30.0‡	0.71
A 383	02 48 02.00	−03 32 15.0	0.1883	5.27	36.0‡	30.0‡	0.67
A 521	04 54 6.88	−10 13 24.6	0.2475	9.46	22.0#,‡‡	22.0#	0.61
A 586	07 32 22.32	+31 38 02.4	0.1710	6.58	35.0‖	20.0§	0.83
ZwCl 0740.4+1740†	07 43 23.16	+17 33 40.0	0.1114	—	25.0‖	20.0‖	0.83
ZwCl 0823.2+0425	08 25 57.84	+04 14 47.5	0.2248	4.41	35.0‖	16.0‖	0.71
ZwCl 0839.9+2937	08 42 56.07	+29 27 25.7	0.1940	3.79	35.0‖	—	0.77
A 611	08 00 55.92	+36 03 39.6	0.2880	8.05	30.0‖	16.0‖	0.79
A 689	08 37 25.44	+14 58 58.8	0.2793	17.99	40.0‖	20.0‖	0.69
A 697	08 42 57.84	+36 21 54.0	0.2820	9.64	40.0‖	16.0‖	0.73
A 750	09 09 11.76	+10 59 20.4	0.1630	5.50	28.0#	32.0#	0.71
A 963	10 17 01.20	+39 01 44.4	0.2060	6.16	I_c, 50.0#,††	—	0.75
A 1835	14 01 02.40	+02 52 55.2	0.2528	22.80	20.0§	20.0§	0.89
ZwCl 1454.8+2233	14 57 14.40	+22 20 38.4	0.2578	7.80	36.0§	15.0§	0.81
A 2009	15 00 20.40	+21 21 43.2	0.1530	5.40	R_c, 26.0#,**,‡‡	—	0.75
ZwCl 1459.4+4240	15 01 23.13	+42 20 39.6	0.2897	6.66	R_c, 27.0#	18.0#	0.57
A 2219	16 40 22.56	+46 42 21.6	0.2281	12.07	R_c, 24.0#	18.0#	0.99
RX J1720.1+2638	17 20 08.88	+26 38 06.0	0.1640	9.54	32.0§	20.0§	0.71
A 2261	17 22 27.60	+32 07 37.2	0.2240	10.76	R_c, 27.0#	18.0#	0.63
A 2345	21 27 11.00	−12 09 33.0	0.1760	4.95	30.0‡	—	0.77
RX J2129.6+0005	21 29 37.92	+00 05 38.4	0.2350	11.00	44.0‡	30.0‡	0.85
A 2390	21 53 36.72	+17 41 31.2	0.2329	12.69	R_c, 38.0#	12.0#	0.65
A 2485	22 48 31.13	−16 06 25.6	0.2472	5.90	40.0‡	30.0‡	0.67
A 2631	23 37 40.08	+00 16 33.6	0.2780	7.85	R_c, 24.0#	12.0#	0.65

* Column (1): cluster name; Columns (2), (3): right ascension (RA) and declination (Dec) (J2000.0); Column (4): redshift; Column (5): the ROSAT X-ray luminosity in the 0.1–2.4 keV band; Columns (6), (7): exposure times in the i' and V, respectively. Note that a case such as I_c, 50.0 means 50 min exposures for the I_c filter. Column (8): the seeing FWHMs for either of i', R_c, and I_c filters that are used for our weak lensing analysis.

† ZwCl 0740.4+1740 was observed by an incorrect pointing, and is nevertheless added to our sample because a cluster exists in the field. The redshift is taken from NED.

‡ Observed in the semester S05B.

§ Observed in the semester S06A.

‖ Observed in the semester S07A.

\# Data retrieved from SMOKA.

** Data of w67c1 chip is not usable.

†† Data taken without AG (acquisition and guide) probe for guide stars.

‡‡ Data taken without performing focus test before taking images.

with the 2MASS catalog (Skrutskie et al. 2006). The typical residuals on these fits were less than the CCD pixel size (0.″22) — i.e., sufficient for our lensing study. A photometric calibration was achieved by reference to standard star observations that were interspersed between the science observations, and SDSS photometry, where available (Adelman-McCarthy et al. 2008). The uncertainties on the photometric calibration were typically $\lesssim 0.1$ mag. Photometric catalogs were constructed from mosaic images using SExtractor (Bertin & Arnouts 1996).

2.4. *Weak Lensing Distortion Analysis*

Our weak lensing analysis was done using the IMCAT package, kindly provided by N. Kaiser,[3] which was developed based on the formalism described in Kaiser, Squires, and Broadhurst (1995, hereafter KSB). We also incorporated modifications by Erben et al. (2001) into the analysis pipeline (see Okabe & Umetsu 2008 for the details).

[3] ⟨http://www.ifa.hawaii/kaiser/IMCAT⟩.

Table 2. PSF anisotropy correction.[†]

Cluster	$\bar{e}_1^*$ 10^{-2}	$\bar{e}_2^*$ 10^{-2}	$\sigma(e^*)$ 10^{-2}	$\bar{e}_1^{*\rm res}$ 10^{-4}	$\bar{e}_2^{*\rm res}$ 10^{-4}	$\sigma(e^{*\rm res})$ 10^{-3}	N^*	$\bar{r}_{\rm h}^*$ ($''$)
(1)	(2)			(3)			(4)	(5)
A 68	+1.59	+1.10	2.11	−0.49 ± 2.69	−0.80 ± 1.81	6.49	402	0.44
A 115	+0.86	−1.98	3.52	+2.73 ± 2.46	+1.01 ± 1.51	6.80	554	0.37
ZwCl 0104	−4.28	+0.79	3.07	+3.48 ± 3.34	−1.38 ± 1.77	8.13	463	0.32
A 209	+0.85	−4.74	3.29	+0.33 ± 2.33	+6.05 ± 2.26	6.64	418	0.33
RX J0142	+1.80	−2.07	2.91	+0.21 ± 1.80	+2.34 ± 1.26	5.35	594	0.35
A 267	−1.98	−0.85	2.91	−0.25 ± 2.17	+0.90 ± 1.63	5.59	425	0.32
A 291	+0.61	+1.94	2.52	−1.45 ± 1.51	−0.28 ± 1.37	4.14	412	0.38
A 383	−0.66	+2.19	2.18	+0.27 ± 1.86	−1.21 ± 1.51	4.25	316	0.35
A 521	−0.29	+1.47	2.53	−1.25 ± 1.68	−1.37 ± 1.01	6.34	1046	0.33
A 586	−0.99	+0.53	2.22	−0.09 ± 0.76	+0.91 ± 0.56	3.28	1196	0.47
ZwCl 0740	−3.11	−1.50	1.90	+1.24 ± 1.14	+0.69 ± 0.61	4.35	1126	0.44
ZwCl 0823	+1.24	−0.36	2.68	+0.10 ± 1.01	+0.30 ± 0.68	4.79	1543	0.39
ZwCl 0839	−1.86	+3.32	3.01	+0.14 ± 1.42	−2.97 ± 1.38	4.63	544	0.41
A 611	−2.06	−2.56	2.81	−0.41 ± 1.01	+2.14 ± 1.08	3.62	596	0.42
A 689	−2.55	−1.77	2.51	+2.46 ± 1.71	+0.78 ± 1.02	4.66	549	0.36
A 697	−0.74	−0.13	4.28	+0.10 ± 0.86	+0.07 ± 0.66	1.95	325	0.38
A 750	+0.15	+0.81	2.04	+1.11 ± 1.67	−1.88 ± 1.07	5.63	806	0.38
A 963	−1.02	−0.17	2.50	−2.65 ± 2.03	+0.86 ± 1.56	4.42	298	0.39
A 1835	−1.52	+1.88	1.67	+0.26 ± 1.24	−0.24 ± 0.90	3.57	547	0.47
ZwCl 1454	−1.28	−0.30	1.99	−0.13 ± 1.40	+0.92 ± 0.87	3.83	538	0.43
A 2009	+2.10	−0.48	1.82	−0.56 ± 2.46	+0.05 ± 1.10	6.30	546	0.40
ZwCl 1459	−0.94	−1.73	2.25	+4.27 ± 2.97	+3.95 ± 1.73	7.83	518	0.31
A 2219	1.83	0.27	0.97	−0.94 ± 0.85	0.32 ± 0.53	2.58	657	0.51
RX J1720	+1.16	+0.12	2.60	−0.96 ± 1.15	−0.39 ± 0.61	4.11	998	0.39
A 2261	+0.85	−1.36	1.53	−0.20 ± 1.21	+1.32 ± 0.61	4.08	911	0.34
A 2345	+2.92	+0.89	3.23	+1.10 ± 1.79	+1.36 ± 1.22	6.86	994	0.39
RX J2129	+1.20	+4.92	2.50	−0.55 ± 0.91	−2.95 ± 0.84	4.72	1446	0.45
A 2390	−2.39	−1.41	2.17	+1.13 ± 1.34	+0.79 ± 0.70	6.44	1811	0.36
A 2485	−2.03	+2.21	2.36	+0.32 ± 2.11	−0.96 ± 1.34	5.46	476	0.35
A 2631	−2.35	+1.02	2.58	+0.63 ± 1.73	−0.18 ± 1.01	4.78	571	0.34

[†] Column (1): cluster name (we used the abbreviation for some clusters' names); Column (2): mean and standard deviation for two components of stellar ellipticities before PSF correction; Column (3): mean and standard deviation after the PSF anisotropy correction; Column (4): number of stellar objects used in the analysis; Column (5): median stellar half-light radius in units of arcsecond.

In order to obtain accurate lensing measurements, it is of critical importance to correct for atmospheric distortion effects due to seeing smearing and PSF anisotropy. After constructing object catalogs of galaxies and stars that are detected with significant signal-to-noise ratio ($>6\sigma$ for our study), yet unsaturated, we first measure the image ellipticity of individual galaxies by computing the weighted quadrupole moments of the surface brightness with respect to the galaxy center. Then, according to the KSB method, the PSF anisotropy is corrected as

$$e'_\alpha = e_\alpha - P^{\alpha\beta}_{\rm sm} q^*_\beta, \tag{1}$$

where $P^{\alpha\beta}_{\rm sm}$ is the smear polarisability matrix being close to the diagonal, and $q^*_\alpha = (P^*_{\rm sm})^{-1}_{\alpha\beta}\, e^\beta_*$ is the stellar anisotropy kernel (hereafter quantities with an asterisk denote the quantities for stellar objects). We select bright unsaturated stars identified in the half-light radius, $r_{\rm h}$, vs. (either of i', $R_{\rm c}$, and $I_{\rm c}$) magnitude diagram to estimate q^*_α for individual stellar objects. To obtain an estimate on q^*_α at each galaxy position in equation (1), we need to construct a map of q^*_α that smoothly varies with the angular position. We therefore divide the frame into several chunks, the sizes of which are determined based on the typical coherent scale of the measured PSF anisotropy pattern. We then fit the discrete distribution of q^* in each chunk independently to second-order bi-polynomials of vector $\boldsymbol{\theta}$ to obtain $q^\alpha_*(\boldsymbol{\theta})$ at each galaxy position, in conjunction with iterative σ-clipping rejection on each component of the residual, $e^{*({\rm res})}_\alpha = e^*_\alpha - P^{\alpha\beta}_{*{\rm sm}} q^*_\beta(\boldsymbol{\theta})$.

Table 2 summarizes the results of the PSF anisotropy correction in each cluster field. While the mean and rms of the original stellar ellipticities are typically both a few per cent, the correction described above reduces the residual ellipticities to $|\bar{e}^{*\rm res}_\alpha| \lesssim 10^{-4}$ and the rms of the residuals, $\sigma(e^{*\rm res})$ to less than 10^{-2} for all clusters, even down to a few times

10^{-3} for a few clusters. Measurements of cluster distortion signals of $> 10^{-2}$ should therefore be robust, based on this PSF anisotropy correction.

Next we correct for the isotropic smearing of galaxy images caused by seeing and the Gaussian window function used for the shape measurements. An estimate of the pre-seeing reduced distortion signal, g_α, for each galaxy can be obtained from

$$g_\alpha = (P_{\rm g}^{-1})_{\alpha\beta} e'_\beta, \tag{2}$$

where $P^{\rm g}_{\alpha\beta}$ is the pre-seeing shear polarizability tensor. To reduce the noise, we employ the following procedures. First the tensor $P^{\rm g}_{\alpha\beta}$ for each galaxy is estimated based on a scalar correction approximation (Hudson et al. 1998; Hoekstra et al. 1998; Erben et al. 2001) as

$$(P_{\rm g})_{\alpha\beta} = \frac{1}{2}{\rm tr}[P_{\rm g}]\delta_{\alpha\beta} \equiv P^{\rm s}_{\rm g}\delta_{\alpha\beta}. \tag{3}$$

The tensor $P^{\rm s}_{\rm g}$ for individual galaxies is still noisy, especially for small and faint galaxies, and therefore we employ a practically useful procedure developed by Van Waerbeke et al. (2000; see also Erben et al. 2001; Hamana et al. 2003). We first identify 30 neighboring galaxies around each galaxy in the magnitude–$r_{\rm g}$ plane, where $r_{\rm g}$ is the Gaussian smoothing radius used in the KSB method, and then compute, over the defined neighboring sample, the median value, $\langle P^{\rm s}_{\rm g}\rangle$, as an estimate on $P_{\rm g}$ used in equation (3). We thus use the following estimator for the reduced distortion signal of each galaxy:

$$g_\alpha = \frac{e'_\alpha}{\langle P^{\rm s}_{\rm g}\rangle}. \tag{4}$$

Using this equation, we also compute the variance $\sigma_g^2 (\equiv \sigma_{g_1}^2 + \sigma_{g_2}^2)$ for each galaxy over the neighboring sample. We below use the dispersion σ_g^2 to estimate a statistical error in measuring the lensing distortion signals, as described around equation (8). Typically, $\sigma_g \sim 0.4$ for our galaxy samples.

2.5. *Tangential Distortion Profile*

As indicated in equation (4), the reduced distortion is given by two components reflecting the spin-2 field nature (e.g., see Bartelmann & Schneider 2001): $\boldsymbol{g} = (g_1, g_2)$. For cluster lensing it is useful to define, for each galaxy, the tangential distortion component, g_+, and the 45° rotated component, $g_\times$, with respect to the cluster center:

$$\begin{aligned} g_{+(i)} &= -(g_{1(i)}\cos 2\varphi + g_{2(i)}\sin 2\varphi), \\ g_{\times(i)} &= -g_{1(i)}\sin 2\varphi + g_{2(i)}\cos 2\varphi, \end{aligned} \tag{5}$$

where subscript (i) denotes the i-th galaxy, and φ is the position angle between the first coordinate axis on the sky and the vector connecting the cluster center and the galaxy position. The minus sign for the definition of g_+ is introduced so that g_+ becomes positive or negative when a background galaxy shape is tangentially or radially deformed with respect to the cluster center, respectively. The tangential distortion contains full information about the lensing signals if the lensing mass distribution is axisymmetric on the sky. Clusters can be considered as gravitationally bound spherical objects to zeroth order; therefore, studying the tangential distortion profile is a sensible first step. The position of the brightest cluster galaxy (BCG) is adopted as the cluster center for this analysis (see also subsection 1.2).

The weak lensing signal of a cluster is typically 0.01–0.1 in ellipticities, and cannot be distinguished from the intrinsic ellipticity of individual galaxies. The coherent weak lensing distortion pattern is therefore only measurable at high significance when averaged over sufficient background galaxies, thus beating down the "shape noise" attributable to the (assumed) random intrinsic ellipticity distribution of background galaxies. Note that the assumption of random intrinsic galaxy ellipticities and orientations is safe because the majority of galaxies considered are separated by cosmological distances, and therefore are not physically associated with each other. The tangential distortion profile is estimated as

$$\langle g_+\rangle(\theta_n) = \frac{\sum_i w_{(i)} g_{+(i)}}{\sum_i w_{(i)}}, \tag{6}$$

with the weight function, $w_{(i)}$, being given by

$$w_{(i)} \equiv \frac{1}{\alpha^2 + \sigma^2_{g(i)}}. \tag{7}$$

In equation (6) the summation runs over all the galaxies residing in the n-th radial bin, θ_n, with a given bin width. The weighting $w_{(i)}$ is used to down-weight galaxies whose shapes are less reliably measured, based on the uncertainty in the shape measurement, $\sigma_{g(i)}$, estimated for the i-th galaxy (see subsection 2.4), following Van Waerbeke et al. (2000). We use $\alpha = 0.4$ throughout this paper.

The other distortion component, $g_\times$ [see equation (5)], should vanish after the azimuthal average in the weak lensing regime. Therefore, the measured $\langle g_\times\rangle(\theta_n)$ in each radial bin serves as a monitor of systematics errors, most likely arising from an imperfect PSF correction.

The statistical uncertainty on the tangential distortion profile in each radial bin can be estimated as

$$\sigma^2_{g_+}(\theta_n) = \frac{1}{2}\frac{\sum_i w^2_{(i)}\sigma^2_{g(i)}}{\left(\sum_i w_{(i)}\right)^2}, \tag{8}$$

where the prefactor $1/2$ accounts for the fact that $\sigma_{g(i)}$ is the rms for the sum of two distortion components [see below equation (4)]. The statistical error in $\langle g_\times\rangle(\theta_n)$ is the same as that given in equation (8). Here, we have assumed that the dominant source of the measurement errors is the intrinsic ellipticities, that are uncorrelated between different radial bins. We thus, for simplicity, ignore the error contribution arising from cosmic shearing effects on galaxy images caused by large-scale structures along the line-of-sight through a cluster. As discussed in Hoekstra (2003; also see Dodelson 2004), the cosmic shear contribution may reduce an accuracy of an cluster mass estimation from the distortion profile. However, we checked that the cosmic shear contamination is insignificant, because the shot noise turns out to be more significant than assumed in Hoekstra (2003), due to a smaller number of galaxies used in the lensing analysis after our background galaxy selection (see Oguri et al. 2010 for the detail).

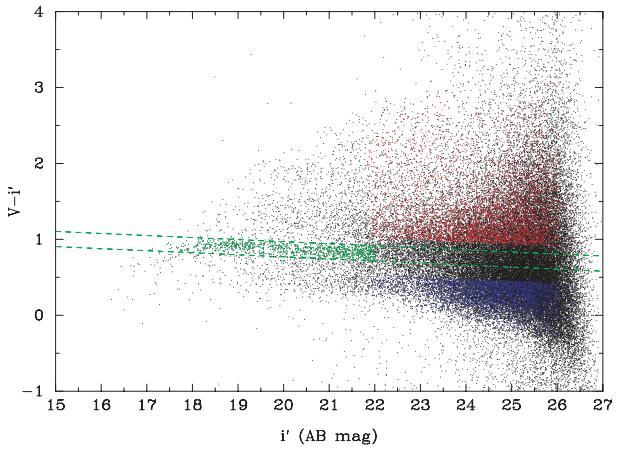

Fig. 2. Color–magnitude diagram and our galaxy samples for A 68 as one representative example (see text for details). Green points are the member galaxy sample for E/S0 galaxies of this cluster, where the two dashed curves denote the width of the red sequence. The red and blue points are the background galaxy samples redder and bluer than the red-sequence, respectively, used for the lensing distortion analysis. Note that these shear catalogs are chosen by imposing another condition that galaxies are well resolved to make reliable shape measurements, so do not include all of the red/blue galaxies in the diagram.

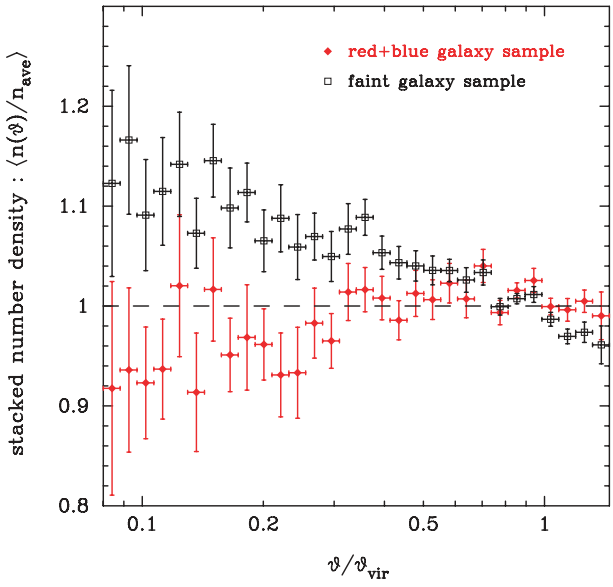

Fig. 3. Radial profiles of galaxy number density stacked over 21 clusters with two passband data, for the faint background galaxy samples (square symbols) and the red + blue galaxy samples (circle), respectively. The profiles are computed by stacking the number densities in each radial bins normalized by the virial radius of each cluster for the galaxy samples of 21 clusters. The profile for the faint galaxy samples shows increasing number densities with decreasing radius, indicating contamination of member galaxies. On the other hand, the red + blue galaxy sample does not show any excess at the inner radii.

3. Galaxy Sample Selection and Source Redshift Estimation

3.1. Galaxy Sample Selection

Including unlensed galaxies, mainly cluster members in the case of our low-z clusters, into the background galaxy catalog dilutes the measured lensing strengths. Therefore, it is of vital importance to minimize contamination of the background galaxy catalogs in order to obtain robust lensing measurements (Broadhurst et al. 2005; Limousin et al. 2007). For the clusters for which data in two filters are available (see table 1), we therefore define the following four galaxy samples:

- Member galaxy sample: brightest cluster galaxy (BCG) plus galaxies that are contained in the cluster red sequence and brighter than 22 mag (AB) in the red-band magnitude (either of i', R_c, and I_c).
- Faint galaxy sample: galaxies that are in the magnitude range listed in table 3 (typically fainter than 22 mag) and are well resolved so as to be usable for weak lensing analysis.
- Red galaxy sample: galaxies contained in the faint galaxy sample, but redder than the cluster red sequence at least by a finite color offset that is chosen to reduce the monitored dilution effect on the lensing distortion signal.
- Blue galaxy sample: galaxies contained in the faint galaxy sample, but bluer than the red sequence at least by a finite color offset.

As one example, figure 2 shows these galaxy samples in the color–magnitude diagram of A 68. For the clusters for which single filter data are available, we use the faint galaxy sample for our lensing analysis. In appendix 1 we describe in detail how the galaxy samples are defined based on the color–magnitude information of galaxies, constructed from two filter data. We briefly summarize the method below.

Broadhurst et al. (2005) showed that selecting galaxies redder than the cluster red sequence yields galaxy samples dominated by background galaxies because the red galaxy colors are caused by larger k-corrections than for lower redshift objects. These photometric results have also been confirmed spectroscopically by Rines and Geller (2008). However, solely using red galaxies for weak lensing analysis generally leads to low signal-to-noise ratios because of the relatively small number density of red galaxies. We therefore used combined red plus blue galaxy samples as our fiducial sample of background galaxies in order to obtain a higher statistical precision for our lensing measurements.

In brief, the method for determining the appropriate color cuts with which to define the red and blue galaxy samples — i.e., how much redder or bluer than the cluster red sequence needs to qualify as a red or blue galaxy respectively — consists of plotting the mean distortion profile strength $\langle\langle g_+\rangle\rangle$ [see equation (A2) for the definition] as a function of the color offset from the cluster red sequence. In regions of high contamination (i.e., small color offsets) the value of $\langle\langle g_+\rangle\rangle$ is depressed due to the stronger dilution of distortion signals. The optimal color offsets are thus chosen to minimize this effect (e.g., see figure 12) — the typical color cuts are $|\Delta\mathrm{color}| \simeq [0.1, 0.4]$ for the redder and bluer galaxies than the cluster red-sequence.

A justification on the effectiveness of the red and blue color selection method is given by figure 3 showing the stacked number density profiles as a function of the cluster-centric radius for the faint and red + blue galaxy samples, respectively.

Table 3. Background galaxy samples and the lensing distortion signals.*

Cluster	$r_{\rm h}$ (pix. scale)	magnitude (AB mag)	$n_{\rm g}^{\rm all}$ (arcmin^{-2})	$\langle\langle g_+\rangle\rangle$ (10^{-2})	(S/N)	$n_{\rm g}^{\rm red\,+\,blue}$ (arcmin^{-2})	$\langle\langle g_+\rangle\rangle$ (10^{-2})	(S/N)
(1)	(2)	(3)	(4)	(5)	(6)	(7)	(8)	(9)
A 68	[2.25–10.00]	[22.0–26.0]	19.85	2.60 ± 0.53	6.20	9.61	3.65 ± 0.94	5.83
A 115	[1.96– 4.00]	[22.0–26.0]	14.23	1.80 ± 0.60	5.99	5.94	3.79 ± 1.05	5.39
ZwCl 0104	[1.70–10.00]	[22.0–26.0]	42.88	2.44 ± 0.42	7.60	—	—	—
A 209	[1.79–10.00]	[22.0–25.8]	37.13	3.78 ± 0.66	14.30	20.90	5.83 ± 1.10	12.85
RX J0142	[1.85–10.00]	[22.0–26.0]	36.92	3.56 ± 0.68	9.78	20.71	6.60 ± 1.18	9.47
A 267	[1.66–10.00]	[22.0–26.0]	42.82	4.61 ± 0.64	11.90	24.10	5.48 ± 0.85	9.30
A 291	[2.04–10.00]	[21.5–26.3]	36.84	2.23 ± 0.44	9.50	18.06	3.17 ± 0.68	8.26
A 383	[1.81–10.00]	[22.0–26.2]	48.15	4.01 ± 0.40	12.57	33.81	4.95 ± 0.52	12.00
A 521	[1.74–10.00]	[22.0–26.2]	43.65	3.02 ± 0.54	11.74	27.26	3.98 ± 0.78	9.81
A 586	[2.50–10.00]	[22.0–26.0]	22.02	6.73 ± 0.86	11.31	7.48	11.20 ± 1.99	9.08
ZwCl 0740	[2.25–10.00]	[21.5–25.5]	21.55	1.89 ± 0.48	7.19	16.73	2.23 ± 0.60	6.56
ZwCl 0823	[2.11–10.00]	[22.0–25.9]	26.61	3.64 ± 0.51	11.24	16.92	4.08 ± 0.60	10.38
ZwCl 0839	[2.23–10.00]	[22.1–26.0]	26.82	3.67 ± 0.61	7.67	—	—	—
A 611	[2.15–10.00]	[22.0–26.0]	31.23	3.04 ± 0.47	9.63	21.00	4.08 ± 0.59	9.81
A 689	[1.86–10.00]	[22.0–26.0]	39.80	0.52 ± 0.42	6.38	22.08	1.49 ± 0.58	5.29
A 697	[2.04–10.00]	[22.0–26.2]	39.10	3.01 ± 0.49	12.53	20.58	5.21 ± 0.76	12.06
A 750	[2.06–10.00]	[22.0–26.0]	31.67	2.80 ± 0.38	13.70	13.59	4.51 ± 0.67	10.30
A 963	[2.08–10.00]	[21.5–26.1]	43.57	3.15 ± 0.44	11.45	—	—	—
A 1835	[2.44–10.00]	[20.0–24.5]	19.76	4.16 ± 0.52	11.79	14.93	4.60 ± 0.66	11.11
ZwCl 1454	[2.21–10.00]	[21.8–24.8]	20.85	3.90 ± 0.88	7.39	9.78	4.05 ± 1.12	5.84
A 2009	[2.14–10.00]	[22.4–26.1]	25.47	3.85 ± 0.56	9.42	—	—	—
ZwCl 1459	[1.64–10.00]	[22.0–26.3]	56.26	3.13 ± 0.56	9.80	11.18	5.93 ± 1.66	7.45
A 2219	[2.65–10.00]	[22.0–26.0]	25.77	4.13 ± 0.52	12.13	10.33	9.26 ± 1.10	11.27
RX J1720	[2.03–10.00]	[20.0–24.2]	20.12	2.92 ± 0.52	6.70	10.72	4.77 ± 0.77	7.75
A 2261	[1.76–10.00]	[22.0–26.0]	44.77	4.13 ± 0.37	16.49	16.76	6.85 ± 0.71	12.90
A 2345	[2.01– 4.00]	[22.0–25.8]	15.68	2.26 ± 0.63	6.78	—	—	—
RX J2129	[2.34–10.00]	[22.0–25.5]	26.51	2.80 ± 0.50	8.42	15.49	3.97 ± 0.71	7.89
A 2390	[1.89–10.00]	[22.0–26.2]	33.58	5.91 ± 0.67	14.73	10.70	9.55 ± 1.31	10.66
A 2485	[1.81–10.00]	[22.0–25.9]	38.35	2.79 ± 0.49	9.52	15.06	3.50 ± 0.82	6.78
A 2631	[1.79–10.00]	[22.0–26.3]	47.11	3.25 ± 0.43	10.55	30.89	5.47 ± 0.61	11.30

* Column (1): cluster name; Column (2): the range of half light radius used in selecting the background galaxy sample; Column (3): the magnitude range of the background galaxy sample; Column (4): the angular number density of background galaxies for the faint galaxy sample (see text for the details); Column (5): the mean strength of the tangential distortion profile averaged over radii from $\simeq 1'$ up to the outermost radius, measured for the faint galaxy sample [see equation (A2) for the definition]; Column (6): the total signal-to-noise ratio for the tangential distortion signal [see equation (9)]; Column (7): the number density for the red + blue background galaxy sample (the row marked "—" denotes the cluster where no color information on galaxies is available); Columns (8) and (9): similar to Columns (5) and (6), but for the red + blue galaxy sample.

These stacked profiles are constructed from the 21 clusters for which data are available in two filters, excluding ZwCl 0740 (the lowest redshift cluster). The number density profile of the faint galaxy sample shows increasing densities at smaller cluster-centric radii, as expected for a catalog that is contaminated by faint cluster members. On the other hand, the number density profile of red + blue galaxies does not show any evidence of excess in the number densities at small radii, and is consistent with a constant density within the Poisson errors. One may notice that a slight depression exists in the number density at small radii, for the red + blue galaxy sample. This is probably due to an overestimation in the solid angle in computing the number density. Since the red + blue galaxy sample is defined from the faint galaxy sample by excluding galaxies around the red-sequence, we have to take into account the masking effect of the excluded galaxies on the solid angle on the sky, and this masking contamination is more significant at smaller radii due to an increased contribution of member galaxies. However, we ignored this effect, and this likely cause us to underestimate the number densities at small radii for the red + blue galaxy sample. Furthermore, the number densities at such small radii may be affected by a magnification effect on the background galaxies, which causes the galaxies to be included or excluded in the sample within a given magnitude range.

Table 3 summarizes the background galaxy samples obtained based on the methods outlined above, the number density of galaxies in the faint and red + blue galaxy samples, the mean strength of the tangential distortion profiles and the total signal-to-noise ratio measured for each galaxy sample. Here the signal-to-noise ratios are defined from equations (6) and (8) as

$$\left(\frac{S}{N}\right)^2 \equiv \sum_{n=1}^{N_{\rm bin}} \frac{[\langle g_+\rangle(\theta_n)]^2}{\sigma^2_{g_+}(\theta_n)}. \quad (9)$$

We emphasize that the Subaru data allow us to achieve a significant detection of the tangential distortion at $(S/N) \gtrsim 5$ for all cluster fields. A comparison of the 5th and 8th columns in table 3 also quantitatively confirms the impact of dilution on weak lensing signal — the mean distortion signal is larger for the red + blue galaxy sample than for the faint galaxy sample in every cluster for which two filter data are available. However, the number density of galaxies in the red + blue samples is a factor of $\sim$1.5–3 lower than in the faint galaxy samples (see 4th and 7th columns of table 3). Nevertheless, as a result of the balance between these competing effects, the total signal-to-noise ratios are only degraded by $\lesssim$20% in most cases, and by $\sim$30% for a few clusters (see 6th and 9th columns).

3.2. Source Redshift Estimation

The overall normalization of the lensing distortion signals depends on the redshift distribution of background galaxies. An uncertainty in the source redshift causes biases in parameter estimations.

The lensing amplitude for a given cluster of known redshift scales with the mean distance ratio averaged over the population of source galaxies,

$$\left\langle \frac{D_{\rm ls}}{D_{\rm s}} \right\rangle = \int dz \, \frac{dp_{\rm wl}}{dz} \frac{D_{\rm ls}}{D_{\rm s}}, \quad (10)$$

where $D_{\rm ls}$ and $D_{\rm s}$ are the angular diameter distances from the lens to the source and from the observer to the source. The probability distribution function, $dp_{\rm wl}/dz$, is the redshift distribution of the source galaxies used in the lensing analysis.

Since redshifts of our imaging galaxies are not available, we instead employ a statistical approach, as follows. In order to estimate $dp_{\rm wl}/dz$ we used the COSMOS photometric redshift catalog given in Ilbert et al. (2009). The photometric redshifts were estimated by combining 30 broad, intermediate, and narrow bands covering a wide range of wavelengths from UV, optical, to mid infrared, and also calibrated using a spectroscopic subsample. Hence, the catalog currently provides the most reliable redshift distribution for a magnitude-limited galaxy sample selected with $i < 25$ in the Subaru i-band data. In addition, the catalog is constructed from a sufficiently large survey area of about 2 square degrees; therefore, it can be considered to be a fairly representative sample of distant galaxies.

To estimate redshifts of our galaxy samples, we first construct a subsample of galaxies from the COSMOS catalog by imposing the same color cut as that used in our weak lensing analysis for each cluster field (see table 3 for the cuts). We then computed the average distance ratio (10) using the redshift distribution of the COSMOS subsample based on the available photo-z information. Although our source galaxies contained galaxies fainter than $i = 25$, as listed in table 3, we ignored the contribution because the fraction of such faint galaxies in our source galaxies is not large, and the redshift distribution does not so much change for the range of limiting magnitudes, $25 < i < 26$. Table 4 gives the estimated distance ratio for each cluster field. Note that the distance ratio for a faint galaxy sample varies with the clusters because of the different ranges of magnitudes used to define the faint galaxy sample as well as the differences of the cluster redshifts. A typical error inferred from the statistical errors of photometric redshifts is found to be, at most, a few per cent in $\langle D_{\rm ls}/D_{\rm s}\rangle$. We will come back to a possible residual uncertainty in the source redshifts in sub-subsection 5.7.2; it turns out that the uncertainty, even if it exists, does not cause any significant changes to the cluster parameters because our clusters are all at low redshifts, [0.15, 0.3].

Table 4. Distance ratio averaged over the redshift distribution of the background galaxy sample.*

Cluster	$\langle D_{\rm ls}/D_{\rm s}\rangle_{\rm faint}$	$\langle D_{\rm ls}/D_{\rm s}\rangle_{\rm red+blue}$
A 68	0.655	0.660
A 115	0.701	0.715
ZwCl 0104	0.657	—
A 209	0.709	0.714
RX J0142	0.628	0.635
A 267	0.683	0.687
A 291	0.723	0.744
A 383	0.732	0.733
A 521	0.667	0.668
A 586	0.728	0.738
ZwCl 0740	0.820	0.827
ZwCl 0839	0.709	—
A 611	0.615	0.626
A 697	0.623	0.637
A 963	0.686	—
A 1835	0.584	0.603
ZwCl 1454	0.622	0.633
A 2009	0.779	—
ZwCl 1459	0.637	0.706
RX J1720	0.697	0.727
A 2219	0.684	0.762
A 2261	0.697	0.733
RX J2129	0.667	0.672
A 2390	0.691	0.736
A 2485	0.670	0.688
A 2631	0.639	0.655

* Column (1): cluster name; Column (2): distance ratio averaged over the redshift distribution of faint galaxy sample, calibrated based on the COSMOS photometric redshift catalog; Column (3): distance ratio averaged over the redshift distribution of red + blue galaxy sample.

4. Modeling of Lensing Distortion Signals

In this section we describe the modeling methods that will be applied to the data to constrain the cluster mass and density profile shape presented in section 5.

4.1. Model-Dependent Estimate of the 3D Cluster Mass

The definition of mass most often used in the literature is the three-dimensional mass enclosed within a spherical region of a given radius, r_Δ, inside of which the mean interior density is Δ times the critical mass density, $\rho_{\rm cr}(z)$, at cluster redshift,

$$M_\Delta = \frac{4\pi}{3} r_\Delta^3 \rho_{\rm cr}(z)\Delta. \tag{11}$$

Conventionally, either a constant over-density, such as $\Delta \simeq 200$ or the virial over-density, $\Delta = \Delta_{\rm vir}(z)$ (e.g., Nakamura & Suto 1997 for the definition of $\Delta_{\rm vir}$; see also Tomita 1969; Gunn & Gott 1972) are used. Note that $\Delta_{\rm vir} \simeq 112$ for halos at a redshift of $z = 0.2$ for our fiducial cosmological model. This spherical over-density mass is very useful from a theoretical viewpoint because the dark matter halo mass function derived from numerical simulations is well fitted by a simple analytical formula, such as the Press–Schechter function (Press & Schechter 1974; see also White 2002) if halo masses are computed using the spherical top-hat average of the mass distribution in each halo region in the simulations.

However, weak-lensing observables do not provide direct estimates of the three-dimensional masses of clusters because the lensing signal probes the two-dimensional projected mass distribution. We therefore estimate M_Δ by fitting a three-dimensional model to the data. In short, this consists of projecting the three-dimensional model to predict the observables based on a given set of model parameters, and then varying those model parameters to find the best-fit model and associated parameter uncertainties; M_Δ is then estimated by marginalizing over the other parameters. The tangential distortion profile (6) is one-dimensional, and is expressed as a function of the cluster-centric radius. If we simply assume a spherically symmetric mass distribution that corresponds to a circularly symmetric mass distribution on the sky after projection, the model distortion profile can be expressed, in the absence of noise, as

$$g_+(\theta) = \frac{\gamma(\theta)}{1-\kappa(\theta)}, \tag{12}$$

where $\kappa(\theta)$ and $\gamma(\theta)$ are the convergence and the shear profiles of the cluster (note that the shear has the tangential component alone for a circularly symmetric lens). It should also be noted that, exactly speaking, the equation given above is valid for a single source redshift, and needs to be modified when source galaxies have a redshift distribution (e.g., see subsubsection 4.3.2 in Bartelmann & Schneider 2001), but this effect is very small for low-redshift clusters at $z \simeq 0.2$, given the deep Subaru data.

We now briefly discuss the choice of the parametric form for the cluster mass models. The NFW model is a theoretically well-motivated mass model based on dark matter only numerical simulations. NFW found that the mass density profile of "equilibrium" CDM halos is well fitted by the following analytic function over a wide range of halo masses:

$$\rho_{\rm NFW}(r) = \frac{\rho_{\rm s}}{(r/r_{\rm s})(1+r/r_{\rm s})^2}, \tag{13}$$

where $\rho_{\rm s}$ is the central density parameter and $r_{\rm s}$ is the scale radius to divide the two distinct regimes of asymptotic mass density slopes, $\rho \propto r^{-1}$ and r^{-3}. The NFW profile is thus specified by two parameters. The enclosed mass within a sphere of radius r_Δ can be obtained by integrating the NFW profile up to r_Δ,

$$M_{\rm NFW,\Delta} = \frac{4\pi\rho_{\rm s} r_{\rm s}^3}{c_\Delta^3}\left[\ln(1+c_\Delta) - \frac{c_\Delta}{1+c_\Delta}\right], \tag{14}$$

where we have introduced the concentration parameter, the ratio of r_Δ relative to the scale radius, $c_\Delta \equiv r_\Delta/r_{\rm s}$. By equating equations (11) and (14), the NFW profile can be specified in terms of the two parameters M_Δ and c_Δ, instead of $\rho_{\rm s}$ and $r_{\rm s}$, once the cosmological parameters and the spherical top-hat over-density, Δ, are specified. We use this parametrization of the NFW profile throughout the rest of this paper.

It is then straightforward to compute the lensing profiles, $\kappa(\theta; M_\Delta, c_\Delta)$ and $\gamma(\theta; M_\Delta, c_\Delta)$, given the NFW profile (Bartelmann 1996; Wright & Brainerd 2000; Takada & Jain 2003). Inserting these profiles into equation (12) gives the NFW prediction for the tangential distortion profile to be compared with the measurement. In doing this, note that the lensing fields are dimension-less and given in units of the critical projected mass density, defined as

$$\Sigma_{\rm cr} \equiv \frac{c^2}{4\pi G} D_{\rm l}^{-1}\left\langle \frac{D_{\rm ls}}{D_{\rm s}}\right\rangle^{-1}, \tag{15}$$

where $D_{\rm l}$ is the angular diameter distance to a given cluster, and the average distance ratio, $\langle D_{\rm ls}/D_{\rm s}\rangle$, is estimated for source galaxy samples in each cluster field, as described in subsection 3.2.

An alternative simpler model often used in the literature is a singular isothermal sphere (SIS) model. This model is specified by one parameter, the one-dimensional velocity dispersion, σ_v^2; the density profile is given by

$$\rho_{\rm SIS}(r) = \frac{\sigma_v^2}{2\pi G}\frac{1}{r^2}. \tag{16}$$

Integrating this profile over a spherical region of radius r_Δ gives the enclosed mass,

$$M_{\rm SIS,\Delta} = \frac{2\sigma_v^2}{G} r_\Delta. \tag{17}$$

Again by equations (11) and (17), the SIS model is fully specified by either σ_v^2 or the over-density mass, M_Δ. The lensing fields, obtained by integrating the profile above along the line-of-sight, are found to be

$$\kappa(\theta) = \gamma(\theta) = \frac{\theta_{\rm E}}{2\theta}, \tag{18}$$

where $\theta_{\rm E}$ is the Einstein radius, defined as $\theta_{\rm E} \equiv 4\pi(\sigma_v/c)^2 D_{\rm ls}/D_{\rm s}$ (e.g., see Bartelmann & Schneider 2001 for further details).

We also consider a cored isothermal sphere (CIS) model that is obtained by introducing a softening "core" into an SIS model in an empirical manner. We use the CIS model given as

$$\kappa_{\rm CIS}(\theta) = \frac{\theta_{\rm E}}{2(\theta+\theta_{\rm c})}, \tag{19}$$

where $\theta_{\rm E}$ is not exactly the same as that for the SIS model given by equation (18), so should be considered as a model parameter, and $\theta_{\rm c}$ is the core radius parameter. Note that, for the limit $\theta_{\rm c} \to 0$, the CIS model becomes equivalent to the SIS model. The CIS model above is given by two parameters, similarly to the NFW model.

By comparing the goodness-of-fit of each model to the measured distortion profile for each cluster, we will discuss which of these mass models are preferred for real clusters.

4.2. Model-Independent Estimate of 2D Cluster Mass

It is also possible and very useful to derive a model-independent estimate of the cluster mass from weak lensing data. In the weak lensing limit, the azimuthally averaged tangential distortion in each circular annulus of radius θ, $\langle g_+\rangle(\theta)$ [see equation (6)], is related to the projected mass density (e.g., Bartelmann & Schneider 2000) as

$$\langle g_+\rangle(\theta) \simeq \langle\gamma_+\rangle(\theta) = \bar{\kappa}\,(<\theta) - \langle\kappa\rangle(\theta), \quad (20)$$

where $\langle\cdots\rangle(\theta)$ denotes the azimuthally averaged shear in the circular annulus, and $\bar{\kappa}$ is the mean convergence within a circular aperture of radius θ, defined as $\bar{\kappa}\,(<\theta) \equiv 1/(\pi\theta^2)\int_{|\boldsymbol{\theta}'|\le\theta} d^2\boldsymbol{\theta}'\kappa(\boldsymbol{\theta}')$. Note that relation (20) holds for an arbitrary mass distribution.

As implied by equation (20), if the tangential distortion profile, $\langle g_+\rangle$, can be measured out to sufficiently large radii from the cluster center, where the local convergence likely drops down to $\kappa \approx 0$, the measured tangential distortion at a large radius gives a direct estimate on the two-dimensional mass enclosed within the circular aperture: $\langle\gamma_+\rangle(\theta) \simeq \bar{\kappa}\,(<\theta) = M_{\rm 2D}(<\theta)/(\pi\theta^2)$. The large Suprime-Cam FoV is ideally suited to such measurements because the single pointing observations used in this study span cluster-centric radii of $\sim$1–2 $r_{\rm vir}$.

In this paper we employ the so-called $\zeta_{\rm c}$-statistics [slightly modified version made in Clowe et al. (2000) from the original method developed in Fahlman et al. (1994)]:

$$\begin{aligned}\zeta_{\rm c}(\theta_{\rm m},\theta_{\rm o1},\theta_{\rm o2}) &\equiv 2\int_{\theta_{\rm m}}^{\theta_{\rm o1}} d\ln\theta\ \langle\gamma_+\rangle(\theta) \\ &\quad + \frac{2}{1-\theta_{\rm o1}^2/\theta_{\rm o2}^2}\int_{\theta_{\rm o1}}^{\theta_{\rm o2}} d\ln\theta\ \langle\gamma_+\rangle(\theta) \\ &= \bar{\kappa}(<\theta_{\rm m}) - \bar{\kappa}(\theta_{\rm o1}\le\theta\le\theta_{\rm o2}), \end{aligned} \quad (21)$$

where the radii $\theta_{\rm m}$, $\theta_{\rm o1}$, and $\theta_{\rm o2}$ satisfy $\theta_{\rm m} < \theta_{\rm o1} < \theta_{\rm o2}$. If the radius $\theta_{\rm m}$ is also taken to be sufficiently large so that the weak lensing limit, $g_+ \approx \gamma_+$, holds, the quantity $\zeta_{\rm c}$ can be directly estimated from the measured tangential distortion profile, although the discrete summation for the radial binned profile, instead of the radial integration, needs to be employed. The radius $\theta_{\rm m}$ is the *target* radius that encloses the projected mass we aim to measure (see below). On the other hand, the two outermost radii, $\theta_{\rm o1}$ and $\theta_{\rm o2}$, are taken to be sufficiently far from the cluster center and are also, as suggested in Clowe et al. (2004), chosen so that any prominent substructures in the annulus of $\theta_{\rm o1} \le \theta \le \theta_{\rm o2}$, regardless of being associated with the cluster or not, are absent in the reconstructed mass map. Once these outer radii are set, we can safely consider $\bar{\kappa}\,(\theta_{\rm o1} \le \theta \le \theta_{\rm o2}) \sim 0$ to be valid in the second equality on the rhs of equation (21), and therefore the enclosed mass can be estimated as

$$M_{\rm 2D}(<\theta_{\rm m}) \simeq \pi\theta_{\rm m}^2\Sigma_{\rm cr}\zeta_{\rm c}(\theta_{\rm m},\theta_{\rm o1},\theta_{\rm o2}). \quad (22)$$

More precisely, the estimated mass above, $M_{\rm 2D}(<\theta_{\rm m})$, gives a lower limit on the true mass because there may be a non-vanishing mass contribution from the annulus region of $\theta_{\rm o1} \le \theta \le \theta_{\rm o2}$ as well as a constant mass-sheet contribution that does not change the measured distortion signals at all.

The uncertainty in $\zeta_{\rm c}$ is estimated as

$$\begin{aligned}\sigma^2(\zeta_{\rm c}) = 4&\sum_{i=N_{\rm m}}^{N_{\rm o1}}\left(\frac{\Delta\theta_i}{\theta_i}\right)^2\sigma^2_{g_+}(\theta_i) \\ &+\left(\frac{2}{1-\theta_{\rm o1}^2/\theta_{\rm o2}^2}\right)^2\sum_{i=N_{\rm o1}}^{N_{\rm o2}}\left(\frac{\Delta\theta_i}{\theta_i}\right)^2\sigma^2_{g_+}(\theta_i), \end{aligned} \quad (23)$$

where we have again assumed that the lensing measurement uncertainty is dominated by the intrinsic ellipticity noise, and $N_{\rm m}$, $N_{\rm o1}$, and $N_{\rm o2}$ are indices of the discretized radial bins corresponding to the radii: $\theta_{\rm m}$, $\theta_{\rm o1}$, and $\theta_{\rm o2}$ in equation (21), respectively.

The weak lensing measurements thus offer a unique and powerful method to estimate the projected mass of a cluster in a *model-independent way*.

5. Results

This section presents our main results, i.e., constraints on cluster masses and density profile shapes based on weak lensing measurements.

In the following we often show the results using different subsamples of clusters, each of which is defined according to the available information on the color and lensing properties. Table 5 gives a brief summary of the subsamples.

5.1. Tangential Distortion Profiles

All of our results are based on the tangential distortion profile of galaxy images for each cluster, which are shown in appendix 3 for all 30 clusters. Our X-ray luminous clusters at low redshifts ($z \simeq 0.2$) typically show the lensing distortion strength of $O(0.1)$ on small angular scales of $\sim 1'$. On these small scales, the nonlinear correction to the lensing shear, $g_+ = \gamma_+/(1-\kappa)$ [see equation (12)], must be included in the model fitting. The distortion signals decrease down to a few per cent on large scales of $\sim 10'$ (a few megaparsec scales). Impressively, a 1% shear signal is detected at $\gtrsim 2\,\sigma$ significance in most of our clusters (A 209, A 267, A 291, A 383, A 586, ZwCl 0740, ZwCl 0823, ZwCl 0839, A 611, A 697, A 750, A 963, A 1835, A 2219, A 2261, A 2345, RX J2129, A 2390, and A 2631), thus highlighting the unique capability of Subaru/Suprime-Cam data for accurate weak lensing measurements, thanks to its excellent image quality and depth (Broadhurst et al. 2005; and also see Kneib et al. 2003 for the space-based lensing observation). Given the trade-off between the radial dependence of the number of background galaxies and the distortion strengths of clusters at $z \simeq 0.2$, the distortion signals are most accurately measured around radii of $\sim 5'$.

The figures in appendix 3 also show the radial profile of the $g_\times$ distortion component for each cluster, providing a monitor of the systematic errors inherent in the lensing measurements, as described below equation (6). The $g_\times$ profiles are consistent with a null signal in most of radial bins, confirming the

Table 5. Summary of cluster subsamples.

Subsample	Number of clusters	Comments	Main results
All	30 clusters	As given in table 1	Appendix 3 for the mass map and shear profile
Complex	4 clusters	Complex mass maps	ZwCl 0823, A 689, A 750, and A 2345 (appendix 3)
Two filters	25 clusters	Color used to correct for dilution (including ZwCl 0823, A 689, and A 750)	—
Shear profile	22 clusters	Compared with spherical mass models	Figures 4, 5, 9, 10, and 11
NFW	19 clusters	Well fitted by NFW model	Figures 6, 7, and 8

* Column (1): name of cluster subsamples studied in this paper; Column (2): the number of clusters contained in each subsample; Column (3): comments used to define each subsample; Column (4): the figures and tables showing the main results derived from each subsample.

reliability of our lensing measurements.

5.2. *Two-Dimensional Mass Reconstruction*

To understand the broad-brush features of the cluster mass distributions, and thus to understand the distortion profiles better, we use the Kaiser and Squires (1993) algorithm to reconstruct the projected mass distribution in each cluster field, as shown in appendix 3.

Some clusters have depressions in the tangential distortion profiles spanning a few radial bins. When compared with the corresponding mass map, it becomes apparent that these depressions correspond to prominent structures in the annulus of the same radius — e.g., A 115 has a big depression in the distortion signals at $2'$–$3'$; the mass map contains three structures at this distance from the cluster center. The mass maps therefore provide a useful cross-check on the distortion profiles. However, in this paper we concentrate on a simple one-dimensional (i.e., tangential distortion profile) analysis as the first step in a series of papers on this sample. Future papers will employ more sophisticated modeling schemes, including substructures and halo triaxiality in order to model more precisely the full two- and three-dimensional structures of the cluster mass distributions (e.g., Oguri et al. 2010).

5.3. *Parametrized Distortion Profile Models*

First we use the tangential distortion profile of each cluster to constrain the spherical mass profile models discussed in section 4: NFW, SIS, and CIS models. Table 6 summarizes the best-fit parameters of each model. The clusters in brackets have been observed through just one filter, and the results are thus likely to be adversely affected by the dilution effect discussed in section 3. Note that the results are not shown for 4 clusters (ZwCl 0823, A 689, A 750, and A 2345) because the complex mass distribution revealed by the mass maps in appendix 3 strongly suggest that a spherically symmetric model is wholly inappropriate for these systems. The 4 clusters are a "complex cluster subsample" in table 5.

We quantify the goodness-of-fit of each model by using the significance probability, $Q(\nu/2,\ \chi^2/2)$, that the data gives as a poor fit as the observed value of χ^2 by chance (see subsection 15.2 in Press et al. 1992). Specifically, Q values greater than 0.1 indicate a satisfactory agreement between the data and the model; if $Q \gtrsim 0.001$, the fit may be acceptable, e.g., the measurement errors may be moderately underestimated; if $Q \lesssim 0.001$, the model may be called into question. Note that the Q value can be computed from the chi-square value and the degrees-of-freedom given in table 6. For simplicity we adopt the threshold $Q_{\rm th} = 0.1$ as the dividing line between acceptable ($Q > Q_{\rm th}$) and unacceptable ($Q < Q_{\rm th}$) fits to the measured profile. By this criterion three clusters (A 383, A 2219, and A 963) are not well fitted by any of the three models. Of the remaining 23 clusters, four (A 209, A 521, A 697, and A 1835) are not well fitted by an SIS model having $Q \simeq 6 \times 10^{-5}$, 0.03, 0.02, and 0.08, respectively, while either of CIS or NFW models gives an acceptable fit. In fact, as shown in appendix 3, these 4 clusters display a clear radial curvature in the measured distortion profile, which cannot be fitted by an unbroken power law of SIS. The remaining 19 clusters are all well-fitted by the three models. Note that we checked that, even if we include the 'poor-fit' 3 clusters in the analysis, the following results shown below are not largely changed. To be more precise, for example, the best-fit virial masses obtained from the χ^2-fitting of an NFW model to the stacked shear profile (see below for the details) are changed by less than 5%.

With the exception of the 4 clusters noted above, we cannot discriminate statistically between the three mass models — i.e., we cannot make a statistically robust choice as to which model is a better description of the observational data. This is partly because the statistical precision of the lensing measurements is insufficient, and partly because the radial range of the data is not wide enough to discriminate characteristic radial curvatures of CIS or NFW models from a single power law of the SIS model. Specifically, the weak lensing information at radii smaller than a few arcminutes is limited by the smaller number densities of background galaxies due to the small solid angle subtended by the annuli at these radii. There are several ways to overcome this limitation: (i) the statistical precision, especially on small scales, can be boosted by stacking the distortion profiles over cluster samples (see below), and (ii) the weak lensing information presented here can be combined with strong lensing constraints on small scales, allowing the cluster-by-cluster mass distribution to be measured to high precision over a wider range of radii (e.g., Kneib et al. 2003; Broadhurst et al. 2005). Strong lensing constraints are available for most of the clusters from Hubble Space Telescope observations (GO:11312; PI: G. P. Smith) plus ground-based spectroscopic follow-up (Richard et al. 2010). The improved constraints on the mass profile parameters for the joint fitting to the strong and weak lensing information will be presented elsewhere (G. P. Smith et al. in preparation).

We now turn to constraints on the virial mass of each cluster, $M_{\rm vir}$; from a theoretical perspective this is the most useful

Table 6. Best-fit mass profile parameters for SIS, CIS, and NFW models.*

Cluster	SIS		CIS			NFW		
	$\sigma_{\rm SIS}$ (km s^{-1})	χ^2_ν(d.o.f)	$\theta_{\rm E}$ ($'$)	θ_C ($'$)	χ^2_ν(d.o.f)	$M_{\rm vir}$ ($10^{14}h^{-1}\,M_\odot$)	$c_{\rm vir}$	χ^2_ν(d.o.f)
(1)	(2)	(3)	(4)	(5)	(6)	(7)	(8)	(9)
A 68	$869.03^{+70.82}_{-75.14}$	0.15(11)	$0.30^{+0.13}_{-0.09}$	$0.11^{+0.37}_{-0.11}$	0.13(10)	$5.49^{+2.56}_{-1.81}$	$4.02^{+3.36}_{-1.82}$	0.14(10)
A 115	$818.02^{+86.85}_{-86.08}$	0.66(12)	$0.27^{+0.19}_{-0.08}$	$0.06^{+0.58}_{-0.06}$	0.71(11)	$5.36^{+4.08}_{-2.45}$	$3.69^{+5.03}_{-2.04}$	0.75(11)
[ZwCl 0104]	$665.85^{+42.71}_{-57.95}$	1.29(12)	$0.14^{+0.03}_{-0.14}$	$0.00^{+0.06}_{-0.00}$	1.41(11)	$1.73^{+0.58}_{-0.47}$	$8.08^{+8.20}_{-3.43}$	1.35(11)
A 209	$918.76^{+34.06}_{-40.37}$	3.36(12)	$0.70^{+0.13}_{-0.11}$	$0.65^{+0.30}_{-0.21}$	0.89(11)	$14.00^{+3.31}_{-2.60}$	$2.71^{+0.69}_{-0.60}$	0.84(11)
RX J0142	$886.80^{+43.55}_{-46.56}$	0.56(12)	$0.27^{+0.06}_{-0.27}$	$0.03^{+0.08}_{-0.03}$	0.56(11)	$4.49^{+1.23}_{-1.01}$	$7.12^{+2.71}_{-1.89}$	0.49(11)
A 267	$778.05^{+45.65}_{-37.28}$	0.63(12)	$0.26^{+0.05}_{-0.05}$	$0.07^{+0.09}_{-0.06}$	0.54(11)	$3.85^{+1.08}_{-0.88}$	$6.00^{+2.11}_{-1.58}$	0.58(11)
A 291	$801.74^{+53.89}_{-51.28}$	1.17(12)	$0.42^{+0.17}_{-0.11}$	$0.50^{+0.59}_{-0.33}$	0.86(11)	$7.02^{+3.10}_{-2.06}$	$2.36^{+1.34}_{-0.94}$	0.87(11)
A 383	$875.19^{+34.37}_{-41.47}$	1.95(12)	$0.27^{+0.03}_{-0.27}$	<0.04	2.13(11)	$3.62^{+1.15}_{-0.86}$	$8.87^{+5.22}_{-3.05}$	2.78(11)
A 521	$789.23^{+43.63}_{-43.87}$	1.89(12)	$0.33^{+0.08}_{-0.07}$	$0.28^{+0.23}_{-0.15}$	1.50(11)	$5.85^{+1.45}_{-1.22}$	$3.06^{+1.01}_{-0.79}$	1.29(11)
A 586	$1035.32^{+40.04}_{-67.58}$	0.90(11)	$0.46^{+0.11}_{-0.46}$	$0.07^{+0.12}_{-0.07}$	0.87(10)	$7.37^{+2.89}_{-2.08}$	$8.38^{+3.52}_{-2.52}$	1.08(10)
ZwCl 0740	$726.93^{+66.62}_{-58.09}$	0.80(12)	$0.47^{+0.29}_{-0.17}$	$0.94^{+1.34}_{-0.67}$	0.54(11)	$5.89^{+5.48}_{-2.39}$	$2.85^{+2.03}_{-1.37}$	0.53(11)
[ZwCl 0839]	$766.05^{+57.14}_{-47.89}$	0.40(10)	$0.20^{+0.06}_{-0.02}$	<0.12	0.45 (9)	$2.91^{+1.08}_{-0.82}$	$7.24^{+5.04}_{-2.72}$	0.49(9)
A 611	$929.34^{+57.70}_{-45.26}$	1.45(12)	$0.33^{+0.08}_{-0.07}$	$0.11^{+0.19}_{-0.11}$	1.47(11)	$6.65^{+1.75}_{-1.42}$	$4.23^{+1.77}_{-1.23}$	1.37(11)
A 697	$1021.91^{+41.13}_{-45.14}$	2.07(12)	$0.56^{+0.11}_{-0.09}$	$0.38^{+0.23}_{-0.16}$	1.13(11)	$12.36^{+2.68}_{-2.21}$	$2.97^{+0.85}_{-0.69}$	1.04(11)
[A 963]	$816.53^{+37.85}_{-42.83}$	2.25(13)	$0.40^{+0.10}_{-0.08}$	$0.46^{+0.35}_{-0.23}$	1.72(12)	$6.96^{+2.17}_{-1.59}$	$2.57^{+1.00}_{-0.79}$	1.76(12)
A 1835	$1050.55^{+56.49}_{-41.65}$	1.65(11)	$0.61^{+0.14}_{-0.11}$	$0.46^{+0.27}_{-0.20}$	0.71(10)	$13.69^{+3.65}_{-2.86}$	$3.35^{+0.99}_{-0.79}$	0.56(10)
ZwCl 1454	$702.37^{+69.49}_{-67.89}$	0.91(11)	$0.20^{+0.10}_{-0.20}$	$0.09^{+0.28}_{-0.09}$	0.94(10)	$3.45^{+2.02}_{-1.36}$	$4.01^{+3.44}_{-1.96}$	0.99(10)
[A 2009]	$800.80^{+40.11}_{-49.15}$	1.20(12)	$0.31^{+0.08}_{-0.07}$	$0.13^{+0.18}_{-0.11}$	1.14(11)	$3.86^{+1.20}_{-0.93}$	$6.59^{+2.40}_{-1.71}$	0.89(11)
ZwCl 1459.4	$864.90^{+53.43}_{-71.78}$	1.21(12)	$0.28^{+0.08}_{-0.28}$	$0.04^{+0.12}_{-0.04}$	1.28(11)	$4.40^{+1.50}_{-1.20}$	$6.55^{+3.34}_{-2.18}$	1.17(11)
RX J1720	$879.13^{+61.09}_{-54.04}$	0.52(12)	$0.28^{+0.09}_{-0.03}$	<0.14	0.57(11)	$4.07^{+1.65}_{-1.22}$	$8.73^{+5.60}_{-3.08}$	0.57(11)
A 2219	$1132.87^{+43.65}_{-58.12}$	1.73(12)	$0.47^{+0.08}_{-0.47}$	<0.07	1.89(11)	$9.11^{+2.54}_{-2.06}$	$6.88^{+3.42}_{-2.16}$	2.26(11)
A 2261	$1078.32^{+54.66}_{-29.73}$	0.77(12)	$0.50^{+0.09}_{-0.08}$	$0.08^{+0.11}_{-0.07}$	0.68(11)	$9.49^{+2.01}_{-1.69}$	$6.04^{+1.71}_{-1.31}$	0.67(11)
RX J2129	$879.92^{+62.12}_{-52.16}$	0.52(12)	$0.33^{+0.12}_{-0.09}$	$0.15^{+0.33}_{-0.15}$	0.48(11)	$6.71^{+2.73}_{-1.96}$	$3.32^{+2.16}_{-1.34}$	0.56(11)
A 2390	$951.38^{+55.34}_{-31.23}$	1.05(12)	$0.49^{+0.08}_{-0.07}$	$0.13^{+0.09}_{-0.07}$	0.53(11)	$8.20^{+1.93}_{-1.63}$	$6.20^{+1.53}_{-1.28}$	0.61(11)
A 2485	$777.49^{+60.07}_{-64.03}$	0.82(12)	$0.28^{+0.11}_{-0.08}$	$0.17^{+0.34}_{-0.16}$	0.78(11)	$4.56^{+1.84}_{-1.38}$	$3.52^{+2.24}_{-1.44}$	0.77(11)
A 2631	$959.71^{+50.90}_{-35.71}$	0.86(12)	$0.30^{+0.04}_{-0.30}$	<0.04	0.93(11)	$5.24^{+1.15}_{-0.98}$	$7.84^{+3.54}_{-2.28}$	1.09(11)

* Column (1): cluster name (clusters with name in brackets have only one filter data available, and the rest has two filter data); Column (2): best-fit velocity dispersion for SIS model [equation (16)]; Column (3): reduced χ^2 for the best-fit SIS model, and the degrees-of-freedom in parentheses; Column (4): the Einstein radius parameter for the CIS model [see equation (19)]; Column (5): The core radius; Column (6): the reduced χ^2; Column (7): best-fit virial mass for the NFW model [equation (14)]; Column (8): the best-fit NFW concentration parameter; Column (9): the reduced χ^2.

cluster mass measurement. In table 6 we list the best-fit virial mass and the $1\,\sigma$ statistical uncertainties obtained from the NFW model fits. The marginalized error on one parameter, obtained by projecting the confidence region in a higher dimensional parameter space onto one particular parameter axis, can be obtained by measuring the range of the parameter that satisfies $\Delta\chi^2 \leq 1$ while varying other parameter(s) (e.g., see subsection 15.3 in Numerical Recipes by Press et al. 1992).

In figure 4 we compare the virial masses derived from the NFW models with the masses derived from the SIS models, where the latter are estimated by inserting the best-fit $\sigma_{\rm SIS}$ values from table 6 into equation (17). Note that here we consider only clusters with data available in two filters, which corresponds to the subsample named "shear profile" in table 5 consisting of 22 clusters (25 clusters with two filter data minus 3 clusters showing the complex mass distribution). The two mass estimates agree within the uncertainties for 13 out of 22 clusters. Adopting a fixed slope of unity, the relationship between the two model-dependent mass measurements is found to be $M_{\rm vir}^{\rm NFW}/M_{\rm vir}^{\rm SIS} = 1.20 \pm 0.25$, where the quoted uncertainty is the scatter around the mean, and is dominated by the measurement errors. Nevertheless, the SIS mass is systematically smaller than the NFW mass by $\sim 20\%$, implying that the model choice does influence the mass measurement. We defer consideration of the origin of the difference between the SIS and NFW mass estimates to subsection 5.5, in which we

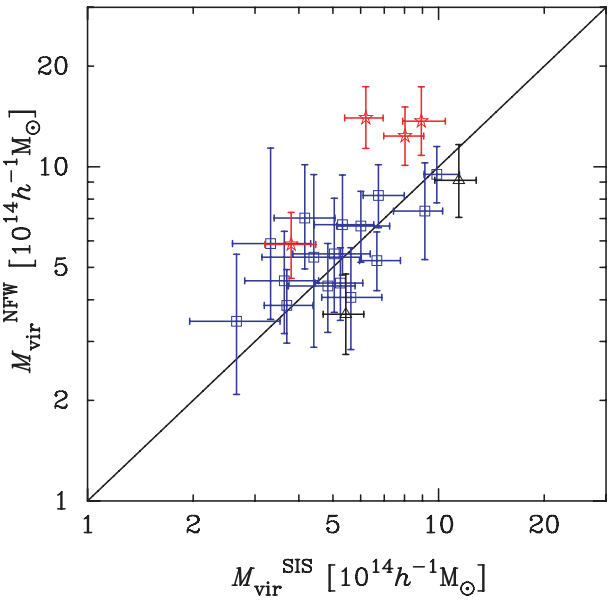

Fig. 4. Comparison of the virial mass estimates derived from the fitting of SIS and NFW models to the tangential distortion profile measured for each of the 22 clusters that have color information of galaxies (to define the red + blue galaxy sample). The clusters are classified into 3 different groups based on the results of table 6: the triangle symbols with error bars show the clusters for which any of the SIS, CIS, and NFW models does not give an acceptable fit (A 383 and A 2219); the star symbols show clusters for which an SIS model is disfavored compared with CIS and NFW models (A 209, A 521, A 697, and A 1835); the square symbols denote the other clusters for which all the three modes give an acceptable fit. While the star symbols show a significant smaller mass from SIS than that from NFW, an agreements within 1σ error bars can be found for other clusters, but the scatter around the relation $M_{\rm vir}^{\rm SIS}$–$M_{\rm vir}^{\rm NFW}$ is rather substantial.

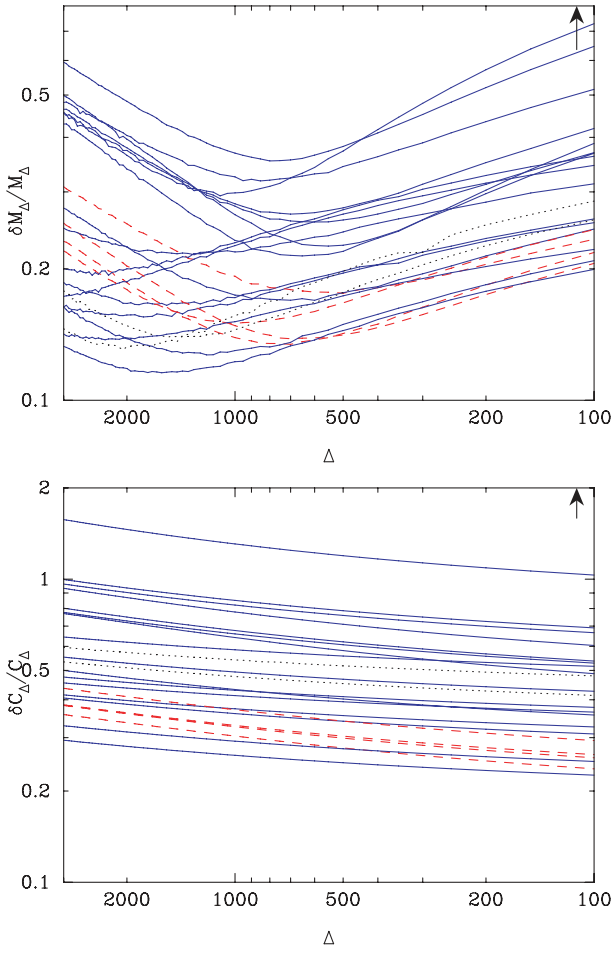

Fig. 5. Upper panel: Relative accuracies of the cluster mass estimations, from the NFW model fitting, as a function of the average over-density assumed, Δ, by which the enclosed mass M_Δ is defined based on equation (14). The solid, dashed, and dotted curves show the clusters that are marked with the square, star and triangle symbols in figure 4, respectively. For most clusters, the cluster mass can be estimated at a best precision when assuming $\Delta \simeq 500$–2000. The arrow denotes the virial over-density at $z \simeq 0.2$: $\Delta_{\rm vir} \simeq 110$. Lower panel: The similar plot, but for the concentration parameter.

study stacked distortion profiles.

The fractional error on virial masses in table 6 is typically 20%–30%. The precision to which cluster masses can be measured is central to attempts to measure the intrinsic scatter in the cosmological scaling relations. We therefore explore whether alternative definitions of the cluster mass yield similar or, hopefully, greater precision.

Despite its theoretical appeal, the virial mass is neither a unique nor necessarily the most observationally appealing choice of the cluster mass measurement. There are many alternative cluster mass definitions, the use of which depends to a large extent on the nature of observational data available (strong lensing, weak lensing, X-ray, SZ) to constrain the cluster mass. In figure 5 we plot the variation of the fractional error on the cluster mass and the concentration with the over-density, Δ, at which the parameters are defined. More precisely, for each Δ, we first express the NFW model in terms of the two parameters (c_Δ, M_Δ), instead of their virial counterparts, and then estimate the best-fit parameters and statistical uncertainties from the model fitting. While the best-fit NFW model is unchanged for any Δ, given the measured distortion profile, the statistical uncertainties in the parameters M_Δ and c_Δ change because the variations in the NFW profile are given with respect to r_Δ corresponding to the enclosed over-density, Δ.

The upper panel of figure 5 indeed shows that the accuracies of the cluster mass determination do vary with Δ. Interestingly, the optimal over-density is $\Delta \simeq 500$–2000 for the majority of our clusters. This result can be understood as follows. These clusters are found to be well fitted by an NFW model with concentration $c_{\rm vir} \lesssim 5$, which roughly matches the ΛCDM simulation predictions for cluster-scale halos (e.g., Bullock et al. 2001; Dolag et al. 2004; Neto et al. 2007). Given the cluster redshifts ($z \simeq 0.2$) and the number densities of background galaxies available from Subaru, the weak lensing signals have a maximum signal-to-noise ratio over a range of radii corresponding to the over-density, $\Delta \simeq 500$–1000.

The lower panel shows the results for the concentration parameter. The concentration parameter is not as tightly constrained as the mass, with the fractional error being in excess of 20% in every case, at all Δ. The precision does increase slowly with decreasing Δ or increasing the pivot radius, r_Δ. This reflects the fact that the larger pivot radius,

r_Δ, gives a greater leverage when measuring the curvature of an NFW profile with respect to the scale radius, $r_s\,(\equiv r_\Delta/C_\Delta)$, yielding a superior precision on the concentration parameter for a smaller Δ.

5.4. *The $M_{\rm vir}$–$c_{\rm vir}$ Relation*

Numerical simulations based on the CDM model have revealed that the two parameters of NFW halos, e.g., $c_{\rm vir}$ and $M_{\rm vir}$, are correlated, i.e., the halo concentration is a weakly decreasing function of mass (e.g., Bullock et al. 2001). Such a correlation is expected to naturally arise from the nature of hierarchical clustering. According to the CDM structure formation scenario, less massive halos first form, and then more massive halos form as a result of mergers of smaller halos and/or mass accretion onto halos. Hence, since the progenitors of more massive halos should have formed at lower redshifts at which the mean background mass density is lower, more massive halos at a given observing redshift tend to possess a less centrally concentrated profile, given the fact that the mean over-density within the virial radius is fixed for all halos. Thus, the properties of the halo profile contain rich information on cosmological models as well as the mass assembly history of halos.

We can therefore use our large cluster sample to explore whether such a correlation between $c_{\rm vir}$ and $M_{\rm vir}$ is present in real clusters, concentrating on 19 clusters (the "NFW" subsample in table 5) — i.e., we exclude 3 clusters from the 22 with 2-filter data: A 383 and A 2219 are not well fit by an NFW profile, and ZwCl 0740 because its redshift is estimated photometrically. Figure 6 shows how these 19 clusters are distributed in the $(c_{\rm vir}, M_{\rm vir})$ plane. Interestingly, a visual inspection of the data suggests a marginal trend that the measured $c_{\rm vir}$ becomes smaller for more massive halos, although the scatter is large. It is also interesting to note that none of our morphologically unbiased X-ray selected sample of clusters, including those with the highest masses ($\gtrsim 10^{15}\,M_\odot$), show very high concentrations of $c_{\rm vir} \gtrsim 10$ as have been found for some strong lensing clusters (e.g., Gavazzi et al. 2003; Kneib et al. 2003; Broadhurst et al. 2005, 2008).

We quantify the possible trend by fitting the following function to the $c_{\rm vir}$–$M_{\rm vir}$ data points:

$$c_{\rm vir} = c_{\rm N}\left(\frac{M_{\rm vir}}{10^{14}h^{-1}M_\odot}\right)^{-\alpha}. \quad (24)$$

This form is motivated by simulation-based studies (e.g., Bullock et al. 2001) and specified by two free parameters: the normalization, $c_{\rm N}$, and the mass slope, α. The best-fit parameters and $1\,\sigma$ uncertainties are: $c_{\rm N} = 8.75^{+4.13}_{-2.89}$ and $\alpha = 0.40 \pm 0.19$. Thus, the mass scaling of $c_{\rm vir}(M_{\rm vir})$ is marginally detected at a $2\,\sigma$ level. Our results are more significant than the earlier weak-lensing results (Comerford & Natarajan 2007; Mandelbaum et al. 2008).

Note that the two parameters $M_{\rm vir}$ and $c_{\rm vir}$ are correlated for each cluster: the measured shear profile can be explained by NFW profiles with larger $M_{\rm vir}$ and smaller $c_{\rm vir}$ than the best-fit values and vice versa. We therefore checked whether this intrinsic correlation might be exaggerating significance of our result. We randomly draw $M_{\rm vir}$ and $c_{\rm vir}$ for each cluster from the respective posterior distributions, and re-calculate the best-fit $M_{\rm vir}$–$c_{\rm vir}$ 30000 times. From the mean relation derived from these samples, and the scatter around the mean, we estimate that the significance of our detection of anti-correlation between mass and concentration remains unchanged, and conclud that the intrinsic correlation has a negligible effect on our results.

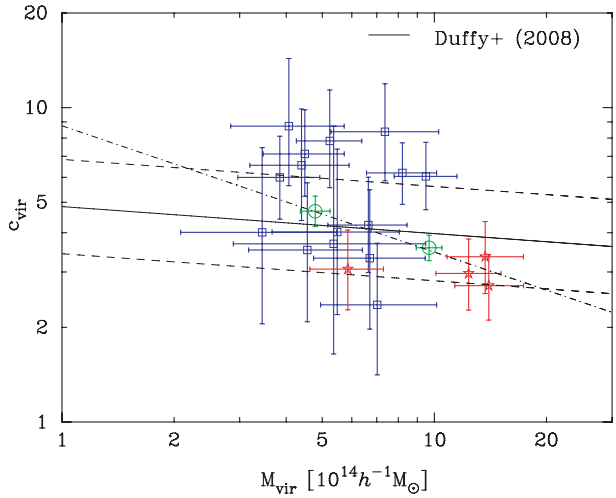

Fig. 6. The observed distribution of the concentration parameters $c_{\rm vir}$ as a function of the cluster masses $M_{\rm vir}$, for 19 clusters that are better fitted by NFW than SIS models. The solid line indicates the median relation found from the CDM simulations for the WMAP5 cosmological model, while the region enclosed within the dashed lines correspond to the range of $\sigma(\log_{10}c_{\rm vir}) = 0.1$ within which most of simulated clusters are distributed (Duffy et al. 2008). The dotted-dashed line denotes the best-fit model of $c_{\rm vir} = c_{\rm N}(M_{\rm vir}/10^{14}\,h^{-1}\,M_\odot)^{-\alpha}$ to the cluster distribution that is given by $c_{\rm N} = 8.55$ and $\alpha = 0.40$. The two circle symbols are the results for the stacked lensing signals obtained from the low- and high-mass samples that are divided with mass threshold, $M_{\rm vir,thresh} = 6 \times 10^{14}\,h^{-1}\,M_\odot$ (see subsection 5.5 for the details). The star and square symbols are as in figure 4.

We also checked whether the parameter fitting above causes a bias in the best-fit slope, α, of the scaling relation, $c_{\rm vir}(M_{\rm vir})$, by using simulated data. First, we generate 3000 simulated catalogs of the tangential shear profiles for 19 clusters including the errors at all radial bins that are modeled to reproduce the measured errors. In making these simulations, the mass and concentration of each cluster are randomly chosen from the observed ranges of $2 \le M_{\rm vir}/(10^{14}\,h^{-1}\,M_\odot) \le 15$ and $2 \le c_{\rm vir} \le 10$, and the redshift of all clusters is fixed to a single redshift of $z_{\rm l} = 0.23$, corresponding to the mean redshift of the 19 Subaru clusters. Note that the simulated cluster catalogs have no intrinsic scaling relation between $c_{\rm vir}$ and $M_{\rm vir}$ on average, i.e., $\alpha = 0$. We then estimated the $M_{\rm vir}$ and $c_{\rm vir}$ parameters for each simulated cluster from the shear profile fitting to an NFW model, and made a fitting of the distribution of $M_{\rm vir}$ and $c_{\rm vir}$ for 19 clusters to the model $c_{\rm vir}$–$M_{\rm vir}$ relation [equation (24)]. From the 3000 catalogs we found that the estimated slope of $c_{\rm vir}(M_{\rm vir}) \propto M_{\rm vir}^{-\alpha}$ tends to be slightly biased as $\langle\alpha\rangle = 0.06$ from the input value, $\alpha = 0$. The origin of this bias can again be ascribed to the degeneracy between the mass and the concentration for the shear profile fitting. Nevertheless, the amount of the bias is smaller than the $1\,\sigma$ statistical errors of α estimation, $\sigma(\alpha) = 0.19$, and therefore we conclude that this

Table 7. Best-fit parameters for the mass–concentration relation of $c(M) = c_{\rm N}(M/10^{14}\,h^{-1}\,M_\odot)^{-\alpha}$.*

	$c_{\rm N}$	α	$\sigma(\log_{10}c)$
$c_{\rm vir}(M_{\rm vir})$	$8.75^{+4.13}_{-2.89}$	$0.40\ \pm 0.19$	0.17
Duffy+08: $c_{\rm vir}(M_{\rm vir})$	4.96	0.086	$\sim$0.15
Buote+07: $c_{\rm vir}(M_{\rm vir})$	7.5 ± 0.33	0.172 ± 0.026	$\sim$0.1
$c_{200}(M_{200})$	$5.75^{+2.47}_{-1.90}$	$0.37^{+0.20}_{-0.21}$	0.18
Duffy+08: $c_{200}(M_{200})$	3.71	0.089	$\sim$0.15

* The row labeled as "Duffy + 08" shows the results obtained from numerical simulations for the WMAP 5-year cosmological model in Duffy et al. (2008), corrected for clusters at $z = 0.24$, the mean redshift of our sample clusters. The row labeled as "Buote + 07" shows the results obtained from the X-ray data sets of 39 galaxy- and cluster-scale halos in Buote et al. (2007).

effect is also insignificant.

The observed concentration–mass relation can be compared with the theoretical predictions based on large N-body simulations. The solid line in figure 6 shows the median relation obtained by Duffy et al. (2008, hereafter Duffy08), and given by $(c_{\rm N}, \alpha) = (4.96, 0.086)$ in equation (24), where the relation is obtained assuming the concordance ΛCDM model that is constrained by the WMAP 5-year data. Note that the redshift dependence of $c_{\rm vir}(M_{\rm vir})$ is corrected to match halos at the mean redshift, $z = 0.23$, based on the fitting results in table 1 of Duffy08. The observed concentrations of $M_{\rm vir} \sim 5 \times 10^{14}\,M_\odot$ clusters, i.e., $c_{\rm vir} \sim 5$, are consistent with the prediction; however, the observed slope is steeper than the prediction, albeit at a very modest statistical significance. It is also important to note that the clusters (star symbols) that are well fitted by an NFW profile have low concentrations of $c_{\rm vir} \sim 3$, while the distribution of clusters (squares) for which we cannot discriminate between CIS and NFW models extends to much large concentrations.

The region enclosed by the two dashed lines shows the range of $\sigma(\log_{10}c_{\rm vir}) = 0.1$ in which simulated clusters are typically distributed, as shown in Duffy08 (also see Jing 2000). The scatter for the observed concentrations is given by $\sigma(\log_{10}c_{\rm vir}) \simeq 0.17$, which is estimated by weighting the cluster distribution with the inverse square of the statistical error of each cluster concentration. The observed statistical errors are so large that it's not possible to say whether there is any intrinsic scatter contribution.

Our results for the concentration distribution are summarized in table 7, together with the predictions of Duffy08 and Buote et al.'s (2007) observational results based on X-ray data. Note that the X-ray results are derived using a much wider range of halo masses than our results — from galaxy to galaxy cluster scales. Both the lensing and X-ray observations imply a significantly higher normalization, $c_{\rm N}$ than the simulations, and also a steeper dependence (higher α) on the halo masses. Comparing the lensing and X-ray results, the lensing results indicate a steeper dependence than the X-ray results, but the discrepancy is not yet conclusive due to the large statistical errors. A further, careful study will be needed to resolve these possible discrepancies.

In figure 7 we show the one-dimensional distribution of the concentration parameters for the 19 clusters in figure 6. The mean values and error bars in each bin are computed from 3000 Monte Carlo redistributions of the clusters, assuming that the halo concentration of each cluster obeys the Gaussian distribution with the width given by the measurement error $\sigma(c_{\rm vir})$. Note that the data points in different bins are correlated. Interestingly, the observed distribution contains a dip at $c_{\rm vir} \simeq 4$, suggesting that a single lognormal model distribution may not fit the distribution very well. The solid and dashed curves show the results of fitting two and one lognormal distributions, respectively. Given the large error bars, the two models both give an acceptable fit to the data: the two lognormal distributions (additional two model parameters compared to the one lognormal distribution) improve the χ^2 value only by $\Delta\chi^2 \simeq 0.9$. Nevertheless, it is interesting to note that the simulations have found similar structure in the distribution of the predicted concentrations (Jing 2000; Shaw et al. 2006; Neto et al. 2007; Duffy08). It is argued in these studies that the physical origin of the structure lies in the dynamical

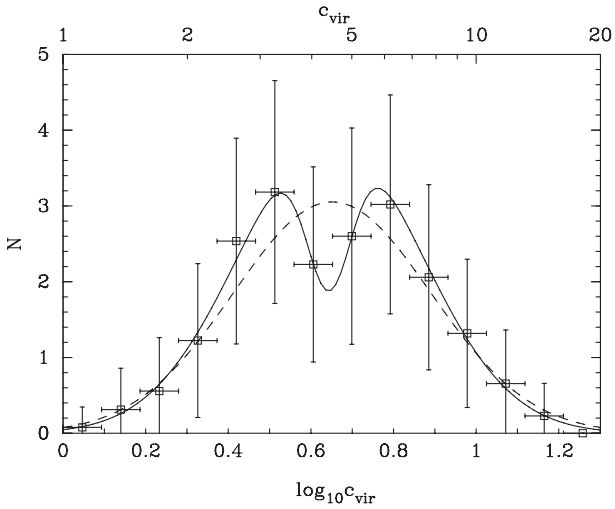

Fig. 7. One-dimensional distribution of the observed concentration parameters for 19 clusters, obtained by projecting the cluster distribution in figure 6 onto the axis of $\log_{10}c_{\rm vir}$. The square symbols and the error bars in each bin are computed from the mean and variance of 3000 Monte Carlo redistributions of the $c_{\rm vir}$ distribution, taking into account the uncertainties in $c_{\rm vir}$ for each cluster. The solid and dashed curves show the best-fit models of two- and one-lognormal distributions, respectively.

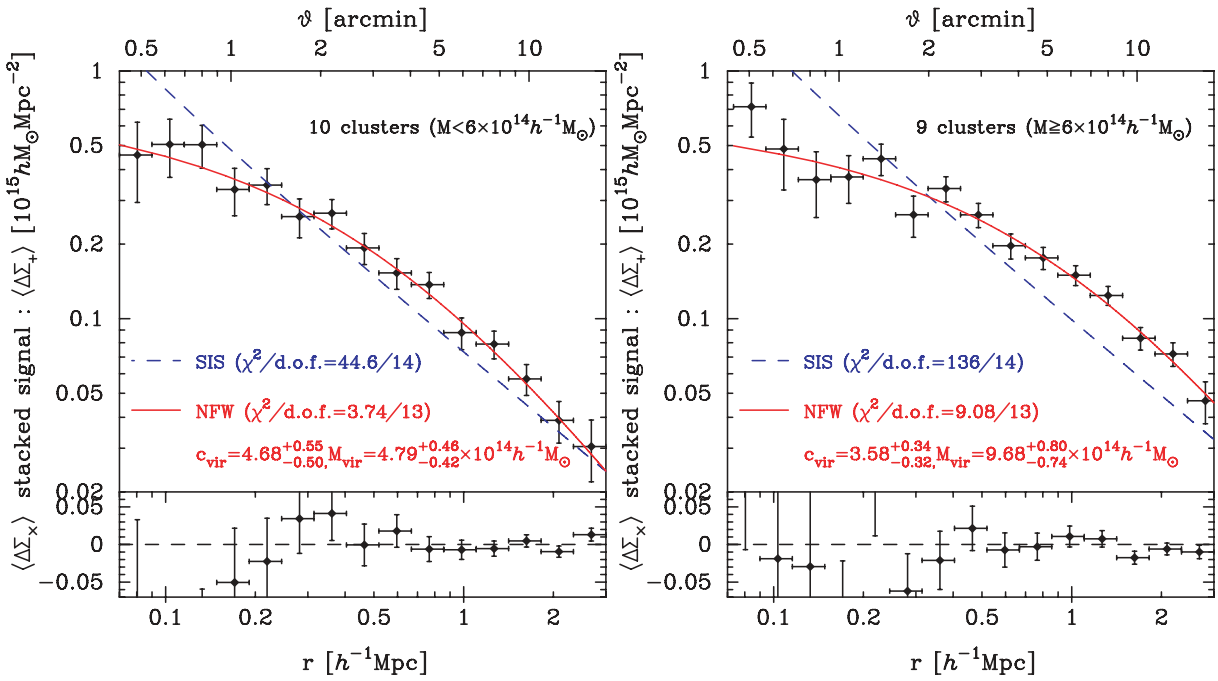

Fig. 8. Left panel: The mean distortion profile with 1σ statistical uncertainties as a function of the projected radius, which is obtained by stacking the distortion signals for 10 clusters that are selected with the virial masses $M_{\rm vir} \leq 6 \times 10^{14}\,h^{-1}\,M_{\odot}$ from 19 clusters in figure 6. Note that the distortion profile is plotted in units of the projected mass density, and the projected radius is computed from the weighted mean redshift of clusters. The dashed and solid curves are the best-fit SIS and NFW models, respectively. Right panel: A similar plot, but for 9 halos with $M_{\rm vir} > 6 \times 10^{14}\,h^{-1}\,M_{\odot}$. For both results, the SIS model is strongly disfavored: $\Delta\chi^2 \equiv \chi^2_{\rm SIS,min} - \chi^2_{\rm NFW,min} \simeq 41$ and 127 for the low- and high-mass cluster samples, respectively. The combined results also show 2σ-level evidence that the NFW concentration is greater for more massive halos, which is exactly consistent with the result in figure 6.

status of the clusters: more relaxed clusters tend to have high concentrations, and vice versa (also see Smith & Taylor 2008). It will therefore be important to further explore the concentration distribution by enlarging the sample size of clusters.

5.5. *Stacked Lensing Signal*

In this section we study the stacked weak-lensing signal of 19 clusters in figure 6. This approach has several important advantages. First, the *average* distortion profile is less sensitive to substructures within and asphericity of the individual cluster mass distributions and also to uncorrelated large-scale structure along the same line-of-sight. This is because these "contaminating signals" are averaged out via the stacking, under the assumption that the universe is *statistically* homogeneous and isotropic. Second, stacking should boost the signal-to-noise ratio of the distortion signal at very small and large radii. The signal-to-noise ratio at small radii is limited for a single cluster because the solid angle subtended by a radial bin shrinks at small radii, thus reducing the number of galaxies over which the mean distortion signal is calculated. Hence, the signal-to-noise ratio suffers despite the signal peaking in these regions. On the other hand, at large radii, the binned solid-angle is much larger, helping to maintain the signal-to-noise; however, the signal becomes very small, and thus the signal-to-noise ratio declines. As discussed in subsection 5.3, the signal-to-noise ratio is optimized at intermediate radii. Therefore, stacking helps to improve the signal-to-noise as a function of the radius, thus enabling a clearer investigation of (i) the curvature of the density profile, which is a characteristic signature of the NFW prediction, helping us potentially to address the nature of dark matter (e.g., Yoshida et al. 2000), and (ii) the distribution of mass outside the virial radius to address whether or not the outer slope of the NFW profile, $\rho \propto r^{-3}$, continues outside the virial radius (e.g., Bertschinger 1985; Busha et al. 2003).

To study the stacked lensing signal, we divide the 19 clusters into two mass bins, based on whether the NFW model fits to individual clusters yielded a virial mass estimate of greater than or less than $M_{\rm vir} = 6 \times 10^{14}\,h^{-1}\,M_{\odot}$. This results in two sub-samples of 10 low-mass and 9 high-mass clusters. Figure 8 shows the average distortion profile as a function of the projected radius in the physical length scale. Note that the effect of different cluster redshifts was taken into account by using the weighting method in terms of the lensing efficiency functions of averaging clusters (Mandelbaum et al. 2006; also see Sheldon et al. 2009a), and the projected radius is computed from the weighted mean redshift of the sampled clusters. However, we checked that, even if we use the single lensing efficiency for the mean cluster redshift, the results remains almost unchanged due to the narrow redshift coverage of our cluster samples. Note that the mean lens redshifts are $\langle z_{\rm l}\rangle = 0.251$ and 0.236 for the low- and high-mass samples, respectively.

First, unsurprisingly, the stacked profiles yield *very* significant detections: the total signal-to-noise ratios are $S/N = 24$ and 30 for the low- and high-mass samples, respectively. Second, the lensing distortion signals are recovered over a wide

range of radii, from $70\,h^{-1}$ kpc to $3\,h^{-1}$ Mpc scales, spanning a factor of 50 in radius. Note that the outer radial boundary corresponds to the size of the Suprime-Cam's FoV for clusters at $z \simeq 0.24$, and is a factor ~ 1.5–2 beyond the cluster virial radii determined from the individual NFW model fits. A visual inspection of the stacked profiles also reveals that they are clearly not described by a single power-law model, displaying very obvious curvature, reminiscent of the NFW prediction. We therefore fitted SIS and NFW models to the stacked profiles, and show that the solid and dashed curves are the best-fit NFW and SIS models, respectively. The non-linear corrections in the measured reduced shear are taken into account in these fits, following the method in Mandelbaum et al. (2006); however, for simplicity we ignore uncertainties in the alignment of the cluster halo centers; we will discuss this effect in detail in sub-subsection 5.7.3. Now, very clearly the SIS model is strongly disfavored at $6\,\sigma$ and $11\,\sigma$ significance for the low- and high-mass samples, respectively, estimated from the difference between the χ^2 values of the best-fit NFW and SIS models: $\Delta\chi^2 \equiv \chi^2_{\rm SIS,min} - \chi^2_{\rm NFW,min} \simeq 41$ and 127, respectively. The NFW model gives an acceptable fit to the data (the CIS model is also acceptable).

The best-fit NFW parameters are $c_{\rm vir} = 4.68^{+0.55}_{-0.50}$, $M_{\rm vir} = 4.79^{+0.46}_{-0.42} \times 10^{14}\,h^{-1}\,M_\odot$ for the low-mass sample, and $c_{\rm vir} = 3.58^{+0.34}_{-0.32}$, $M_{\rm vir} = 9.68^{+0.80}_{-0.74} \times 10^{14}\,h^{-1}\,M_\odot$ for the high-mass sample, i.e., relative accuracies of about 10% for both $c_{\rm vir}$ and $M_{\rm vir}$, an improvement by a factor of 2–5 compared to the individual cluster constraints in figure 5. Comparing the two mass bins reveals that the concentration parameter appears to be greater for the low-mass sample than for the high-mass one at 2σ significance. It is re-assuring that this difference is exactly consistent with the relation found from the individual cluster analysis of 19 clusters in figure 6, even though the individual-cluster and stacked analyses involve non-trivial differences in the averaging procedures that are not necessarily equivalent for real clusters (e.g., due to non-spherical mass distribution and substructures).

The measured distortion profile outside the virial radius is consistent with the outer slope of the NFW profile, i.e., we could not find any evidence that the mass distribution outside the virial radius, which mostly contains gravitationally unbound mass, declines more rapidly than is predicted by NFW. This is in contrast to the sharply truncated profile at the virial radius discussed by Busha et al. (2005; see also Takada & Jain 2003; Prada et al. 2006; Baltz et al. 2007). The stacked distortion profiles also do not show any signature of associated large-scale structures, such as filamentary structures surrounding the clusters, unlike the SDSS stacked lensing results (Johnston et al. 2007). However, the large-scale structure lensing signals are only expected to dominate at projected radii greater than ~ 10 Mpc. Hence, by further extending the observed fields to obtain a more radial range covered, it would be interesting to explore the lensing signals outside the virial radius to test the CDM structure formation scenarios sitting more in the linear regime.

Finally, we note that the results presented in this section help to explain the systematic difference between the virial mass estimates between the SIS and NFW model fits to the individual clusters, as found in figure 4. The virial mass estimates are dominated by the integral of the density profile on large radii around the virial radius. Figure 7 reveals that when an SIS model is fitted to distortion profile data from an NFW halo, the inability of the SIS model to capture the curvature of the distortion profile causes it to underestimate the amount of mass in the cluster on large radii. This short-fall on large scales is compensated to some extent, but not entirely by the overestimation of the cluster mass on small scales.

5.6. *Results for Model-Independent Mass Estimates*

We now turn to model-independent estimates of the projected mass of each cluster, using the $\zeta_{\rm c}$-method described in subsection 4.2.

The first three columns of table 8 list, for the 22 clusters in table 6, the aperture masses within several different radii. Note again that these 22 clusters have color information — the results in table 6 are therefore based on the red + blue background galaxy samples. The statistical accuracy of the aperture mass within a given aperture radius $\theta_{\rm m}$ is determined by the measurement accuracy of the $\zeta_{\rm c}$-statistics [see equation (21)] that is computed by integrating the measured distortion profile over the annulus taken outside the aperture radius, $\theta_{\rm m}$. Therefore, the aperture mass accuracy decreases with increasing aperture radius, because at larger radii the cluster lensing signal becomes weaker, and thus noisier. Table 8 shows that, at the virial radius and r_{500}, the typical accuracies are $\sigma(M_{\rm 2D})/M_{\rm 2D} \sim 50\%$ or 25%, respectively. Note that the aperture mass at the virial radius is somewhat sensitive to the choice of the control annulus [$\theta_{\rm o1} \le \theta \le \theta_{\rm o2}$ — see equation (21)]. However the $M_{\rm 2D}$ estimates vary within the $1\,\sigma$ statistical errors quoted in table 6 when the control annulus is varied — this is therefore not a dominant source of errors. The second column shows the results for a fixed projected radius, $r = 500\,h^{-1}$ kpc.

For a comparison we also list the model-dependent results for the three-dimensional masses obtained from the NFW model fitting, at several over-densities: $\Delta = 2500$, 500, and 200 (the virial mass and the errors were already given in table 6). The masses M_{2500} and M_{500} are often used when estimating cluster masses based on X-ray observations (e.g., Vikhlinin et al. 2006, 2009a).

Figure 9 compares the aperture masses with the three-dimensional best-fit NFW masses for 22 clusters. The upper panel shows a comparison at the virial radius — on this scale the mass estimates agree within the error bars, the scatter around the equality line being dominated by the measurement error. A formal fit to the data points, holding the slope of the line fixed at unity, gives a best-fit ratio of $M_{\rm 2D}(<\theta_{\rm vir})/M^{\rm NFW}_{\rm vir} = 1.32 \pm 0.19$. Note that the fit is done in the linear scale of masses, rather than the log space. On average the aperture masses are therefore $\sim 32\%$ higher than the 3D NFW masses, at $\sim 2\,\sigma$ significance. A comparison at r_{500} is shown in the lower panel. In this case a systematic excess of aperture masses over 3D NFW masses is immediately obvious for most of the clusters. Repeating the fit described above to the data at r_{500} gives a ratio of $M_{\rm 2D}(<\theta_{500})/M^{\rm NFW}_{500} = 1.46 \pm 0.12$, i.e., a 46% difference at $\sim 4\,\sigma$ significance.

Table 8. Weak-lensing mass estimates for the 22 clusters.*

Cluster (1)	$M_{2D}(<500\,h^{-1}\mathrm{kpc})$ (2)	$M_{2D}(<\theta_{500})$ (3)	$M_{2D}(<\theta_{vir})$ (4)	M_{2500}^{NFW} (5)	M_{500}^{NFW} (6)	M_{200}^{NFW} (7)
A 68	2.62 ± 0.69	4.17 ± 1.13	7.87 ± 3.02	$1.00^{+0.42}_{-0.43}$	$2.92^{+0.86}_{-0.75}$	$4.45^{+1.75}_{-1.35}$
A 115	3.23 ± 1.00	5.20 ± 1.82	8.79 ± 6.61	$0.86^{+0.46}_{-0.47}$	$2.70^{+1.15}_{-0.93}$	$4.24^{+2.60}_{-1.79}$
A 209	4.71 ± 0.49	8.40 ± 1.11	13.16 ± 4.00	$1.53^{+0.33}_{-0.33}$	$6.19^{+0.95}_{-0.86}$	$10.62^{+2.17}_{-1.81}$
RX J0142	2.36 ± 0.62	3.97 ± 0.98	5.60 ± 2.91	$1.37^{+0.22}_{-0.22}$	$2.85^{+0.60}_{-0.53}$	$3.86^{+0.98}_{-0.82}$
A 267	1.87 ± 0.45	3.14 ± 0.68	3.94 ± 1.93	$1.01^{+0.18}_{-0.18}$	$2.31^{+0.48}_{-0.43}$	$3.23^{+0.82}_{-0.69}$
A 291	2.55 ± 0.48	3.79 ± 0.84	5.23 ± 3.12	$0.63^{+0.30}_{-0.27}$	$2.88^{+0.70}_{-0.62}$	$5.19^{+1.80}_{-1.34}$
A 383	2.54 ± 0.45	3.72 ± 0.79	8.69 ± 2.53	$1.23^{+0.17}_{-0.17}$	$2.37^{+0.51}_{-0.43}$	$3.11^{+0.88}_{-0.69}$
A 521	3.85 ± 0.61	5.35 ± 1.15	9.29 ± 4.58	$0.77^{+0.22}_{-0.22}$	$2.78^{+0.51}_{-0.48}$	$4.58^{+1.00}_{-0.88}$
A 586	3.75 ± 0.99	7.54 ± 2.53	12.69 ± 8.57	$2.41^{+0.45}_{-0.42}$	$4.74^{+1.40}_{-1.14}$	$6.29^{+2.26}_{-1.69}$
ZwCl 0740	2.25 ± 0.48	2.77 ± 0.85	6.31 ± 3.66	$0.64^{+0.27}_{-0.26}$	$2.55^{+1.11}_{-0.75}$	$4.36^{+3.14}_{-1.60}$
A 611	3.86 ± 0.59	5.78 ± 1.11	8.77 ± 3.52	$1.30^{+0.33}_{-0.34}$	$3.63^{+0.70}_{-0.64}$	$5.47^{+1.31}_{-1.11}$
A 697	3.86 ± 0.56	7.74 ± 1.12	11.09 ± 3.62	$1.60^{+0.38}_{-0.38}$	$5.87^{+0.89}_{-0.82}$	$9.73^{+1.86}_{-1.61}$
A 1835	5.53 ± 0.82	9.15 ± 2.53	16.39 ± 10.02	$2.03^{+0.40}_{-0.41}$	$6.78^{+1.20}_{-1.07}$	$10.86^{+2.53}_{-2.08}$
ZwCl 1454	2.90 ± 0.82	3.12 ± 1.17	5.42 ± 4.04	$0.63^{+0.27}_{-0.29}$	$1.83^{+0.69}_{-0.57}$	$2.80^{+1.39}_{-1.03}$
ZwCl 1459	3.24 ± 0.66	3.92 ± 1.08	3.25 ± 2.83	$1.26^{+0.30}_{-0.30}$	$2.74^{+0.71}_{-0.63}$	$3.77^{+1.17}_{-0.98}$
RX J1720	2.17 ± 0.64	3.13 ± 1.05	6.31 ± 3.11	$1.36^{+0.28}_{-0.26}$	$2.64^{+0.78}_{-0.66}$	$3.48^{+1.28}_{-0.99}$
A 2219	4.54 ± 0.71	7.68 ± 1.62	12.45 ± 4.92	$2.65^{+0.41}_{-0.44}$	$5.67^{+1.05}_{-0.95}$	$7.75^{+1.89}_{-1.60}$
A 2261	4.32 ± 0.61	7.94 ± 1.44	10.64 ± 4.75	$2.49^{+0.31}_{-0.31}$	$5.70^{+0.86}_{-0.78}$	$7.97^{+1.51}_{-1.31}$
RX J2129	2.53 ± 0.57	4.78 ± 1.02	8.17 ± 3.36	$0.97^{+0.37}_{-0.38}$	$3.28^{+0.77}_{-0.69}$	$5.29^{+1.76}_{-1.38}$
A 2390	4.69 ± 0.68	8.84 ± 1.31	18.32 ± 3.74	$2.21^{+0.31}_{-0.30}$	$4.97^{+0.90}_{-0.82}$	$6.92^{+1.50}_{-1.29}$
A 2485	2.84 ± 0.72	3.36 ± 1.11	8.04 ± 3.97	$0.71^{+0.30}_{-0.30}$	$2.30^{+0.63}_{-0.56}$	$3.63^{+1.26}_{-1.02}$
A 2631	3.13 ± 0.49	3.97 ± 0.87	8.16 ± 2.49	$1.70^{+0.25}_{-0.26}$	$3.40^{+0.53}_{-0.49}$	$4.54^{+0.89}_{-0.78}$

* Column (1): cluster name; Column (2): the aperture mass within the projected radius of $500\,h^{-1}$kpc at the cluster redshift, in units of $10^{14}\,h^{-1}\,M_{\odot}$; Columns (3,4): the aperture masses within the radius corresponding to the over-density $\Delta = 500$ and the virial radius, respectively, where the radii are computed from the best-fit NFW model to the tangential distortion profile; Columns (5–7): the three-dimensional masses estimated from the NFW model fitting, M_{2500}, M_{500}, and M_{200}, for the over-densities $\Delta = 2500$, 500, and 200, respectively.

These results are naturally expected as follows. Recalling that the two-dimensional projected mass includes all of the mass contributions contained in the cylinder from the observer to the source galaxies along the line-of-sight, the aperture mass has an additional mass contributions to the three-dimensional spherical mass within the same radius. The main contribution arises from integration of the cluster mass distribution, itself, along the line of sight to calculate the mass within a cylinder of the same radius on the sky as the sphere used in the calculation of the 3D NFW mass. The aperture masses are therefore always expected to be larger than the 3D NFW masses. For example, the amplitude of the mass biases calculated above is well explained by a cluster-scale NFW profile. As described explicitly in appendix 2, the ratio of the projected 2D and 3D masses of such an NFW halo are calculated analytically to be: $M_{2D}^{NFW}(<\theta_m)/M_{3D}^{NFW}(<r=D_l\theta_m)\simeq 1.29$ and 1.43 for $\Delta=\Delta_{vir}$ and 500, respectively, assuming the concentration parameter $\langle c_{vir}\rangle = 3.6$, the mean concentration for all the clusters. These biases are shown by the solid lines in figure 9, showing nice agreement with the measured biases. In other words the three-dimensional spherical mass can be estimated from the aperture mass by correcting for the mass bias, assuming an NFW profile (see Mahdavi et al. 2008 for such an example). Note that the correction factor is not so sensitive to the assumed concentration parameter, because the aperture mass does not measure shear signals at inner radii, which are sensitive to the halo concentration. Even if $c_{vir}=8$ is assumed, the correction factor becomes smaller only by about 10%.

5.7. *Discussion of Systematic Errors*

There are several sources of systematic errors involved in the weak lensing measurements. In this subsection we discuss possible effects of the systematic errors on our results.

5.7.1. *Dilution contamination*

One of the most important systematic errors to which we have paid particular attention is dilution of the weak lensing signal due to contamination of the background galaxy catalog by faint cluster galaxies.

As described in section 3, we defined several samples of background galaxies according to different color/magnitude selection criteria: the magnitude-selected faint galaxy sample

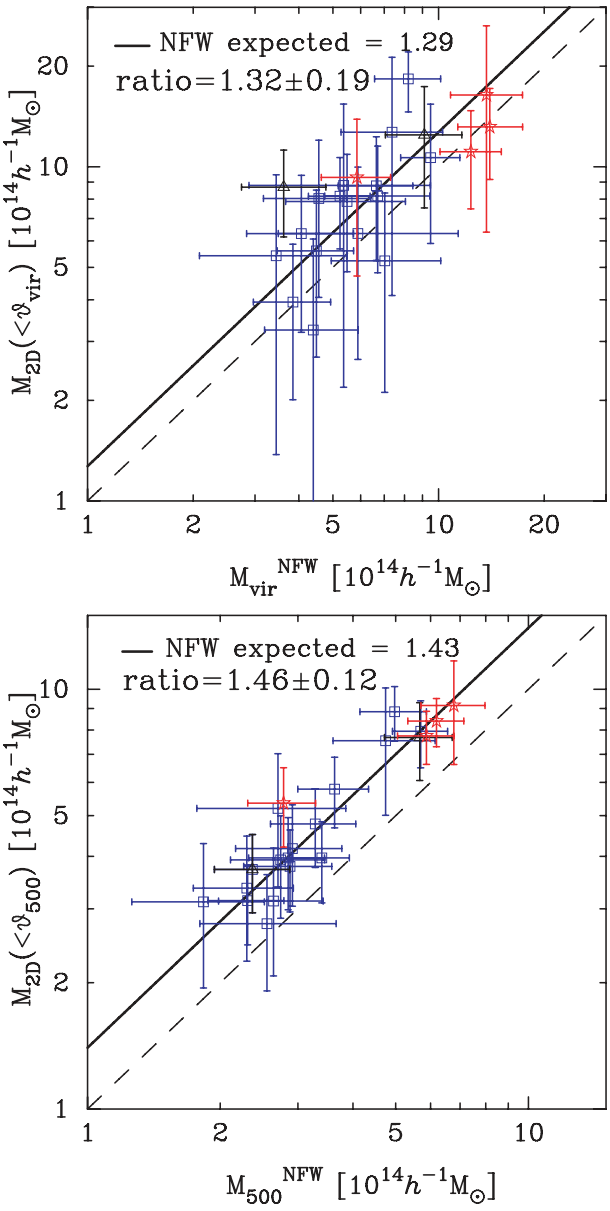

Fig. 9. Comparing the lensing aperture mass with the three-dimensional mass that is obtained from the NFW model fitting, for each of 22 clusters, as in figure 4. The upper panel shows the results obtained when the virial radius of the best-fit NFW model is assumed for the aperture radius, while the lower panel shows the results for the radius of the over-density, $\Delta = 500$. The 2D aperture masses are systematically greater than the 3D masses for both cases. In each panel the numbers labeled as "ratio" are the ratio of the 3D and 2D masses and the dispersion over all of the clusters. For a comparison, the solid line denotes the mass difference expected from a cluster-scale NFW profile with concentration parameters $\langle c_{vir}\rangle = 3.6$ and $\langle c_{500}\rangle = 1.7$, computed using equation (A3): $M_{2D}^{NFW}/M_{3D}^{NFW} \simeq 1.29$ and 1.43 for the radii with $\Delta = \Delta_{vir}$ and 500, respectively, which are in good agreement with the actual measurements. Note that the dashed line denotes $M_{2D} = M_{3D}$. The different symbols are as in figure 4.

that is often used in the literature and a more secure "red + blue" galaxy sample, defined as faint galaxies redder and bluer than the cluster red-sequence by a minimum color offset. Figure 10 demonstrates the impact of dilution on estimates of the cluster parameters, comparing the best-fit NFW parameters obtained when using the faint and red + blue galaxy samples. It is clear that the concentration parameter for the faint galaxy sample is systematically smaller than for the red + blue sample for most of the clusters, i.e., underestimated due to the dilution effect inherent in the faint sample. The bias is measured to be $c_{vir}^{(red+blue)}/c_{vir}^{(faint)} \simeq 1.60 \pm 0.22$. On the other hand, the virial mass constraints are consistent between the two samples within the error bars: $M_{vir}^{(red+blue)}/M_{vir}^{(faint)} \simeq 1.14 \pm 0.11$. This is because the virial mass is mainly sensitive to the overall shear amplitudes at large radii ($\gtrsim 10'$), and relatively insensitive to the distortion signals at small radii to which the concentration parameter is particularly sensitive. It is important to remember here that the dilution effect increases as the cluster-centric distance decreases because the number density of faint cluster galaxies that contaminate the faint galaxy catalog is expected to roughly follow the underlying density profile of the cluster. Thus, our results indicate that correcting for the dilution effect is important to obtain unbiased, accurate constraints on the cluster parameters, especially on the concentration parameter.

It is nevertheless worth noting that, due to limited information on the galaxy colors and redshifts, the red + blue galaxy sample we have used may still be contaminated by member and foreground galaxies. According to the results in figure 10, we should also bear in mind that the virial mass estimates are relatively unbiased, but the best-fit concentration parameters given in table 6 may still underestimate the true value (if an NFW profile represents the true mass distribution).

However, unsurprisingly, given the expected variation of dilution as a function of the radius, the amplitude of the bias in mass measurements depends on the chosen aperture radius within which the mass is measured. Figure 11 shows the variation of the ratio of mass estimates from the faint and red + blue galaxy samples changes as a function of the over-density used to define the cluster mass. As Δ increases, the cluster masses become progressively underestimated due to more significant dilution of the weak lensing signal by cluster members. This is an important result when considering studies in which lensing-based mass estimates are compared with cluster observables at other wavelengths that are conventionally measured at over-densities exceeding Δ_{vir}. For example, X-ray observations, especially with Chandra, are typically sensitive out to $\Delta = 2500$. Figure 11 shows that, in this case, weak lensing may underestimate M_{2500} by a factor of 2 if the faint galaxy sample, based solely on the magnitude selection, is employed. Therefore, the dilution effect should be carefully corrected for if weak lensing is used to estimate cluster masses with higher over-densities.

5.7.2. Source redshift uncertainty

As described in subsection 3.2, we estimated the redshifts of source galaxies using the well-calibrated COSMOS photo-z catalog. However, our analysis includes faint galaxies sometimes down to $i = 26$, while the COSMOS galaxies are available only down to $i = 25$. Hence, our lensing results may be affected by a residual uncertainty in the source redshift, although such faint galaxies are generally assigned a smaller weight.

A 5% or 10% change in the average distance ratio, which controls the overall amplitude of the distortion signal,

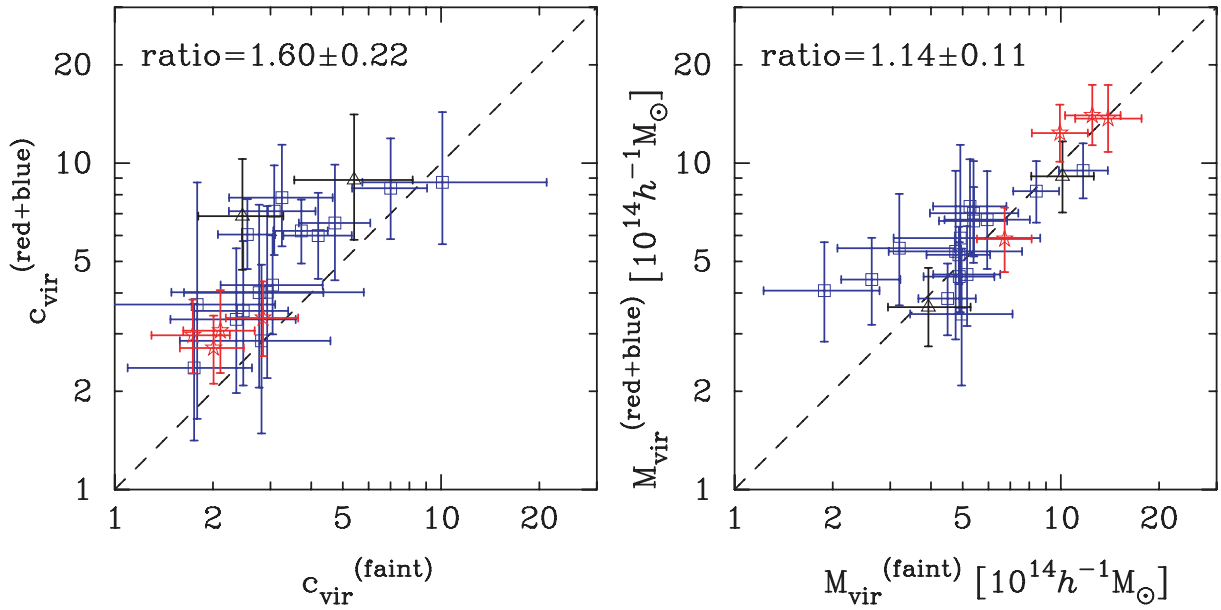

Fig. 10. Comparison of the best-fit parameters of NFW model obtained using the "faint" galaxy sample and the "red + blue" galaxy sample in the weak lensing analysis for the 22 clusters as in figure 4, where the faint galaxy sample is likely to be more contaminated by unlensed member galaxies and therefore suffer from the dilution effect (see section 3). The left panel shows the results for the concentration parameter, and the right panel for the virial mass. The concentration parameter is systematically underestimated by the dilution effect, while the virial mass is little affected. This is because the dilution effect is indeed caused mainly by member galaxies, which reduces the measured distortion signals on small radii, but preserves the signals at large radii to which the virial mass is sensitive.

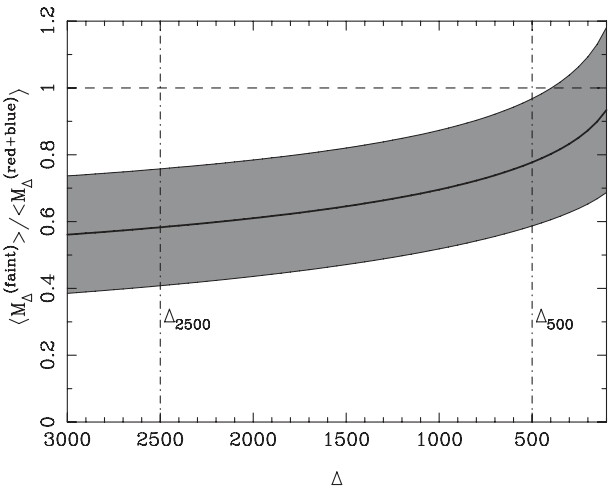

Fig. 11. Solid curve shows the ratio of NFW mass estimates for the red + blue galaxy sample and for the faint galaxy sample, as a function of the over-density used to define the cluster mass. The shaded, gray region around the solid curve is the dispersion of 19 clusters. The dilution effect causes cluster masses to be more significantly underestimated with increasing the over-density.

corresponds to $\simeq 10\%$ or 20% in the mean source redshift for a cluster at $z \simeq 0.2$ or 0.3, respectively. A typical uncertainty in the mean source redshift, inferred from the photo-z errors in the COSMOS catalog, is a few percent at most; therefore, a 10% level change in the mean redshift is unlikely. Recall that a bias in the average distance ratio is linearly propagated into a bias in the cluster mass estimates (a 10% change in $\langle D_{\rm ls}/D_{\rm s}\rangle$ yields a 10% change in the best-fit mass parameter). On the other hand, the concentration parameter is less affected by the bias in the distance ratio about by a factor of 2, because the concentration is constrained by the shape of the distortion profile. Therefore, we believe that a residual uncertainty in the source redshifts is insignificant for our results.

5.7.3. Misalignment of the BCG position and halo center

Our analysis has so far adopted the angular position of the BCG as the cluster center around which to measure the tangential distortion profile. However, the BCG might be offset from the true center of the dark matter halo hosting the cluster. Such a misalignment may cause a bias in measuring the tangential distortion profile and thus cluster model parameters. One advantage of our weak lensing analysis is we can measure variations in the goodness-of-fit of the NFW model fitting to the distortion profile by varying the cluster center, on an individual cluster basis; this can be contrasted to the stacked cluster-galaxy lensing where the cluster center of each cluster has to be a priori assumed before stacking (Johnston et al. 2007). In our case, if the BCG position is close to the true center, the χ^2 value should be close to its true minimum when the BCG is taken as the cluster center in the analysis. On the other hand, if we adopt the BCG as the cluster center in a cluster in which the BCG is significantly offset from the true center, then the resulting χ^2 value may become significantly degraded.

In figure 12 we examine the impact of the uncertainty in the assumed cluster center on the NFW model parameters. For each of the 22 clusters shown in figure 4, the open diamond symbols show typical variations in the best-fit parameters when taking a random point as the cluster center that is away from the BCG position by within $10''$ in radius. More precisely, the results are computed from the variance of the best-fit parameters obtained from 100 Monte Carlo realizations of random

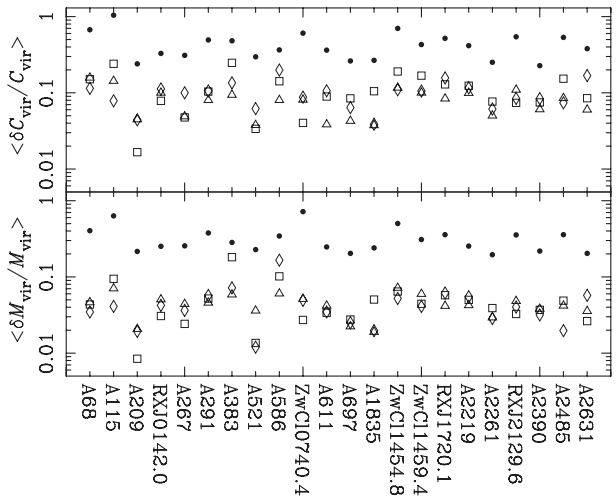

Fig. 12. The diamond symbols show typical biases in the best-fit parameters, $c_{\rm vir}$ (upper panel) and $M_{\rm vir}$ (lower), when the cluster center is randomly taken from an arbitrary point in the vicinity of BCG within $10''$ in radius. Note that the y-axis is plotted on a logarithmic scale. The squares show typical biases in the best-fit parameters obtained when shifting the innermost radial bin by $\Delta\theta_{\rm min} = \pm 0'.2$ in the tangential distortion profile, while the triangles show the biases in the parameters when changing the number of radial bins in the range of $N_{\rm rad} = [7,16]$, instead of their fiducial choices. For comparison, the filled symbols show the statistical accuracies of these parameter estimations given in table 6.

cluster center identifications. The range of $10''$ radius is based on the fact that the χ^2 value for the best-fit model significantly degrades for most of our clusters if the cluster center is taken to be offset from the BCG position by more than $10''$, and is also consistent with the distribution of offsets between the BCG centers and the X-ray centroids (Sanderson et al. 2009). Comparing the results with the filled symbols, one finds that possible variations in the true cluster center around the BCG position cause negligible biases in the parameters, typically smaller by almost one order of magnitude than the statistical errors on our fiducial analysis (i.e., the BCG is taken as the cluster center). Physically, the cluster parameters that we are interested in are sensitive to weak lensing distortions at larger radii compared to the size of the cluster center variations. Therefore, the relative inaccuracy in the cluster center position is negligible. These results are also consistent with numerous strong lensing studies (e.g., Kneib et al. 1996; Smith et al. 2001, 2002, 2005; Sharon et al. 2005; Richard et al. 2007) in which negligible BCG-cluster center offsets were found. We are also testing this more thoroughly with our new HST data (SNAP:10881; Hamilton-Morris et al. in preparation, and GO:11312; Richard et al. 2010) and the new Bayesian version of lenstool (Jullo & Kneib 2009).

5.7.4. Radial binning

Our fiducial analysis did not use the distortion signals at very small radii to avoid the effect of noisy measurements in bins that subtend small solid angles on the sky, in addition to seeking to minimize the impact of any mis-identification of the cluster center on the model fitting (see the tangential distortion plots for each cluster field in appendix 3 to find the range of angular scales used). The square symbols in figure 12 show the mean variation in the NFW parameters obtained when shifting the innermost radial bin used in the analysis by $\Delta\theta_{\rm min} = \pm 0'.2$ with the cluster center being fixed to the BCG position. This uncertainty has a similar-level impact on the model parameters to the diamonds, and is again considered to be an insignificant effect compared to the current statistical precision.

Finally, we also study the effect of the radial binning scheme on the model fitting. We typically use 13 bins in the tangential distortion profiles; finer or coarser binning may change the results, because the intrinsic ellipticity noise contribution to the measurement errors is sensitive to the radial binning that determines the number of background galaxies contained in each radial annulus. The triangles show typical variations in the parameters when varying the bin number in the range $N_{\rm rad} = [7,16]$, confirming that the best-fit parameters do not change significantly. This is partly because the effect of substructures on the azimuthally averaged tangential profile do not largely change with the radial bin variations. The possible biases are again small compared to the statistical errors.

5.7.5. Projection effect

A chance projection of foreground/background mass structures can potentially affect the cluster parameter determination based on the "non-local" distortion profile, which is sensitive to the total interior mass in projection. It can locally boost the surface mass density, and hence can affect the tangential distortion measurement if this physically unassociated mass structure is contained within the measurement radius. For determining the NFW concentration parameter, it can lead to either an under- or over-estimation of the concentration, depending on the apparent position of the projected mass structure. One way to overcome this is to utilize the convergence profile in order to examine the cluster mass profile, by locally masking out the contribution of the known foreground/background structure in the reconstructed mass map (appendix 3; also see Umetsu et al. 2009 for the case of A 2261). It should be again worth noting that these projection effects are averaged out in the stacked lensing signals. Since our results for the individual clusters are consistent with the stacked lensing results (see figure 6), the projection effect does not seem to cause significant biases in our results. The projection effect is studied in more detail in our subsequent paper, confirming an insignificant projection effect for the current measurements (Oguri et al. 2010).

5.7.6. Shape measurement

The shape measurement method may involve systematic errors. As studied in detail by the STEP project (Massey et al. 2007; Heymans et al. 2006), the various shape measurement methods developed to date differ in galaxy ellipticity measurements by up to a multiplicative bias of $\sim 10\%$. It is important to note that STEP was conceived to inform analysis strategies for cosmic shear experiments, and thus concentrated on weak lensing signals of $\lesssim 5\%$ in contrast to cluster signals that typically reach $\gtrsim 10\%$. STEP also used exclusively synthetic data. Nevertheless, possible method-dependent systematic biases in the galaxy shape measurement are also relevant for cluster lensing studies. We therefore repeated the galaxy shape measurement steps of our analysis for a representative subset of our sample using the im2shape method (Bridle et al. 2002), as implemented by G. P. Smith et al. (in preparation). The resulting distortion profiles were identical within

the measurement errors to those based on the KSB methods described earlier in this paper. In summary, whilst further careful tests are required to validate the shape measurement methods on both synthetic and real cluster lensing data, we found no evidence for shape measurement systematic biases in our analysis, and do not expect them to be a dominant source of errors.

5.8. *Characteristics of Mass Maps vs. X-Ray and Radio Information*

Two-dimensional maps of projected mass density can be reconstructed from the measured ellipticity distribution of background galaxy shapes (e.g., Kaiser & Squires 1993). The mass maps of individual clusters are shown in appendix 3. Since the shear and mass density fields are equivalent in the weak lensing regime, the mass maps do not carry any additional information on cluster parameters. Also, in practice uncertainties in reconstructed mass maps are highly correlated between different pixels — it is therefore important to include the error covariance in order to properly propagate the measurement uncertainties into accuracies of parameter estimations from mass maps (see for such studies Umetsu & Broadhurst 2008). Nevertheless, mass maps are useful when comparing the total matter distribution with cluster properties obtained from other wavelengths (optical, X-ray, etc.), in order to study the evolutionary processes and dynamical stages of each cluster (e.g., Clowe et al. 2006; Okabe & Umetsu 2008). Here, we comment on the features in the mass maps from a multi-wavelength perspective.

Our cluster samples contain 2 *cold-front* clusters that have sharp discontinuities of X-ray cores observed in the X-ray surface brightness: ZwCl 1454 (also known as MS 1455.0+2232: Mazzotta et al. 2001a) and RX J1720 (Mazzotta et al. 2001b). The formation of cold fronts is one of the outstanding problems in cluster physics. In fact, the mass maps of these two clusters suggest a bi-modal mass distribution in the core of each cluster. In both clusters, one sub-clump of the bi-modal mass distribution appears to be the "counterpart" of hot intra-cluster gas at a similar position, while the other does not have any clear counterpart (see N. Okabe et al. in preparation for a more quantitative study). This bi-modal structure is consistent with results on the other three cold-front clusters studied to date, including the bullet cluster, A 2034 and A 2142 (Clowe et al. 2006; Okabe & Umetsu 2008).

The origin of diffuse radio emission within clusters, emanating from synchrotron radiation of relativistic non-thermal electrons, remains an unsolved mystery. One possible scenario discussed in the literature is that the non-thermal electrons are produced by hierarchical mergers that every cluster universally experiences in the CDM scenario. Weak lensing mass maps are useful tools with which to test this picture because they allow one to search for direct merging signatures, e.g., prominent substructures in the mass maps due to cluster–cluster mergers. An important advantage of this approach is that the collisionless nature of dark matter should result in the merger signatures surviving longer in the dark matter distribution that dominates weak lensing maps compared to the intra-cluster hot gas (e.g., see Okabe & Umetsu 2008 for the observational; and Tormen et al. 2004 theoretical studies). On the other hand, X-ray substructures may not be a good tracer of mass substructures; indeed, sometimes they are not associated with the lensing substructures, depending on the stage that the merger has reached (Okabe & Umetsu 2008; see also Smith et al. 2005 for a strong-lensing/X-ray comparison).

Our cluster sample contains 8 clusters in which diffuse radio emissions have been found to date: A 209 (Giovannini et al. 2006), A 697 (Kempner & Sarazin 2001), RX J1720 (Mazzotta & Giacintucci 2008), ZwCl 1454 (Venturi et al. 2008), A 115 (Giovannini et al. 1999), A 2345 (Giovannini et al. 1999), A 521 (Ferrari et al. 2003), and A 2219 (Kempner & Sarazin 2001). These clusters appear to show the substructures that are seen to be more prominent than those in other clusters, and the substructure locations generally match well the morphology of the radio emission. This trend was also reported for other clusters with diffuse radio sources (Clowe et al. 2006; Okabe & Umetsu 2008). A more quantitative comparison between the mass map and the radio sources, further including the X-ray information, will be presented elsewhere (N. Okabe et al. in preparation).

6. Summary and Discussion

In this paper we have presented a systematic weak lensing study of 30 X-ray luminous clusters at $0.15 < z < 0.3$ as part of the Local Cluster Substructure Survey (LoCuSS), based on high-quality Subaru/Suprime-Cam data. Our findings are summarized as follows:

- The high-quality Subaru data allowed a significant detection of individual cluster lensing signals (table 3). The total signal-to-noise (S/N) ratios for the tangential distortion profile, integrated over the range of radii probed, are $5 \lesssim S/N \lesssim 13$ for all 30 clusters.
- We made a detailed comparison of the measured distortion profile with mass profile models (table 6 and figure 4) — among the secured 22 clusters (with color information and suitable for the spherical model fitting), 3 clusters favor an NFW profile compared to an SIS model, 2 clusters cannot be well fitted by either model, and the other clusters are well-fitted by either model.
- The virial mass estimates from NFW and SIS models are in good agreement, albeit with large measurement errors. However, the best-fit mass tends to be underestimated if an SIS model is employed. We understand this, in the context of the stacked analysis discussed below, to be caused by the SIS model under-predicting the amplitude of the gravitational distortion on large scales due to its inability to describe the curvature of the distortion profile of an NFW halo.
- We detect an anti-correlation between the mass and the concentration at 2σ significance: $c_{\rm vir}(M_{\rm vir}) = 8.75^{+4.13}_{-2.89} \times (M_{\rm vir}/10^{14}h^{-1}\,M_\odot)^{-\alpha}$ with $\alpha \approx 0.40 \pm 0.19$. This is in qualitative agreement with predictions from numerical simulations, but with a tentative detection of a steeper slope than predicted (figure 6).
- The distribution of $c_{\rm vir}$ for our morphologically- and strong-lensing-unbiased sample does not contain any clusters with extremely high concentrations, as have

been reported in the literature for spectacular strong lensing clusters. More precisely, our best-fit $c_{\rm vir}$–$M_{\rm vir}$ scaling predicts $c_{\rm vir} \simeq 3.48^{+1.65}_{-1.15}$ for massive clusters with $M_{\rm vir} = 10^{15}\,h^{-1}\,M_\odot$. Therefore, the high concentrations of $c_{\rm vir} \sim 10$ inferred from strong lensing-selected clusters are inconsistent with our statistical analysis of X-ray selected clusters at $4\,\sigma$ significance.

- The stacked distortion signals, for the two sub-samples of 19 clusters binned into mass bins, show a pronounced radial curvature over radii ranging from $70\,h^{-1}$ kpc to $3\,h^{-1}$ Mpc (figure 8). The profiles are well-fitted by a curved (cored isothermal or NFW) density profile, supporting the individual cluster lensing results, and strongly rule out the SIS model at $6\,\sigma$ and $11\,\sigma$ for low ($M_{\rm vir} < 6 \times 10^{14}\,h^{-1}\,M_\odot$) and high ($M_{\rm vir} > 6 \times 10^{14}\,h^{-1}\,M_\odot$) mass bins, respectively.
- The projected 2D mass within the cylinder enclosed within a given projected radius, estimated from the model-independent aperture mass method, tends to be greater than the 3D spherical masses enclosed within the same radius in 3D, obtained from the NFW model fitting (table 8 and figure 9). The ratio of 2D to 3D masses is $\simeq 1.32$ and ~ 1.46 at $\Delta = 500$ and $\Delta = \Delta_{\rm vir}$, respectively, which can be well explained by the projected mass contribution of a cluster-scale NFW halo with $c_{\rm vir} \simeq 4$.

Our results are an important step towards a more thorough empirical understanding of the mass distribution in galaxy clusters, and thus towards testing the nature of dark matter and dark energy (through the cluster mass function for the latter). However, the results are limited by (i) the modest statistical precision available from a sample of ~ 20 clusters, (ii) the limited color information available on the background galaxy samples, (iii) the simplistic spherical mass modeling approach applied to the data, and (iv) we have ignored other data available to constrain the cluster mass distributions, most notably strong lensing arcs in the cluster cores.

For example, the detection of a slope in the observed $c_{\rm vir}(M_{\rm vir})$ relation is significant at just $2\,\sigma$. Simply doubling or quadrupling the sample size would improve this to a 3 or $4\,\sigma$ result, respectively. Measurements of the concentration parameters appear to be more sensitive to systematic errors than measurements of cluster mass. We therefore plan to combine the Subaru weak lensing constraints with strong lensing constraints available from our HST and Keck data (Richard et al. 2009) to build joint strong/weak lensing models of the clusters, from which to obtain more robust concentration measurements (G. P. Smith et al. in preparation). An important feature of these models will be the use of pseudo-elliptical NFW models (Golse & Kneib 2002) and the inclusion of multiple halos in the models to capture the full two-dimensional structure of the clusters in the plane of the sky. Jing and Suto (2002) have also used numerical simulations to show that CDM halos are better fitted by a triaxial mass distribution than a spherical NFW model, even in the statistical average sense, as naturally expected from the collision-less nature of CDM particles. This is a very interesting possibility that has been explored recently by Oguri et al. (2005) and Corless and King (2008), and can be explored in a straightforward manner using the same data sets as used in this paper (Oguri et al. 2010).

It is also interesting to compare our results on the distribution of cluster concentrations with the high-concentration results obtained for several well-known strong lensing clusters, notably A 1689, Cl 0024, and MS 2137 (Gavazzi et al. 2003; Kneib et al. 2003; Broadhurst et al. 2005; Limousin et al. 2007; Broadhurst et al. 2008; Oguri et al. 2009). The important difference, beyond sample size, between these detailed single-object studies and our statistical study is that our cluster sample is unbiased with respect to the prevalence of strong lensing arcs in the cluster cores (figure 1). As shown in figure 6, the massive clusters in our sample generally have the lowest statistical errors, and indeed have low concentrations, $c_{\rm vir} \sim 3$; i.e., consistent with the simulation results. On the other hand, there are clusters displaying relatively high concentrations of $c_{\rm vir} \sim 8$. An important test of the joint interpretation of our statistical results with those of single-object studies will be whether the presence of strong lensing arcs in clusters is correlated with the high concentration of the cluster. Increased sample size and joint strong/weak lens modeling will both be central to this investigation.

Vikhlinin et al. (2009b) recently claimed very tight cosmological constraints based on the cluster mass functions at $\Delta = 500$ derived from Chandra observations under the assumption of hydrostatic equilibrium. The relationship between X-ray observables and mass was calibrated using numerical simulations (Kravtsov et al. 2006; Nagai et al. 2007; Vikhlinin et al. 2009a), and the level of residual uncertainty in the absolute mass calibration was assessed by comparing the X-ray derived masses with the lensing mass estimates of Hoekstra (2007), claiming possible 5%-level residual uncertainties in the mass estimate. However, our results indicate that the lensing masses estimated at $\Delta = 500$ are sensitive to dilution of the weak lensing signal by faint cluster galaxies, cluster masses being underestimated by $\gtrsim 20\%$ at $\Delta = 500$ if dilution is not properly corrected for. Therefore, if the absolute mass calibration primarily rests on a comparison with the lensing masses, the X-ray derived masses may still involve additional biases. In this sense, a further large detailed comparison of the X-ray and lensing masses for joint X-ray and lensing cluster samples is crucial. In particular, a detailed *cluster-by-cluster* comparison will be very important to pin down the sources of systematic errors due to physical differences between the clusters. The mass maps shown in appendix 3 will be useful for this purpose because the mass distribution directly reflects the dynamical stages of a cluster (relaxed, merging, etc.). These studies will be presented elsewhere (N. Okabe et al. in preparation).

We are very grateful to A. Finoguenov, C. Haines, H. Hoekstra, Y. Itoh, A. Leauthaud, M. Oguri, Y. Y. Zhang, and the members of LoCuSS collaboration for invaluable discussions and comments. We also thank an annonymous referee for useful comments which led to improvements of the manuscript. Finally, we also thank Subaru Support Astronomers for the Subaru/Suprime-CAM and N. Kaiser for developing the IMCAT package publicly available. NO, MT, and GPS acknowledge warm hospitality at the Kavli Institute for Cosmological Physics at University of Chicago, where

some of this work was carried out. GPS also acknowledges warm hospitality at Tohoku University. NO, MT, and TF are in part supported by a Grant-in-Aid from the Ministry of Education, Culture, Sports, Science and Technology of Japan (NO: 20740099; MT: 20740119; TF: 20540245). MT is also in part supported by the World Premier International Research Center Initiative of MEXT of Japan. KU is partially supported by the National Science Council of Taiwan under the grant NSC97-2112-M-001-020-MY3. GPS acknowledges support from the Royal Society and the Science and Technology Facilities Council. This work is also supported by a Grant-in-Aid for the 21st Century COE Program "Exploring New Science by Bridging Particle-Matter Hierarchy" and the GCOE Program "Weaving Science Web beyond Particle-matter Hierarchy" at Tohoku University as well as by a Grant-in-Aid for Science Research in a Priority Area "Probing the Dark Energy through an Extremely Wide and Deep Survey with Subaru Telescope" (No. 18072001). This work was supported in part by the Kavli Institute for Cosmological Physics at the University of Chicago through grants NSF PHY-0114422 and NSF PHY-0551142 and an endowment from the Kavli Foundation and its founder Fred Kavli.

Appendix 1. Defining Galaxy Samples

We have concentrated on clusters for which Suprime-Cam data are available in two filters, and used the following galaxy samples to select background galaxies robustly for our weak lensing analysis: member galaxy sample, faint galaxy sample, red galaxy sample, and blue galaxy sample. In this appendix, we describe how the four galaxy samples are defined based on the color–magnitude diagram of each cluster.

A.1.1. Color–Magnitude Diagram

We typically used the color–magnitude information, e.g., the $(V-i')$–i' information, to separate cluster members from non-members. Note that because we focus on relatively low-redshift clusters, most non-member galaxies are very likely background galaxies thanks to the deep imaging data and the limited volume that lies between us and each cluster. To define the galaxy samples, we first analyze the data using SExtractor (Bertin & Arnouts 1996) in the dual-image mode, using the redder passband (typically i'-band) for source detection. We extracted all objects with isophotal areas larger than 10 contiguous pixels where each pixel ($2\farcs02$) needs to be $\geq 3\sigma$ pixel^{-1} of the local sky background. We calculate for each source the total magnitude in the AB-magnitude system using the MAG_AUTO parameter. Colors are calculated using the MAG_APER parameters with the aperture size being set to 10 pixels in diameter.

A.1.2. Member Galaxy Sample

Early-type cluster galaxies occupy a narrow well-defined locus, the so-called red sequence, in the color–magnitude diagram. Red sequence galaxies were selected as follows. First, point-sources were removed from the object catalog, and then the following relation (or its equivalent in the case that different filters were available) was fitted to galaxies brighter than 22nd magnitude in the redder filter:

$$(V-i')_{\rm E/S0} = a\,i' + b. \quad \text{(A1)}$$

The best-fit values of a and b were determined such that the number of galaxies contained in the red sequence is maximized, allowing the red sequence to have a finite width, such as $\delta(V-i') \simeq \pm 0.1$ mag, depending on the tightness of the observed color–magnitude relation. For example, the green points in figure 2 show the member galaxy sample for A 68.

In a few cases, multiple combinations of the parameters a and b were found to fit the data. In such cases we identified the sequence that is most likely the one inferred from the cluster redshift based on a passive evolution model of galaxy color and magnitude. Interestingly, as discussed in appendix 3, galaxies sitting in other red-sequences generally coincide with peaks in the weak lensing mass maps, suggesting that they correspond to over-densities at other redshifts.

We also identified the brightest cluster galaxy (hereafter BCG) in each cluster, and defined the nominal center of each cluster as the angular position of the BCG in each cluster. Note that in some clusters the BCG does not sit on the red-sequence — we therefore visually checked such clusters to ensure correct identification of the BCGs.

The BCGs and the galaxies contained in the red sequence with a finite width, which are all brighter than 22 mag (AB), provide our member galaxy sample. This member galaxy sample was used to estimate the number density field as well as the luminosity density field of cluster galaxies for comparisons with the lensing mass maps in appendix 3.

A.1.3. Faint Galaxy Sample

Magnitude-selected background galaxy samples have often been used in previous studies of cluster weak lensing. Although our main results are based on color-selected galaxies, we first define here our magnitude-selected, or "faint" galaxy samples. These samples are mainly used as a suite of reference samples against which our more sophisticated color-selection methods can be compared.

To ensure that the shape of galaxies can be measured reliably, the "background" galaxies used for weak lensing analyses are required to be both well-resolved and to have a sufficiently large integrated signal-to-noise ratio. Concerning the latter point, we restricted our attention to galaxies with signal-to-noise ratios of $\nu \geq 10\,\sigma$, as calculated with the IMCAT software. We also selected galaxies with a half-light radius, $r_{\rm h}$, in the range $\bar{r}_{\rm h}^{*} + \sigma(r_{\rm h}^{*}) < r_{\rm h} < 10$ pixels, where $\bar{r}_{\rm h}^{*}$ and $\sigma(r_{\rm h}^{*})$ are the median and rms of the half-light radii of stellar objects selected over the entire Suprime-Cam FoV. Note that the upper limit of $r_{\rm h} = 10$ pixels is chosen based on trial and error to avoid galaxies with saturated pixels and/or strange shapes, typically originating from the superpositions of two or more galaxies (e.g., Okabe & Umetsu 2008).[4] Then the faint galaxy sample is defined from the resolved, high signal-to-noise galaxies as those lying in the apparent magnitude ranges listed in table 3 — typically $22 \leq i' \leq 26$. The bright magnitude limit is designed to minimize contamination of this sample by bright cluster members, and corresponds to the apparent magnitude of $\sim i'^{\star} + 3.5$ for an early-type galaxy at the median

[4] For the clusters A 115 and A 2345, we impose more restrict conditions on the half-light radius due to poor seeing as listed in table 3.

redshift of a cluster in our sample. The faint limit is a consequence of the signal-to-noise and size cuts discussed above.

A.1.4. Background Red/Blue Galaxy Samples

Several authors have shown that faint galaxy samples, such as those described above, suffer contamination by faint cluster galaxies, and therefore weak-shear measurements based on such samples are diluted by cluster and foreground (and thus unlensed) galaxies (e.g., Broadhurst et al. 2005; Limousin et al. 2007). In this paper we employ a method described by Medezinski et al. (2007) and Umetsu and Broadhurst (2008). First, to quantify the dilution effect we calculated the mean distortion strength of each cluster by averaging the tangential distortion profile [equation (6)] over a range of radial bins:

$$\langle\langle g_+\rangle\rangle \equiv \frac{1}{N_{\rm rad}} \sum_{n;1'\le\theta_n\lesssim 20'} \langle g_+\rangle(\theta_n), \tag{A2}$$

where n runs over the radial bin labels, θ_n, in equation (6) and $N_{\rm rad}$ is the total number of radial bins used. The cluster lensing signals are greater with decreasing cluster-centric radius, and therefore this calculation assigns a greater weight to the lensing signals closer to the cluster center than those towards the edge of the FoV. This is useful when quantifying the effect of dilution, because dilution is expected to be more significant at smaller cluster-centric radii, since it roughly traces the cluster mass distribution, while the lensing distortion signals are nonlocal (non-vanishing even beyond the virial radius) and slowly decreasing with increasing radius. Note that we do not include the lensing signals at very small radii $\theta_n \le 1'$, because on these scales the signals are very noisy due to the small numbers of galaxies in these radial bins, in addition to the impact of uncertainties in the cluster center position.

As described above, SExtractor was used to build photometric catalogs, while IMCAT was used to measure galaxy shapes. Therefore, before varying the color-selection criteria, it was necessary to match the SExtractor and IMCAT catalogs. In doing so, we define the following matching criteria. For each object in the IMCAT catalog, the closest neighbor on the sky in the SExtractor catalog was identified; if positional difference between the two catalogs is less than 2 pixels (0.″404), then the two objects are regarded as the same object, and otherwise are rejected. If we found multiple candidates in this matching procedure, although very rare, we took the one with the closest total magnitude as the corresponding object.

Figure 13 shows, for A 68 as a typical example, the mean distortion strengths as a function of the varying background galaxy samples, where each galaxy sample is selected from the faint galaxy sample by further requiring that the galaxies are redder or bluer than the red-sequence (the vertical dashed line) by a given color offset in the horizontal axis.[5] Note that the data points in the different color bins are highly correlated because each data point includes all galaxies at larger color offsets than the offset at which the point is plotted.

First let us consider the results for galaxy samples redder than the red-sequence — i.e., right-ward of the vertical dashed line. The distortion strength changes as the color-cut becomes progressively redder due to both reduced cluster member contamination and to the change in the average redshift of galaxies. All other things being equal, the distortion strength should, in principle, become insensitive to color-offset when the color-cut is sufficiently large so as to render contamination, and thus dilution to be negligible. In the case of A 68,

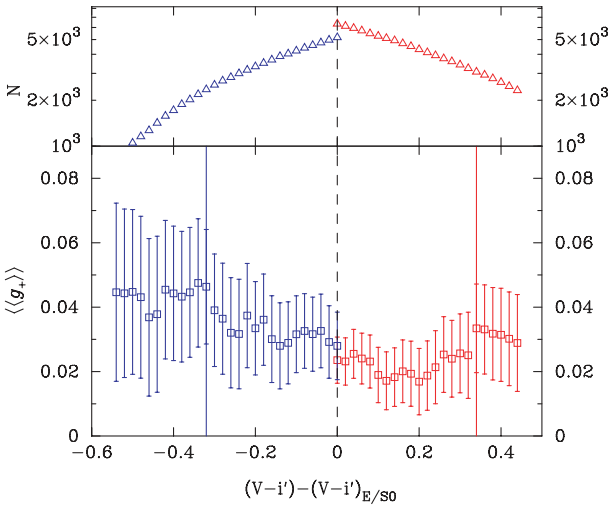

Fig. 13. Total number of galaxies (upper panel) and the mean tangential distortion strength [lower; also see equation (A2)] over the radii of $1' \le r \le 17'$, as a function of the varying background galaxy samples, for A 68. The background samples are defined with galaxies redder or bluer than the red-sequence at least by the color offsets given by x-label. The distortion strength is changed due to the dilution by cluster members, and also partly due to the change in average source redshift. The two solid lines in the lower panel denote our choices of the color cuts used to define the red/blue background galaxy samples shown in figure 2 (see text for the details).

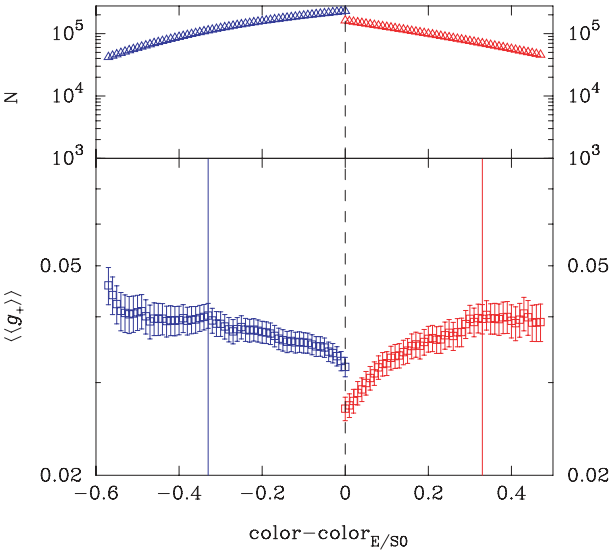

Fig. 14. As in figure 13, but stacked for 21 clusters (22 clusters with color information minus ZwCl 0740). A significant dilution of lensing signals can be found for small color offsets, i.e., if including faint galaxies with color closer to that of cluster red-sequence. The distortion strength becomes almost constant for color offsets, $|\Delta{\rm color}| \gtrsim 0.3$, at both red- and blue-sides.

[5] The errors on the mean distortion strengths are estimated as $\sigma^2_{\langle\langle g_+\rangle\rangle} = (1/N^2_{\rm rad}) \sum_n \sigma^2_{g_+}(\theta_n)$ from equation (8).

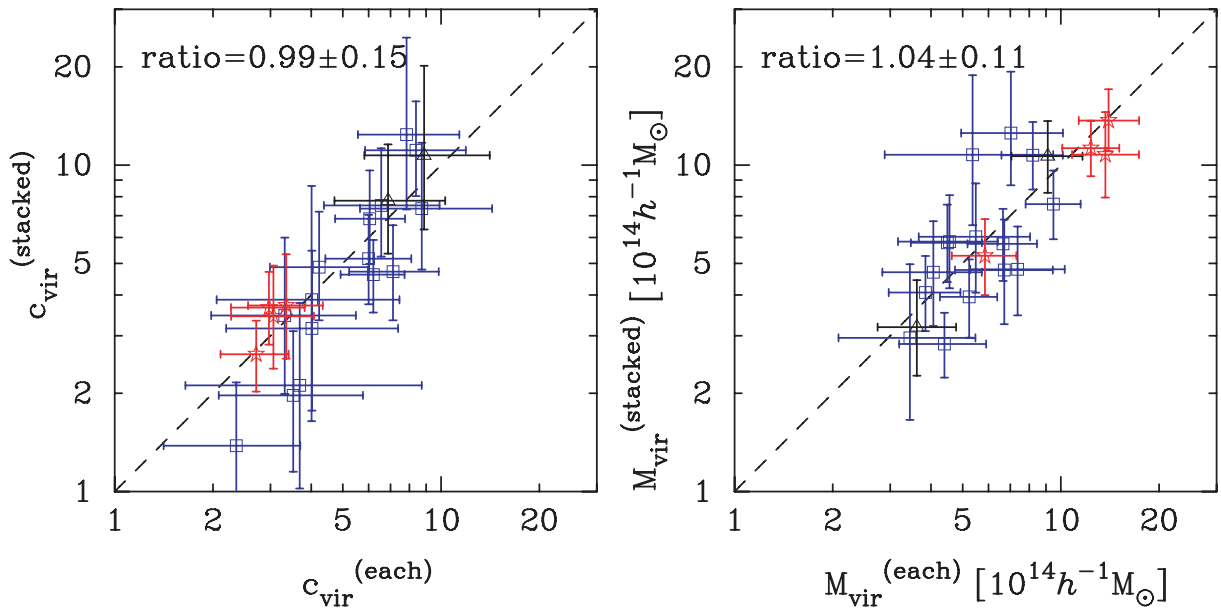

Fig. 15. Comparing the best-fit parameters, $c_{\rm vir}$ (left panel) and $M_{\rm vir}$, for each cluster field when using different samples of blue + red galaxies. The vertical axis in each panel shows the result obtained by using a background galaxy sample defined with a single color cut $|\Delta{\rm color}| = 0.3$, while the horizontal axis shows the result for our fiducial background galaxy sample. The two results agree well within the statistical errors.

we therefore adopt a color-cut of $\Delta{\rm color} \equiv (V - i') - (V - i')_{\rm E/S0} = 0.34$, as shown by the vertical (red) line. The background galaxy redshift distribution is expected to vary slowly with the color offset, suggesting that the relatively abrupt jump in the distortion strength at either side of the vertical (red) line is contamination-related.[6] Similar red-side color-cuts are adopted for the other clusters, with values lying in the range $\Delta{\rm color} \simeq [0.1, 0.35]$. Following the same logic on the blue-side we adopt a color-cut of $\Delta{\rm color} = -0.32$, and mark this with a vertical (blue) line; in this case the insensitivity of the distortion strength at the blue-side cut is more obvious than the red-side discussed above. The blue-side color-cuts are in the range of $\Delta{\rm color} \simeq [-0.4,-0.1]$ for the entire cluster sample.

We then use the combined red + blue galaxy samples in our lensing analysis throughout this paper. Despite the care that we have taken over the color-selection of background galaxies, the rather limited color information that we have used here will inevitably allow some unlensed galaxies to leak into the red + blue galaxy catalogs. Nevertheless, we are able to prove that our red + blue samples are less affected by the contamination than the faint galaxy sample. The effectiveness of our color-selection methods is demonstrated in figure 3.

Our method may be compared to an alternative method where the dilution effect is corrected for by multiplying the measured distortion signal at a given radial bin with a correction factor inferred from the increased number density of faint galaxies at the radius (e.g., see Kneib et al. 2003; Hoekstra 2007). In this method, the stacked number density profile, as shown in figure 3, is usually used to infer the correction factor, because a measurement of the number density profile is noisy for an individual cluster field — we have also found that we cannot necessarily find a clear increase in the number density of faint galaxies at small cluster-centric radii for a single cluster field.[7] Therefore, this alternative method does not allow for a cluster-by-cluster correction of dilution. Our method using a color-selected galaxy sample can thus be recognized as being a more direct, unbiased way in the sense that our method purely rests on the lensing shape measurements, and does not employ any correction factor to obtain cleaner distortion signals. We are planning to further improve the dilution correction with more accurate photometric redshifts obtained by adding more passband data, which is also invaluable to calibrate the source redshift uncertainties.

Since a selection of background galaxies is important, we also made another test as follows. Figure 14 shows the *stacked* distortion strength for 21 clusters (22 clusters with color information minus ZwCl 0740) against different background galaxy samples, as in figure 13, but selected with a single color offset for all of the clusters. With the help of stacking, the distortion strength is smoothly varying against color, and a significant dilution of lensing signals is clearly seen if including faint galaxies with color similar to the color of red-sequence galaxies. Also, evident is that the dilution strength stays constant for a color offset $|\Delta{\rm color}| > 0.3$ at both the red- and blue-sides. Note that this color offset is comparable to the color cut employed for each cluster region, as listed in table 3, giving another confirmation that our background galaxy selection is considered to be secure.

Given the results in figure 14, figure 15 shows how the best-fit parameters, $M_{\rm vir}$ and $c_{\rm vir}$, change for each cluster if

[6] However, note that, for fewer galaxies defined by the larger color-cut, additional large scatters may be caused by violation of the single source redshift assumption.

[7] This is probably because of the intrinsic clustering contamination of galaxies and of another lensing effect, magnification bias, that affects the number counts of galaxies in complex, different ways for blue and red background galaxies (e.g., Broadhurst et al. 2005).

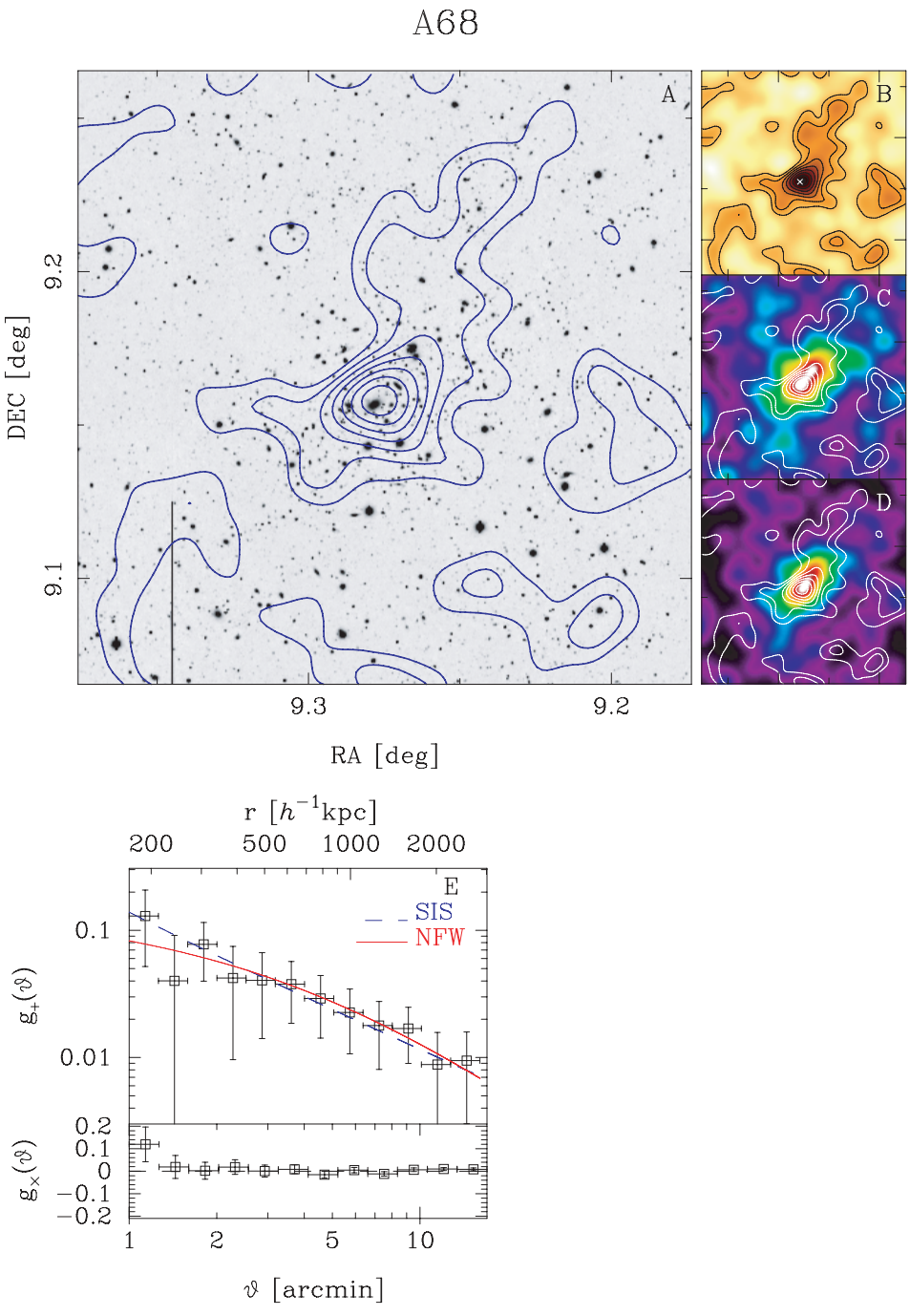

Fig. 16. Results for A 68 ($z = 0.25$). Panel A: The contours show the lensing convergence field, $\kappa(\boldsymbol{\theta})$ (the normalized mass density field), above the 1σ noise level, i.e., $\kappa(\boldsymbol{\theta}) \geq \sigma_\kappa$ [see equation (A4)]. The contours are spaced in units of $\Delta\kappa = 1\sigma_\kappa$. The region shown is $12' \times 12'$, the noise level $\sigma_\kappa = 0.033$ and the Gaussian smoothing scale FWHM $= 1'.2$ (FWHM $= 2\sqrt{\ln 2}\theta_g$). Overlaid is the Subaru redder band image (see table 1, and the i' band image for the case of A 68). Panel B: The mass map in color scales, overlaid on the same contours in the panel A. Panel C: The luminosity density map in the redder band image for the member galaxy sample (see section 3), smoothed with the same Gaussian function as in the mass map. Panel D: Similar to the panel C, but the smoothed number density map for the member galaxy sample. Panel E: The upper panel shows the radial profile of the tangential distortion component for the red+blue galaxy sample, with respect to the cluster center (BCG position). The error bars at each radial bins show the 1σ measurement error bars, which are estimated based on equation (8). The solid and dashed curves show the best-fitting NFW and SIS profiles, respectively. The lower panel shows the radial profile of the 45° rotated component of background galaxy shapes, $g_\times$, for the same background galaxy sample. The $g_\times$ component does not arise from weak lensing, and serves as a monitor of the shape measurement systematics, and our measured profile is consistent with a null signal over all the radial bins (except for the innermost bin, which is sometimes noisy due to smaller background galaxies and perhaps due to the nonlinear lensing distortion). Note that, for other clusters shown below, the panels C and D are shown if the cluster has color information. Panel E is shown if the distortion profile is compared to the mass profile models to constrain cluster parameters. See tables 1 and 6, respectively.

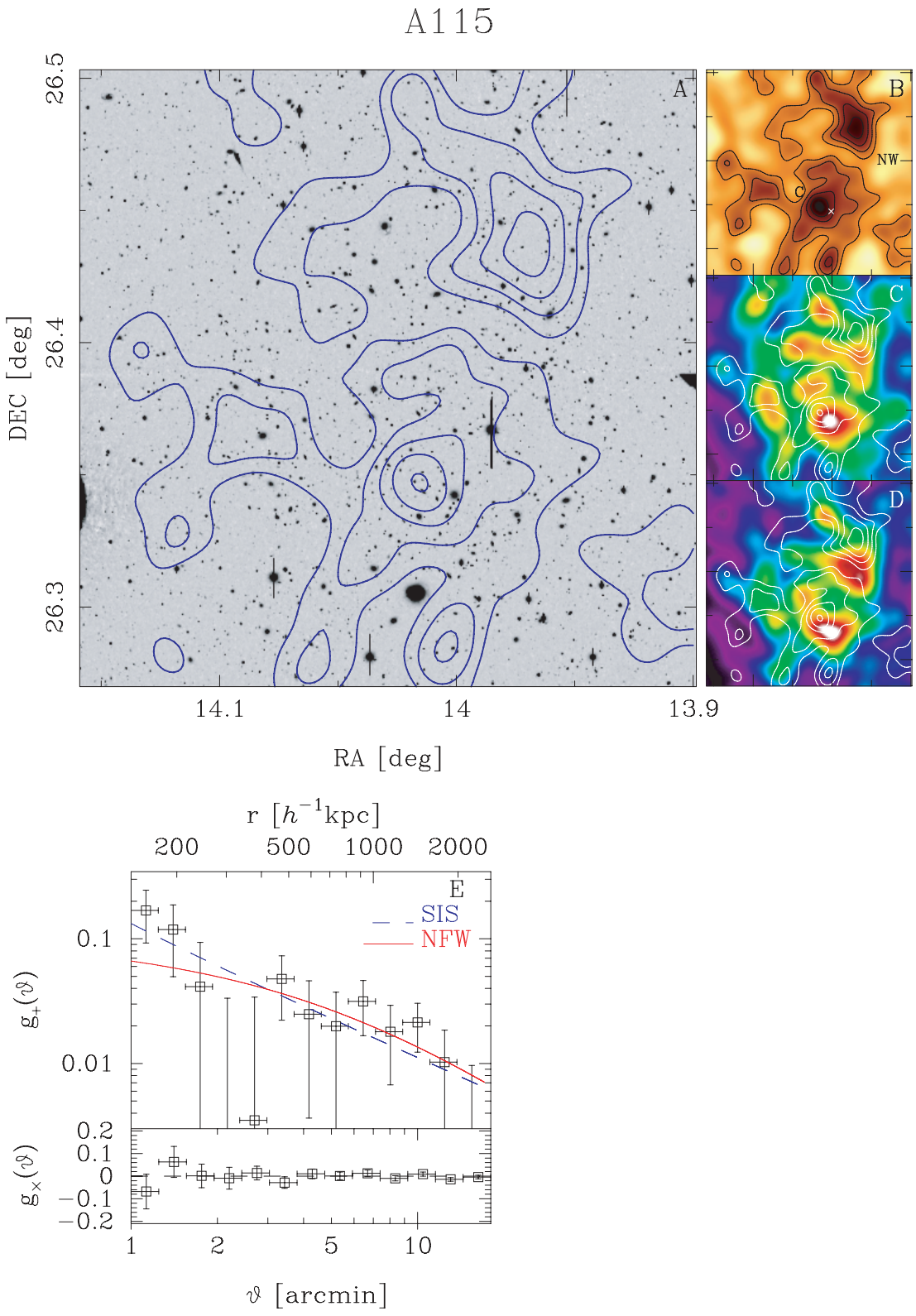

Fig. 17. Similarly to the previous figure, but for A 115 ($z = 0.20$). The region shown is $14' \times 14'$, the smoothing scale FWHM $= 1.'5$, and the noise level $\sigma_\kappa = 0.031$.

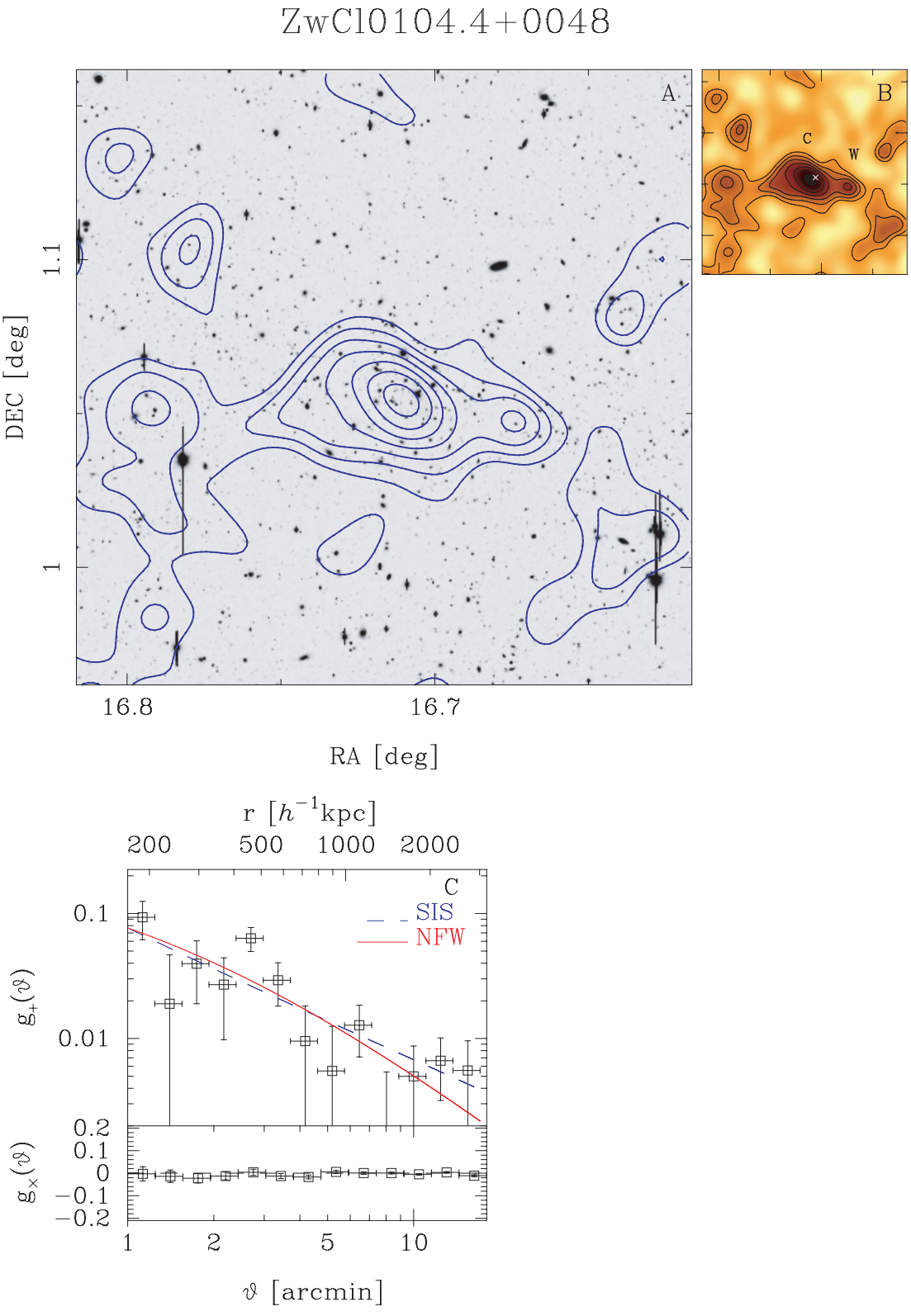

Fig. 18. Results for ZwCl 0104 ($z = 0.25$). The region shown is $12' \times 12'$, the smoothing scale FWHM $= 1.'2$, and the noise level $\sigma_\kappa = 0.025$. This cluster has only one passband data, so a comparison with the luminosity and number density distributions of a member galaxy sample cannot be made (similarly for the following clusters with no color information, which are listed in table 1).

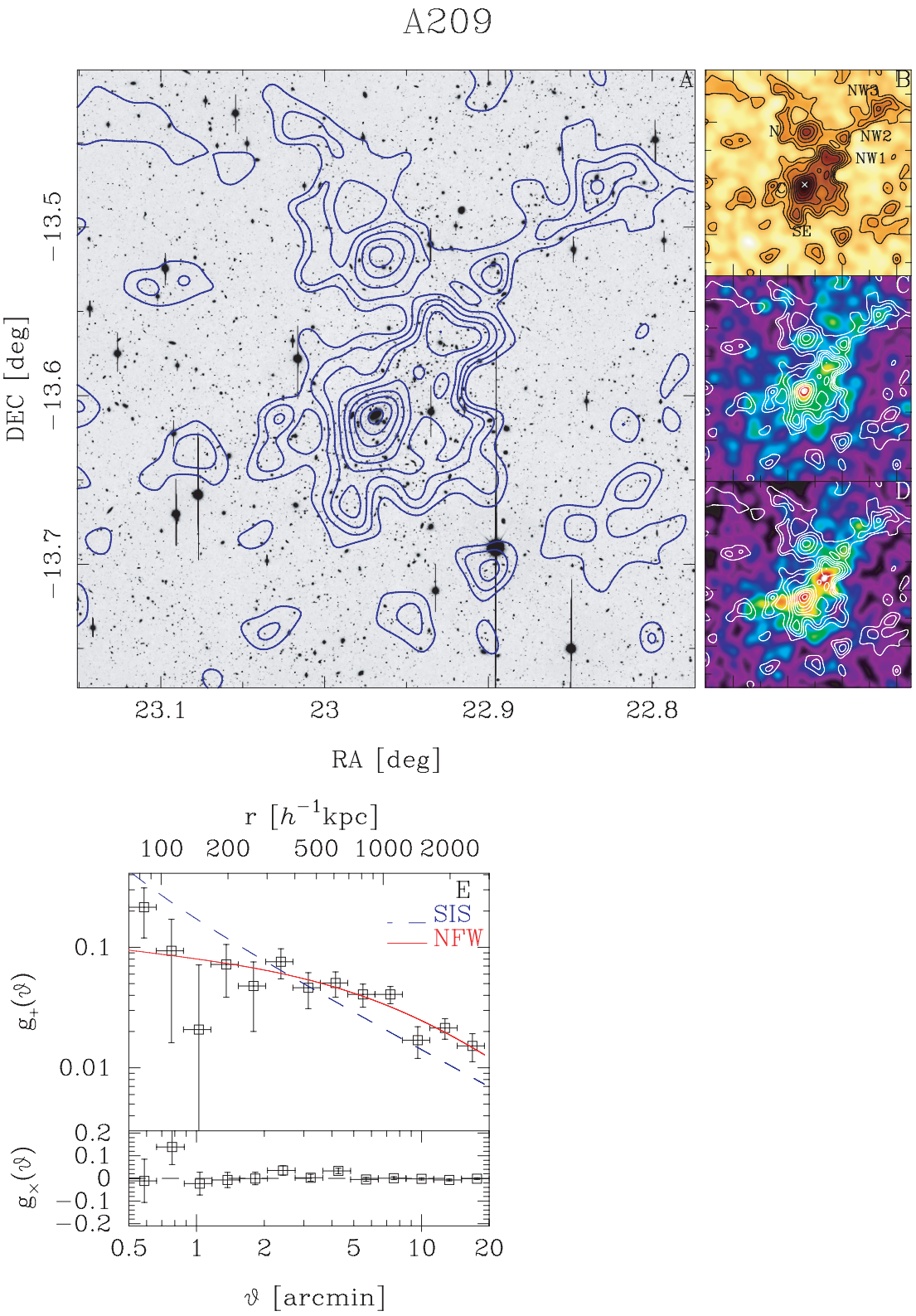

Fig. 19. Results for A 209 ($z = 0.21$). The region shown is $22' \times 22'$, the smoothing scale FWHM $= 1'.2$, and the noise level $\sigma_\kappa = 0.027$.

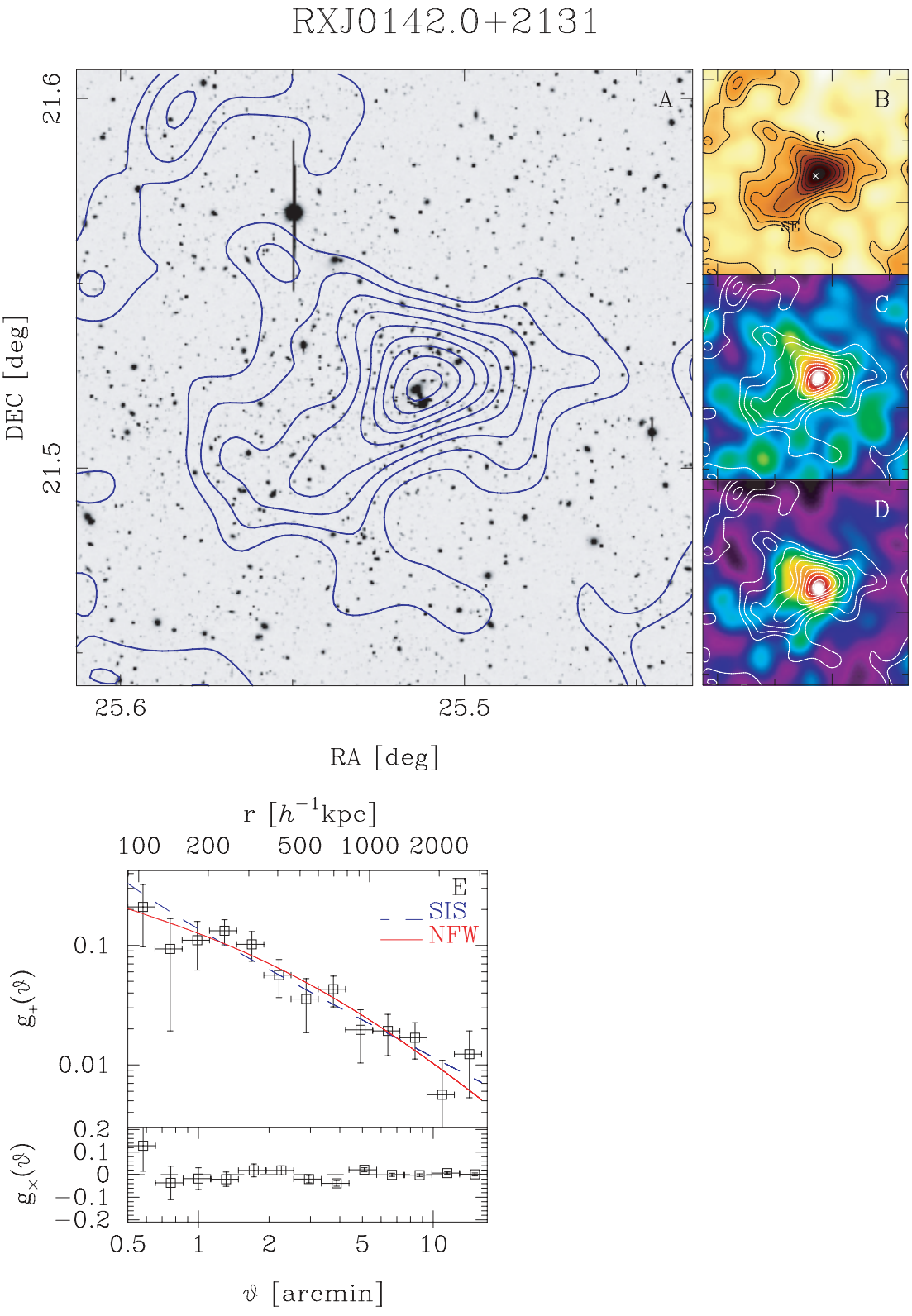

Fig. 20. Results for RX J0142 ($z = 0.28$). The region shown is $10' \times 10'$, the smoothing scale FWHM $= 1.'2$, and the noise level $\sigma_\kappa = 0.027$.

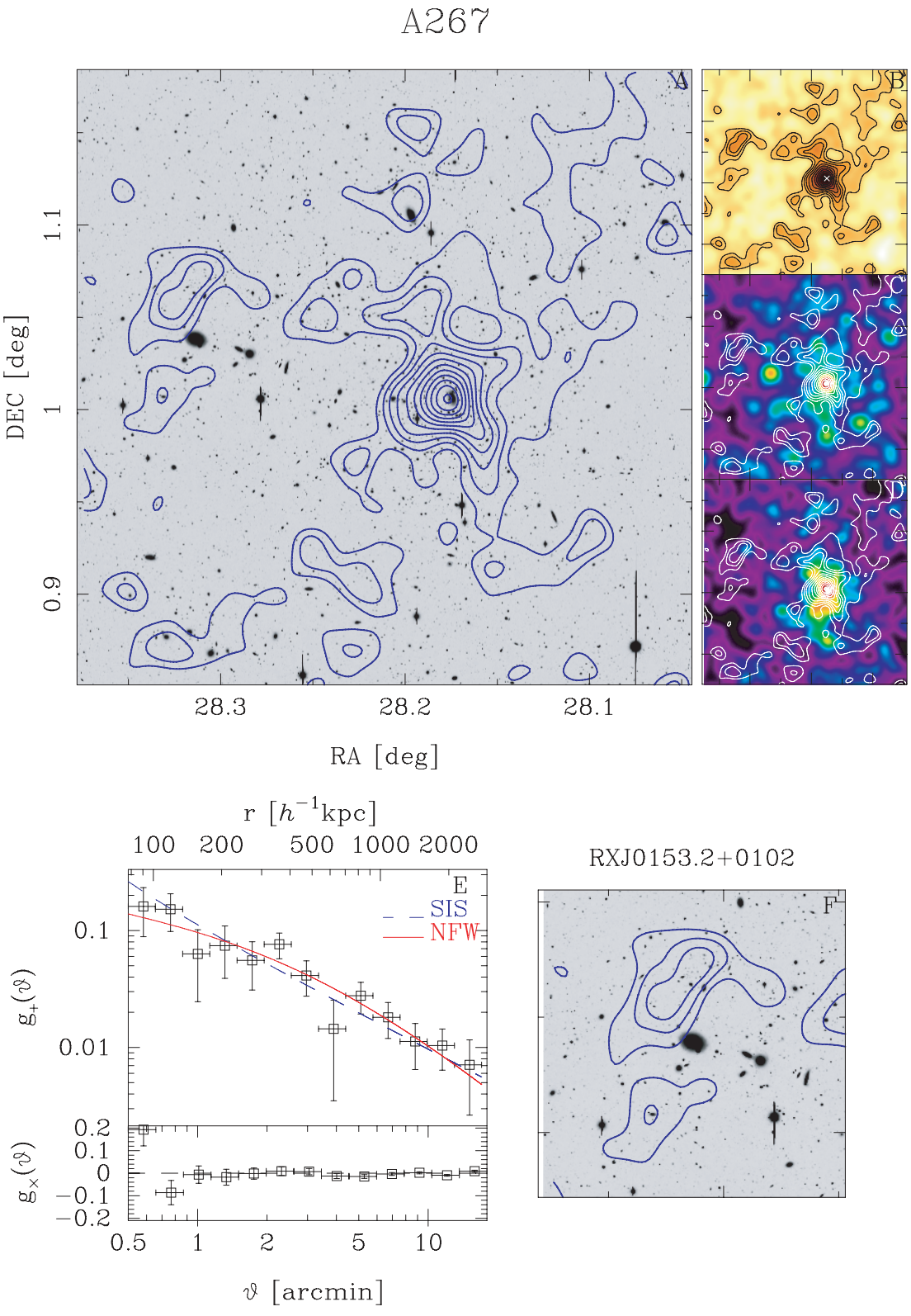

Fig. 21. Results for A 267 ($z = 0.23$). The region shown is $20' \times 20'$, the smoothing scale FWHM $= 1'.2$, and the noise level $\sigma_\kappa = 0.024$. Panel F: The region of the extended X-ray source, RX J0153.2+0102, zoomed in from panel A, indicating a bright central galaxy ($z = 0.06$) and a possible counterpart of a mass sub-clump.

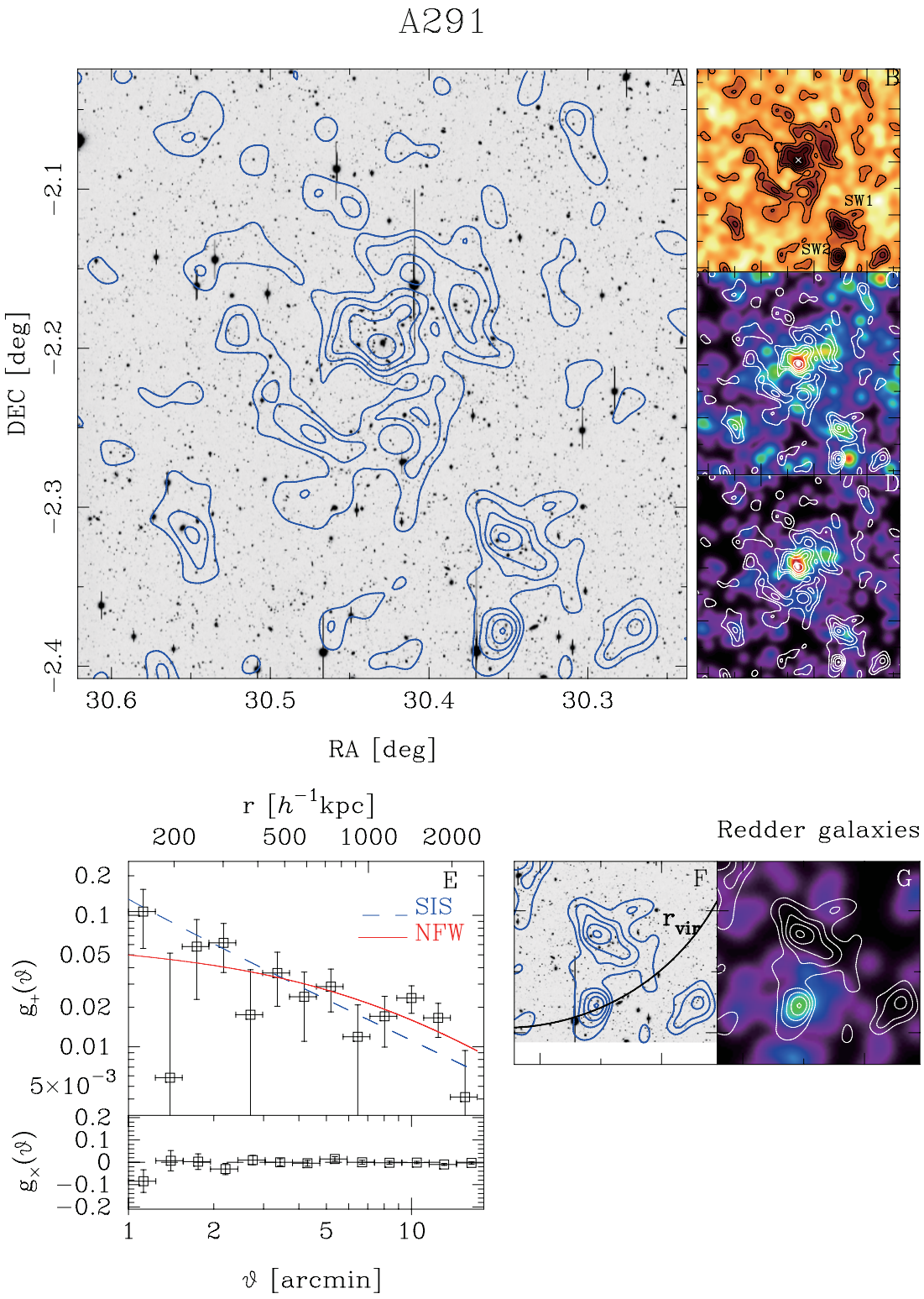

Fig. 22. Results for A 291 ($z = 0.20$). The region shown is $23' \times 23'$, the smoothing scale FWHM $= 1.'2$, and the noise level $\sigma_\kappa = 0.027$. Panel F: The region displaying sub-clumps around the virial radius (see table 6), zoomed in from the panel A. Panel G: The color scale shows the number density map of galaxies redder than the red-sequence of A 291, given as $(V - i') \simeq (V - i')_{\rm A291} + 1$ with the width $|\Delta(V - i')| \simeq 0.1$, indicating a higher-redshift cluster.

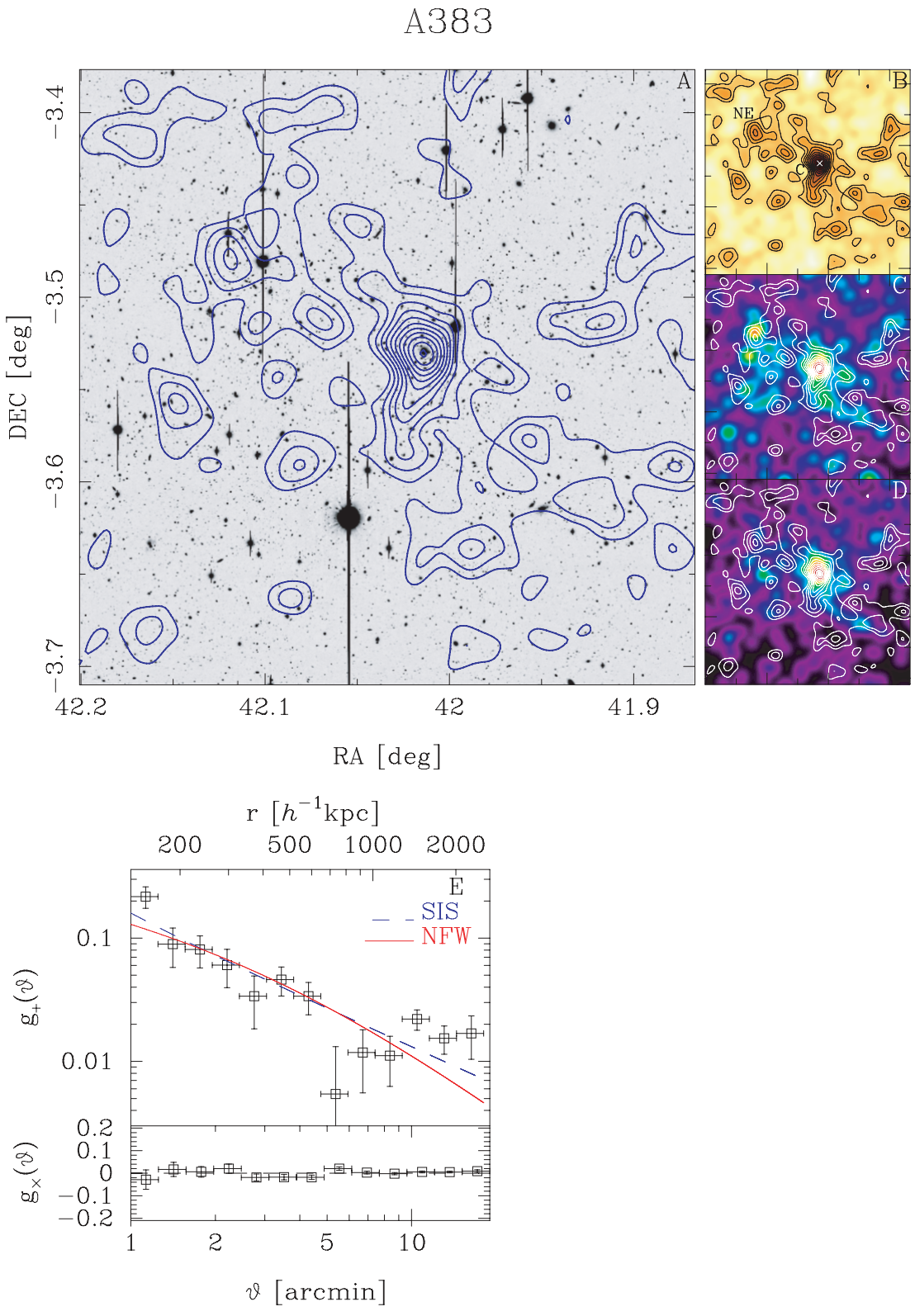

Fig. 23. Results for A 383 ($z = 0.19$). The region shown is $20' \times 20'$, the smoothing scale FWHM $= 1'.2$, and the noise level $\sigma_\kappa = 0.024$.

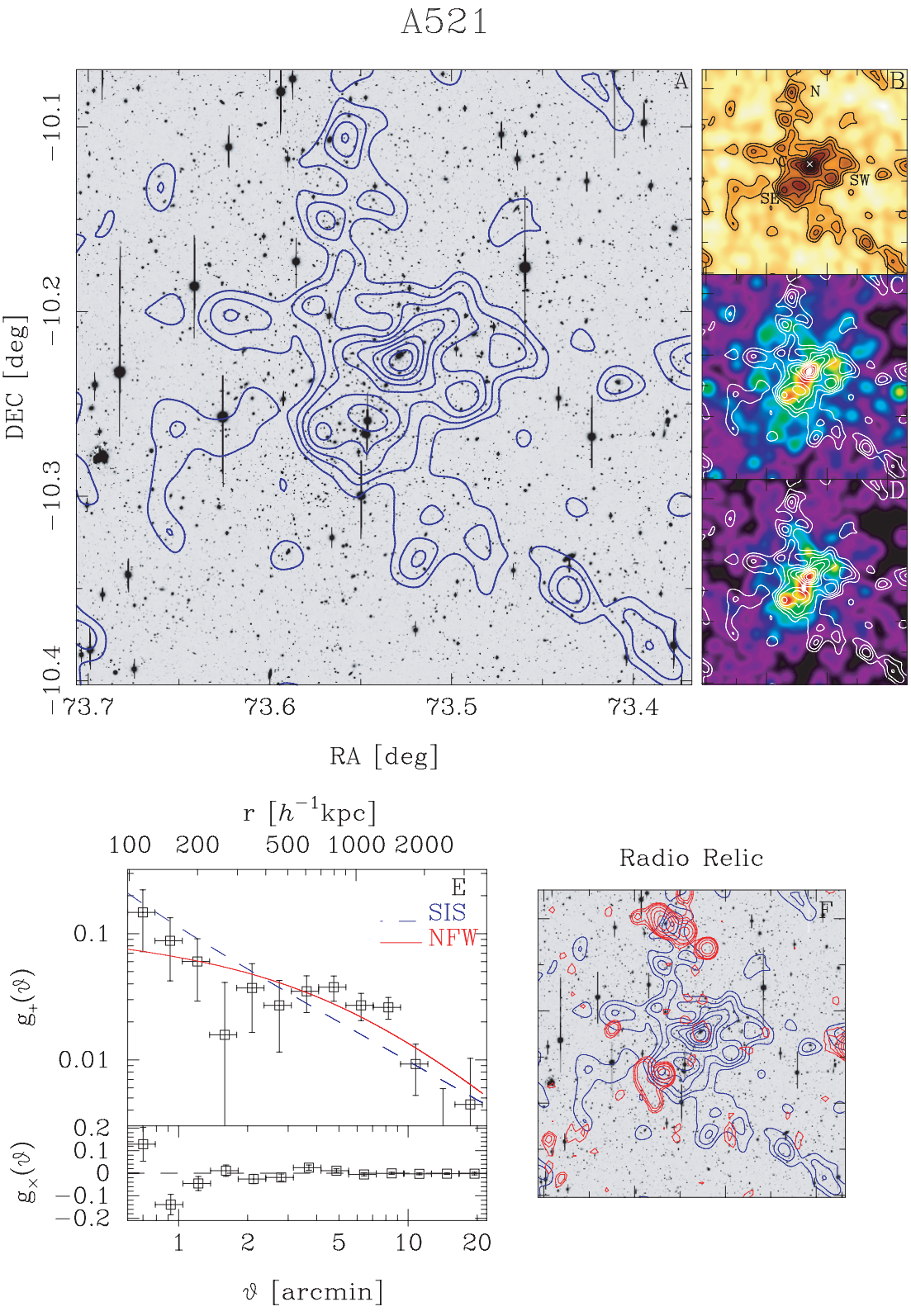

Fig. 24. Results for A 521 ($z = 0.25$). The region shown is $20' \times 20'$, the smoothing scale FWHM $= 1'.2$, and the noise level $\sigma_\kappa = 0.025$. Panel F: The red contours present the VLA diffuse sources indicating a radio relic. The contour levels are spaced as 0.9, 1.35, 2, 4, 8, 16, 32, 64, 128, and 256 mJy/beam.

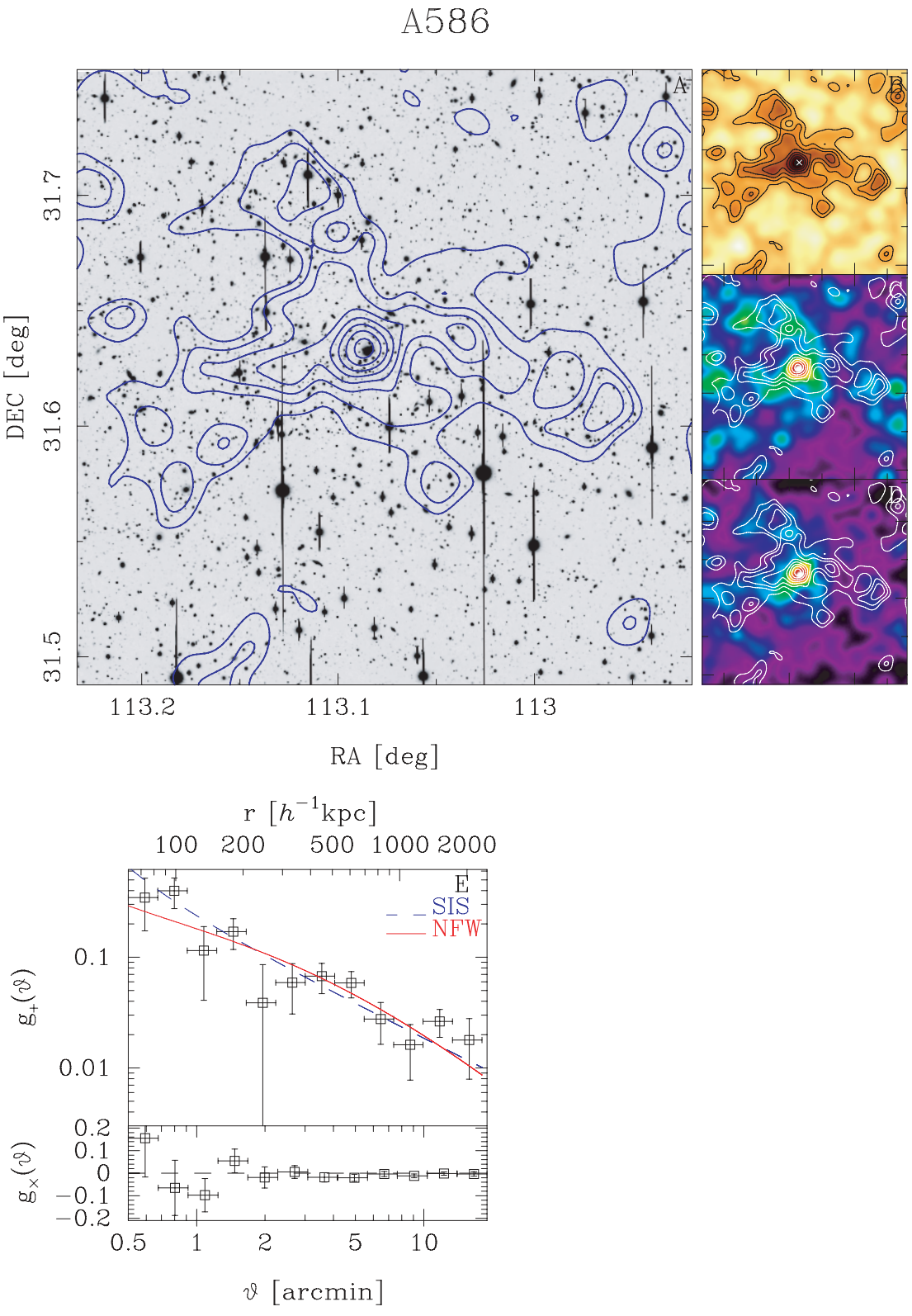

Fig. 25. Results for A 586 ($z = 0.17$). The region shown is $16' \times 16'$, the smoothing scale FWHM $= 1.'2$, and the noise level $\sigma_\kappa = 0.035$.

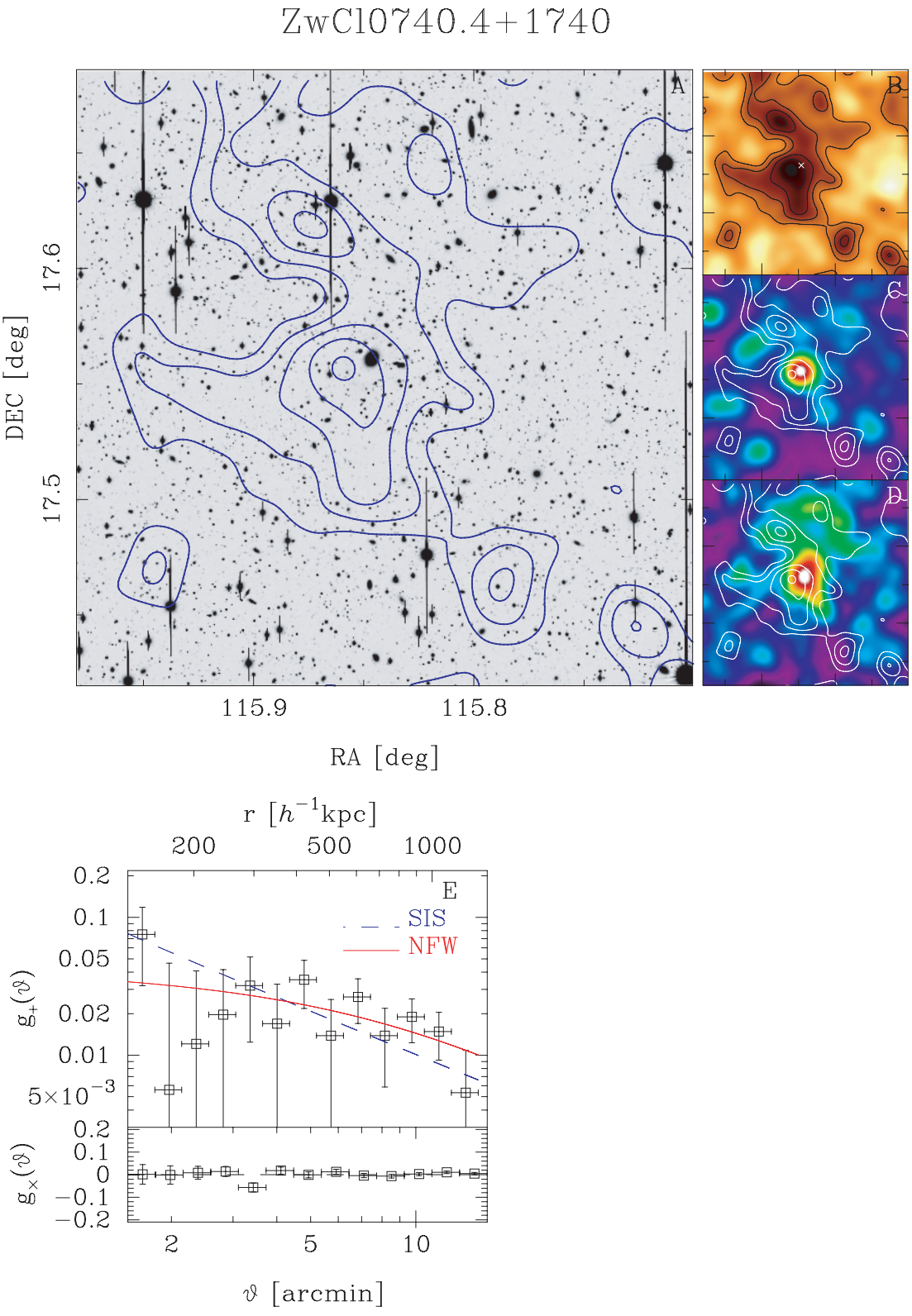

Fig. 26. Results for ZwCl 0740 (the photometric redshift $z = 0.11$). The region shown is $16' \times 16'$, the smoothing scale FWHM $= 1.'7$, and the noise level $\sigma_\kappa = 0.024$. For this cluster (similarly as in the following clusters) there is no color information, and therefore a comparison with the maps of member galaxy sample cannot be made.

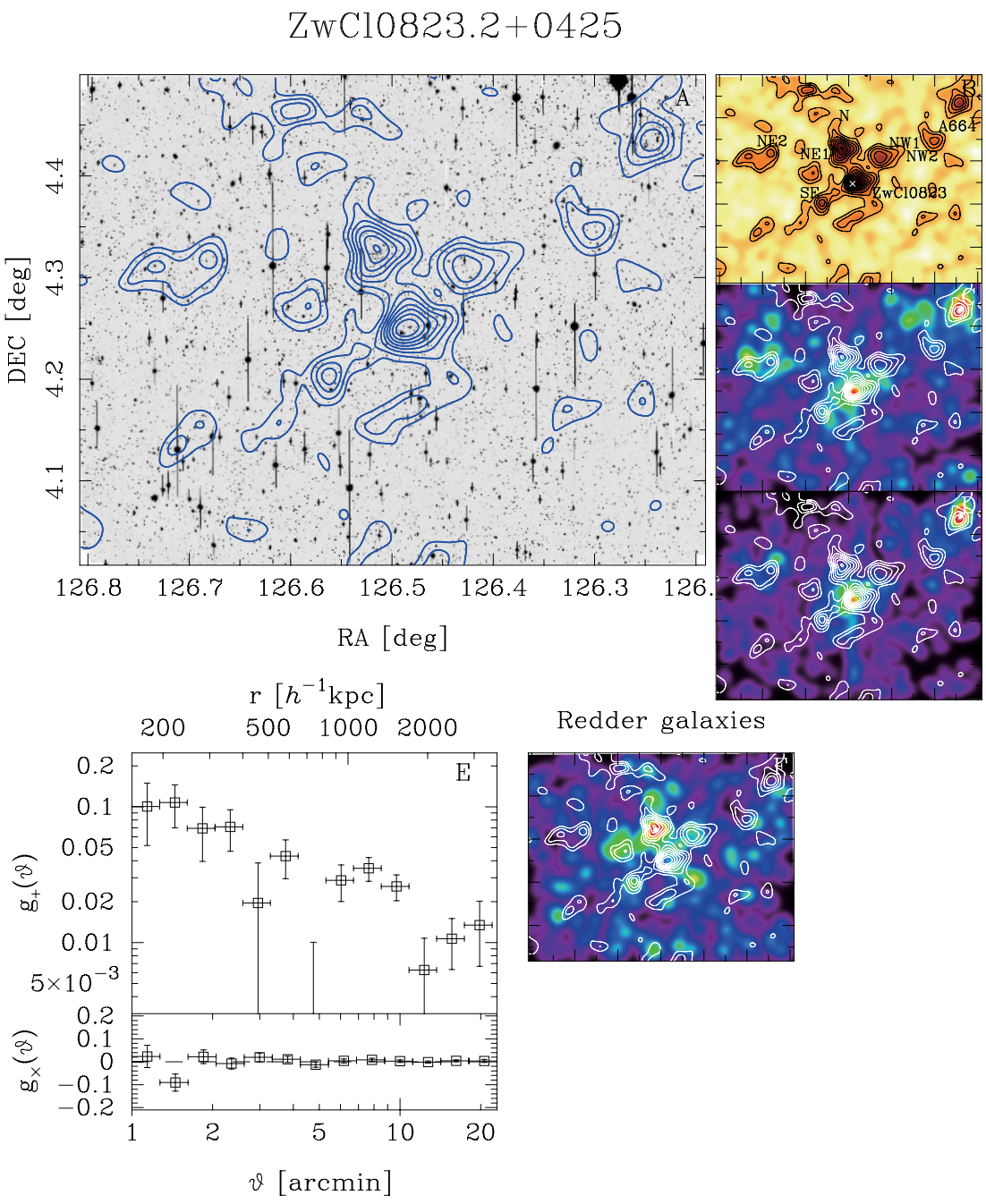

Fig. 27. Results for ZwCl 0823 ($z = 0.22$). The region shown is $37' \times 29'$, the smoothing scale FWHM $= 1.'7$, and the noise level $\sigma_\kappa = 0.022$. Panel B : Another cluster (A 664 at $z = 0.27$) is located near at the upper-right corner in the mass map, based on the SDSS catalogue. Panel C: The luminosity map for the member galaxy sample. Panel D: The luminosity density map of galaxies redder than the cluster red-sequence, as given by $(V-i') \simeq (V-i')_{\rm ZwCl0823} + 0.75$, $|\Delta(V-i')| \simeq 0.15$, indicating the galaxy concentrations at higher redshifts (probably $z \sim 0.5$) that are superposed on the top of one mass clump located at the north region from ZwCl 0823. Panel E: Radial distortion profiles. However, since there are prominent substructures, a more precisely bimodal mass distribution, seen in the mass map and the clear cluster center cannot be defined, we did not use the measured profile to constrain the spherical mass profile model for this cluster.

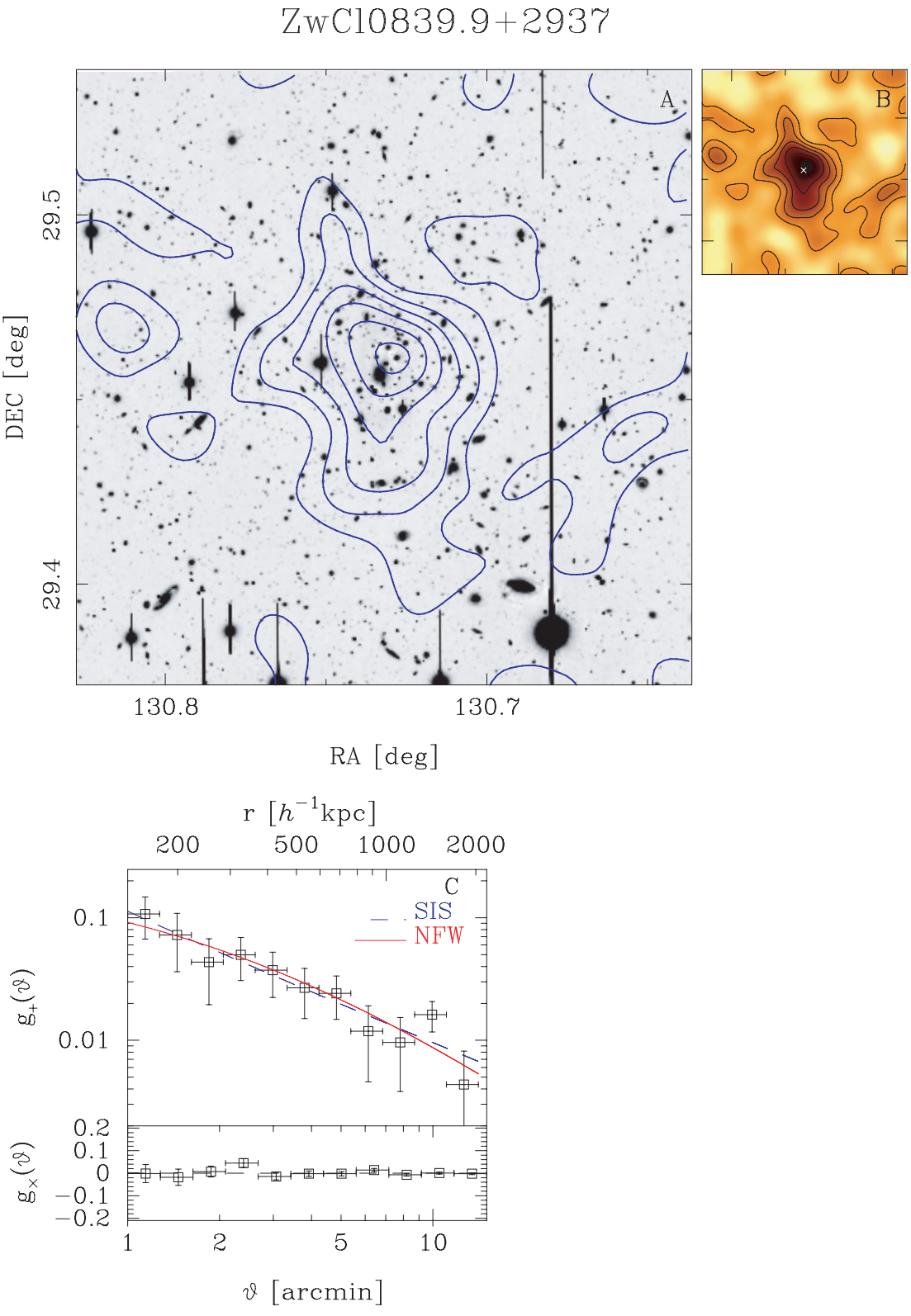

Fig. 28. Results for ZwCl 0839 ($z = 0.19$). The region shown is $10' \times 10'$, the smoothing scale FWHM $= 1'.2$, and the noise level $\sigma_\kappa = 0.031$.

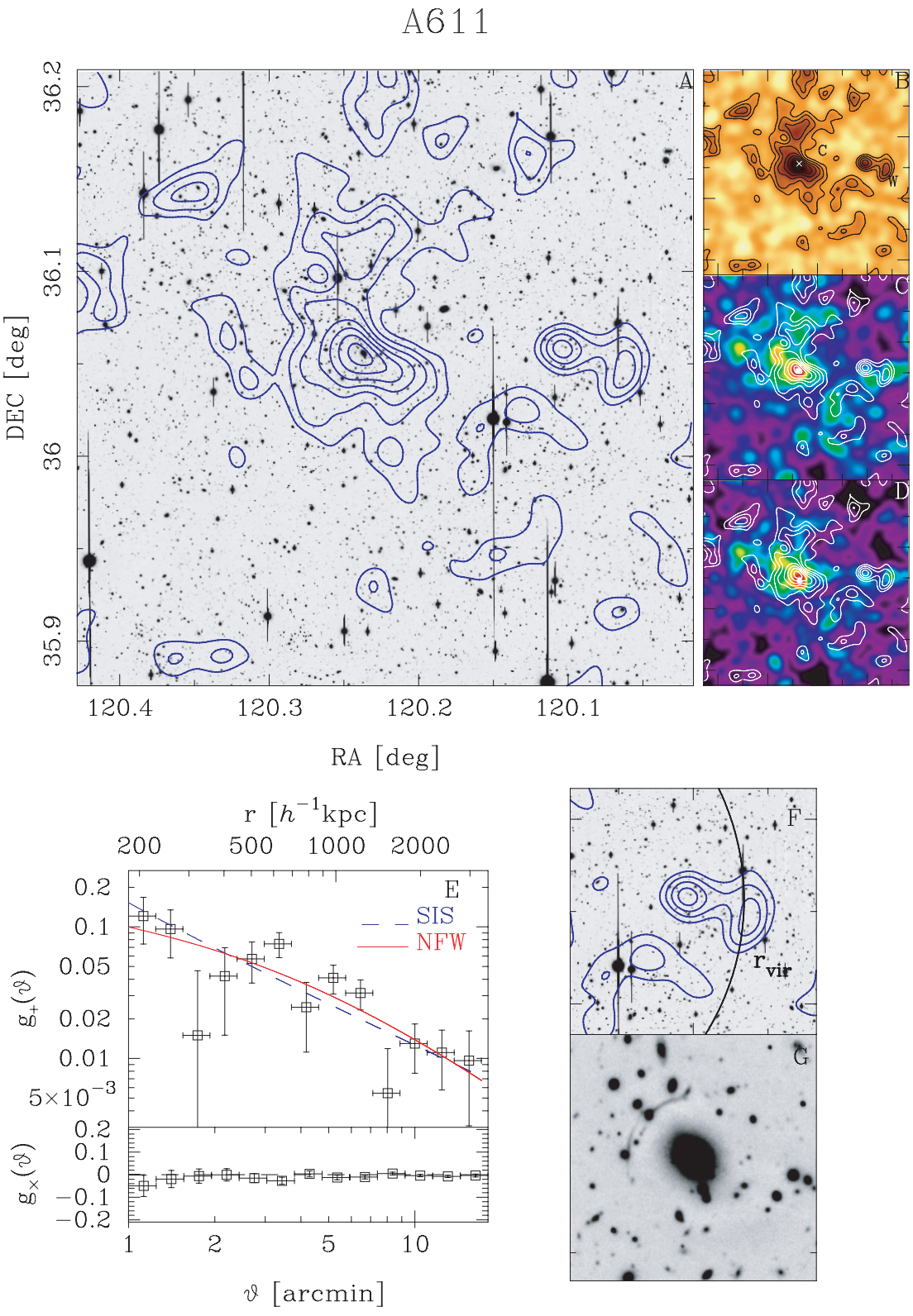

Fig. 29. Results for A 611 ($z = 0.29$). The region shown is $20' \times 20'$, the smoothing scale FWHM $= 1.'2$, and the noise level $\sigma_\kappa = 0.028$. Panel F: Possible sub-clump around the virial radius. Panel G: A newly discovered giant arc near to the cluster center, zoomed in from panel A.

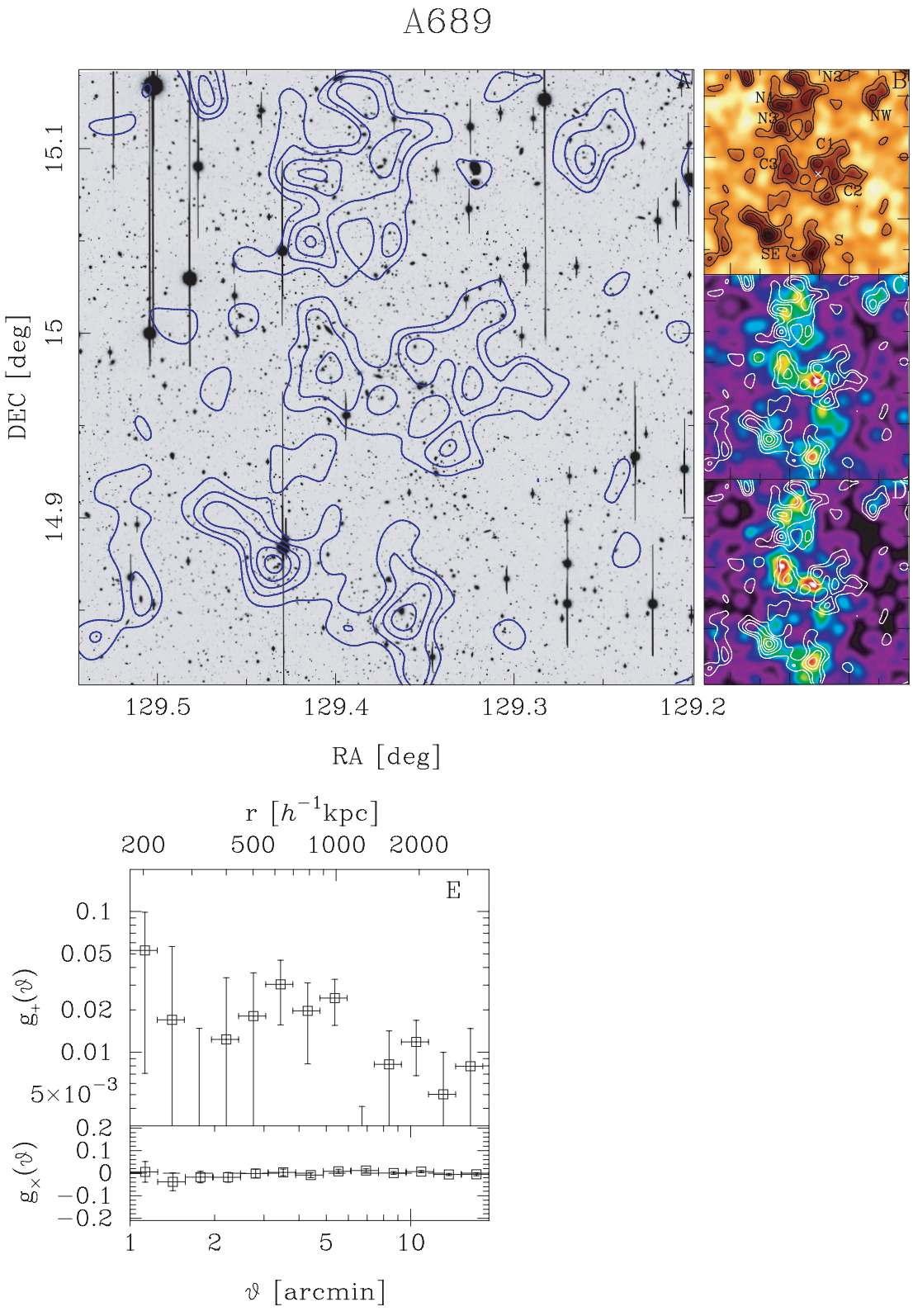

Fig. 30. Results for A 689 ($z = 0.28$). The region shown is $20' \times 20'$, the smoothing scale FWHM $= 1.'2$, and the noise level $\sigma_\kappa = 0.026$. Panel E: As in figure 27, the measured profile was not used to constrain the spherical mass profile models, because of the presence of prominent substructures in the mass maps.

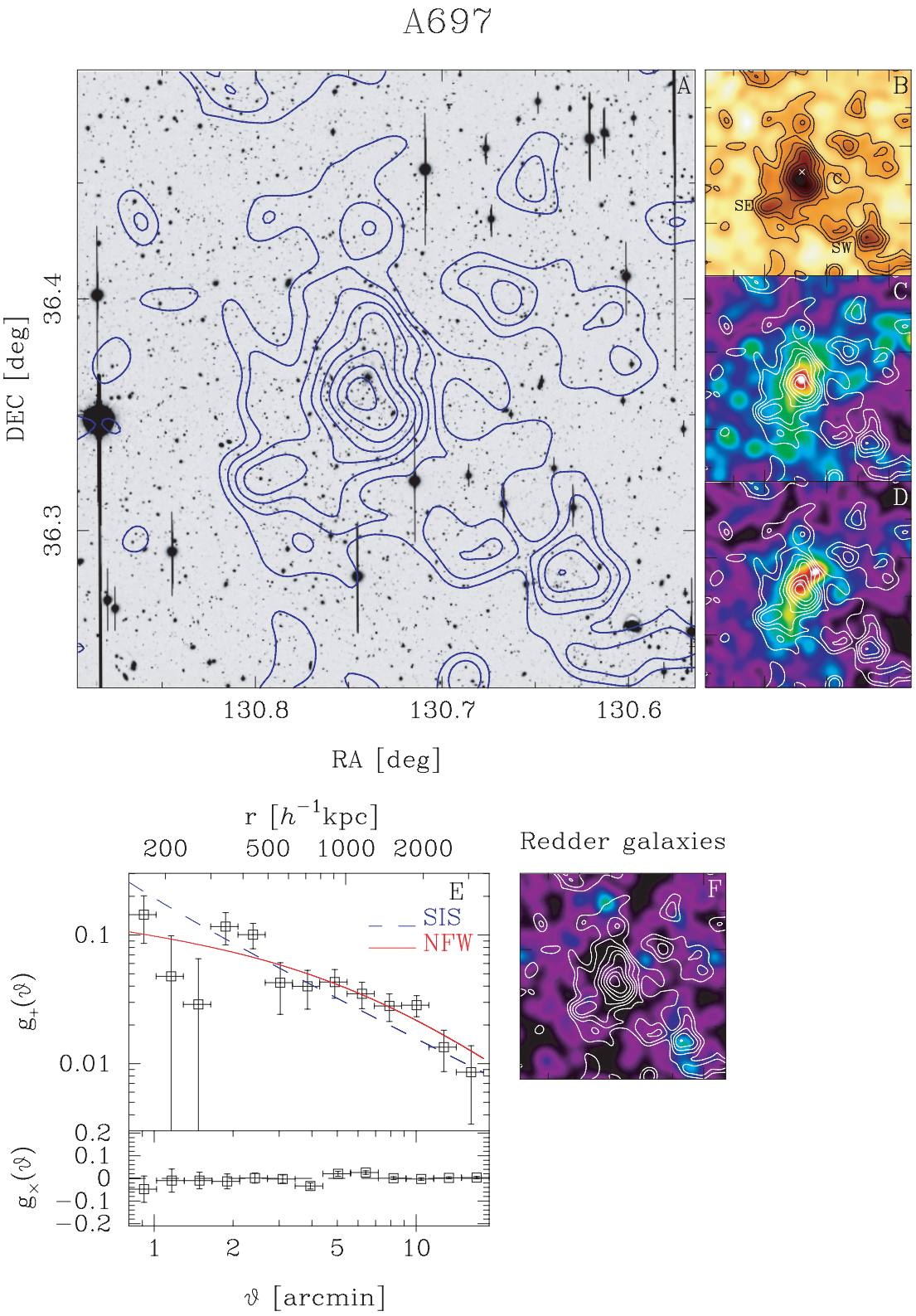

Fig. 31. Results for A 697 ($z = 0.28$). The region shown is $16' \times 16'$, the smoothing scale FWHM $= 1.'2$, and the noise level $\sigma_\kappa = 0.027$. Panel F: Density map of galaxies redder than the cluster red-sequence, as given by $(V - i') \simeq (V - i')_{\rm A697} + 0.9$ with a width of $|\Delta(V - i')| \simeq 0.15$.

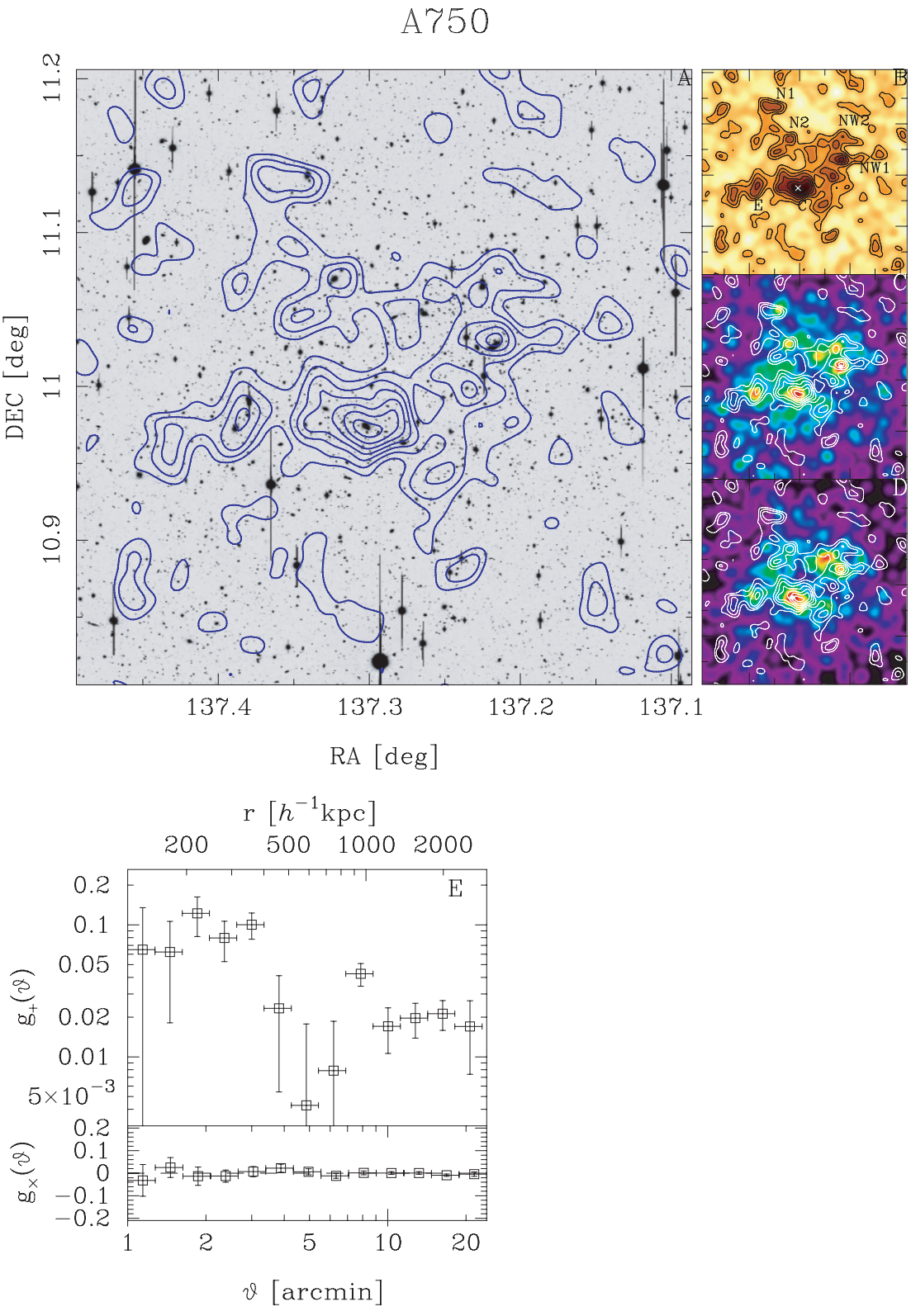

Fig. 32. Results for A 750 ($z = 0.16$). The region shown is $24' \times 24'$, the smoothing scale FWHM $= 1.'2$, and the noise level $\sigma_\kappa = 0.030$. Panel E: As in figure 27, the measured profile was not used to constrain the spherical mass profile models, because of the presence of prominent substructures in the mass maps.

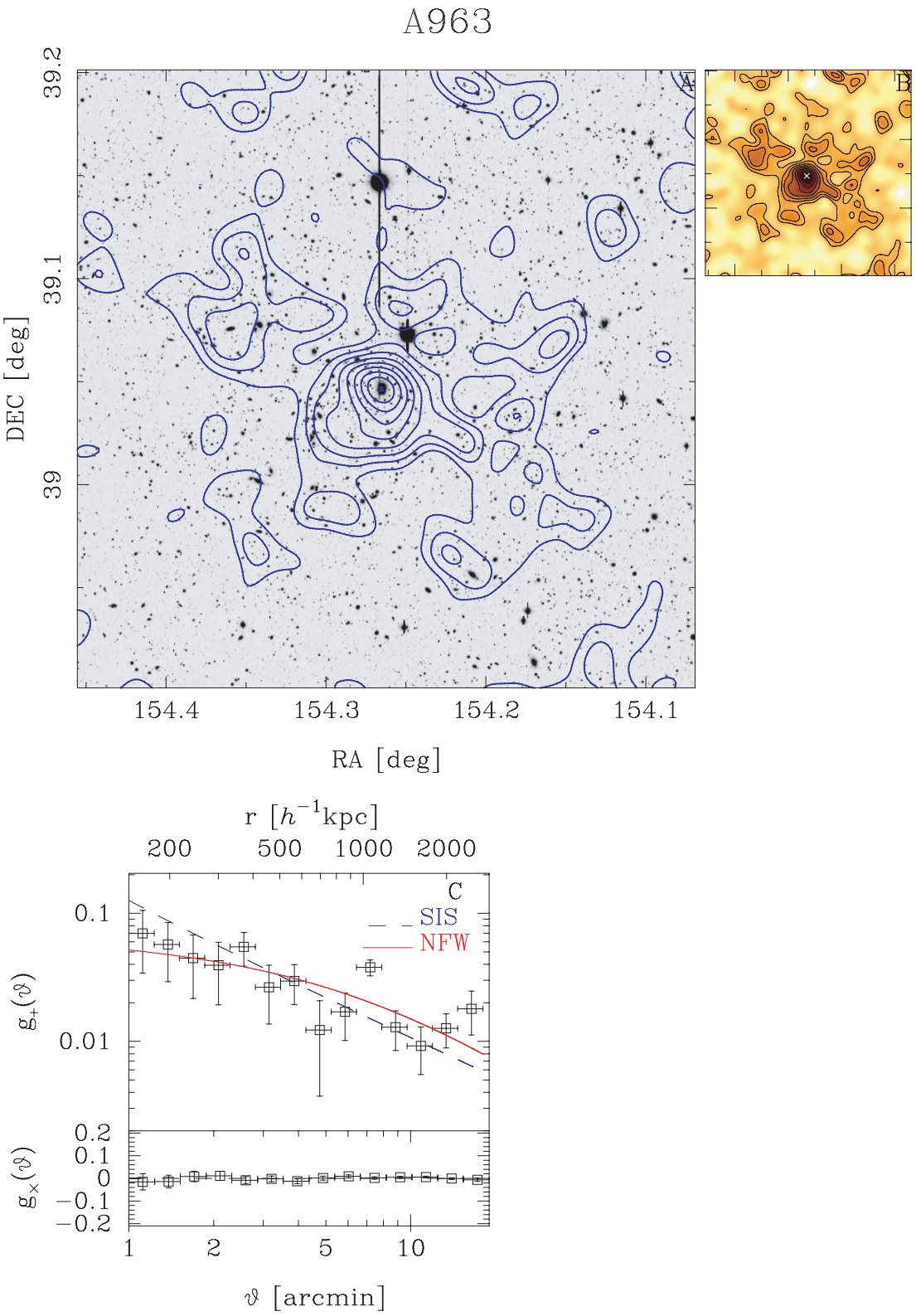

Fig. 33. Results for A 963 ($z = 0.21$). The region shown is $18' \times 18'$, the smoothing scale FWHM $= 1'.2$, and the noise level $\sigma_\kappa = 0.027$.

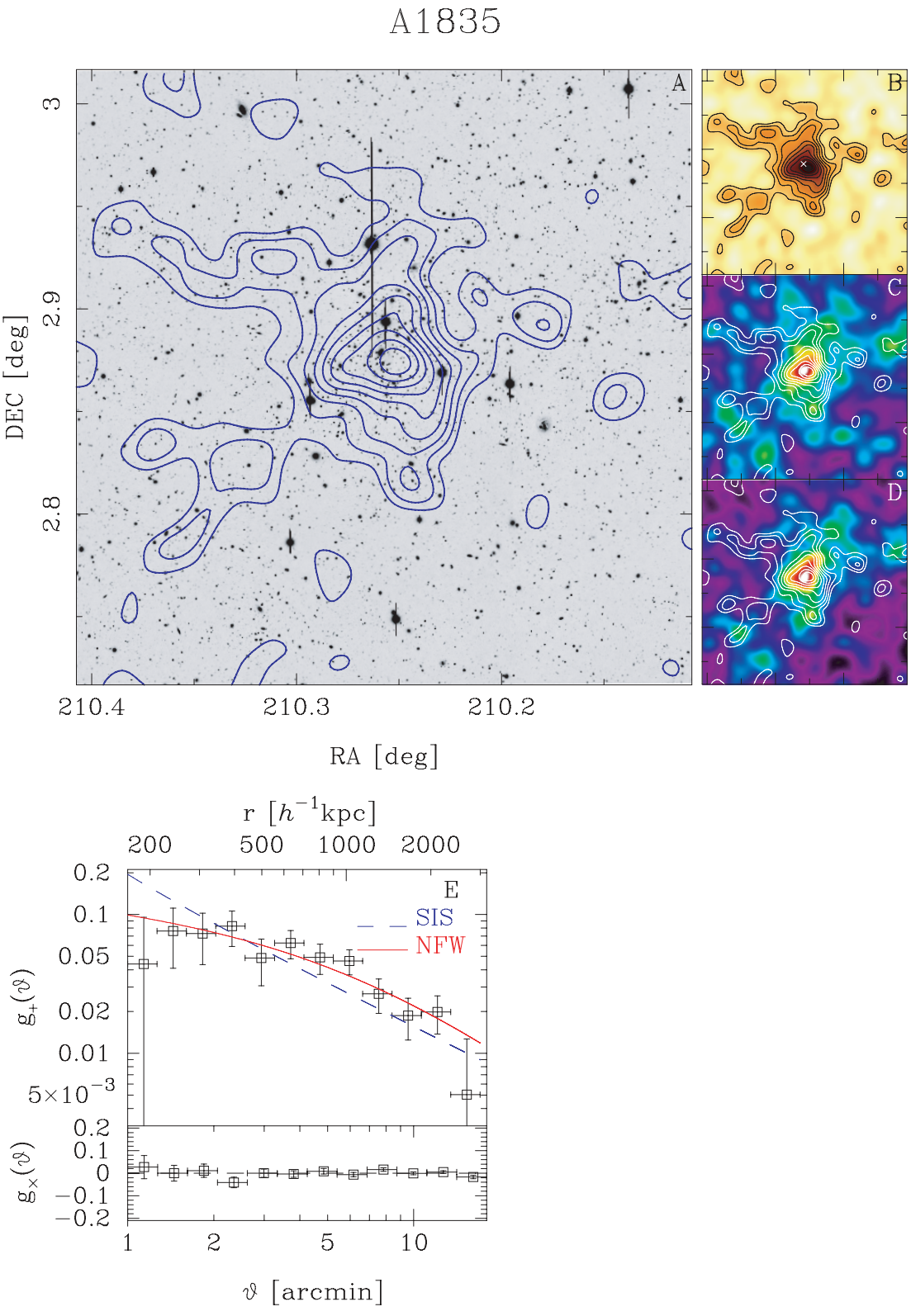

Fig. 34. Results for A 1835 ($z = 0.25$). The region shown is $18' \times 18'$, the smoothing scale FWHM $= 1.'3$, and the noise level $\sigma_\kappa = 0.031$.

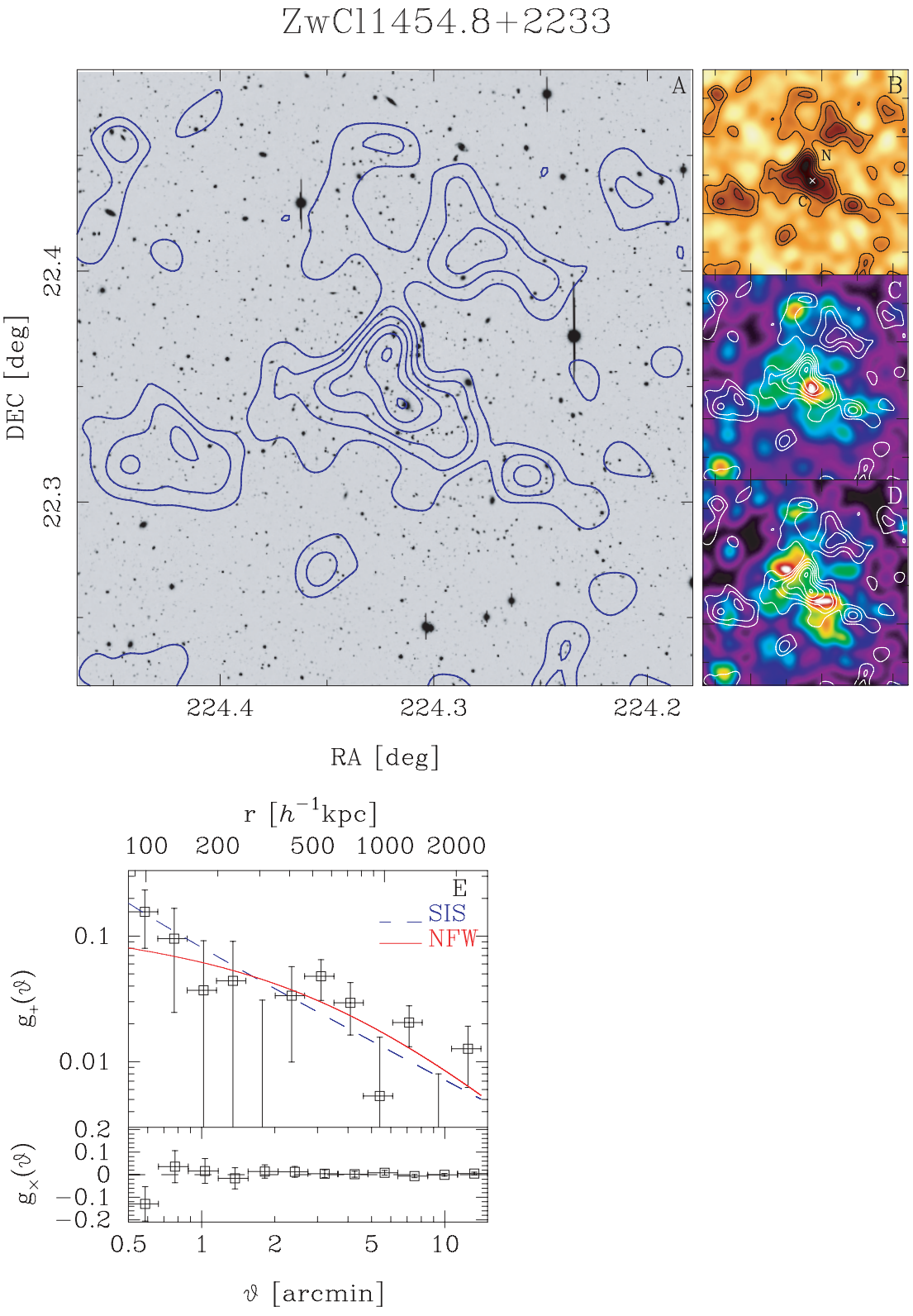

Fig. 35. Results for ZwCl 1454 (also known as MS1455.0+2232 at $z = 0.26$). The region shown is $16' \times 16'$, the smoothing scale FWHM $= 1.'2$, and the noise level $\sigma_\kappa = 0.031$.

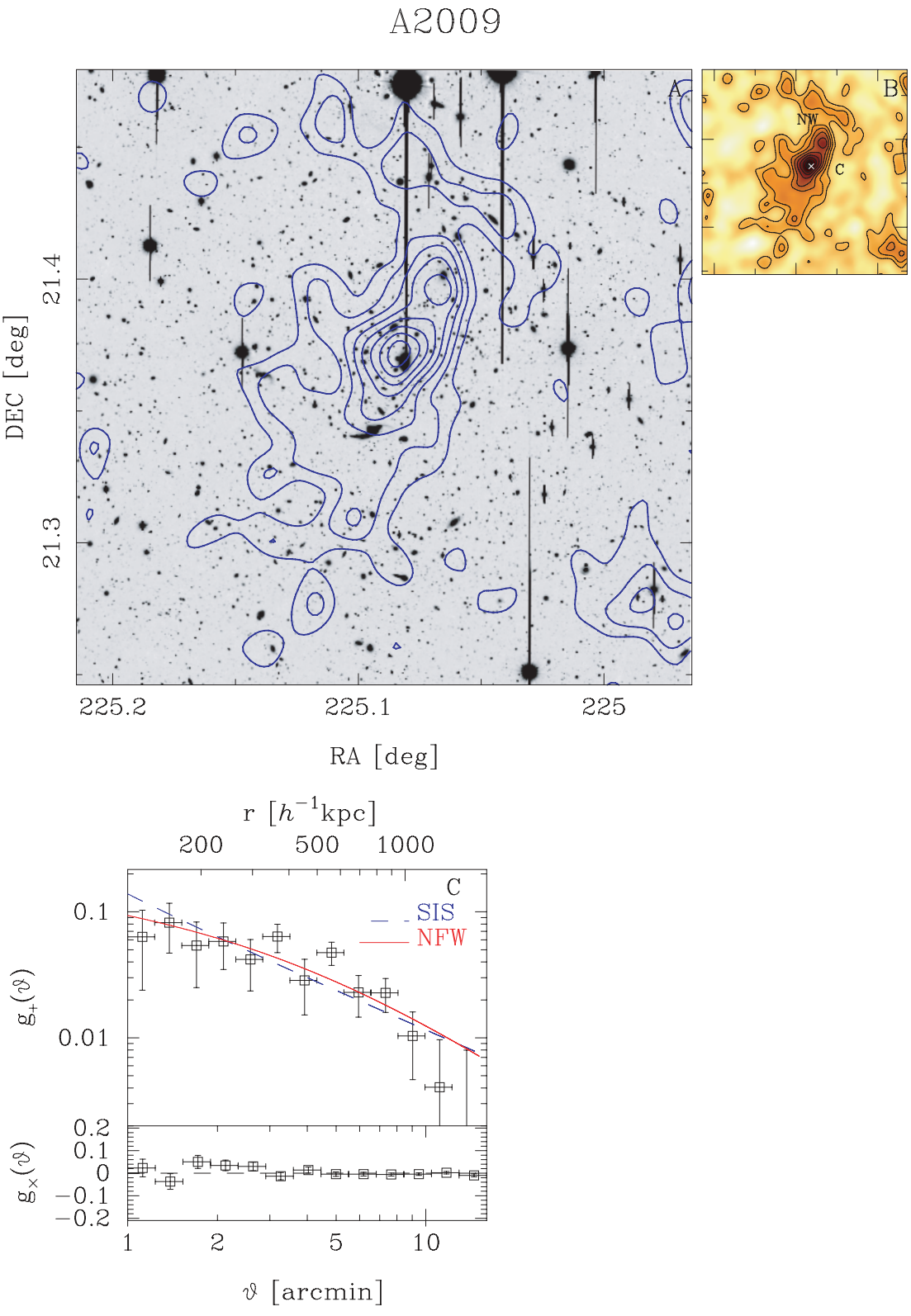

Fig. 36. Results for A 2009 ($z = 0.15$). The region shown is $14' \times 14'$, the smoothing scale FWHM $= 1.'0$, and the noise level $\sigma_\kappa = 0.038$.

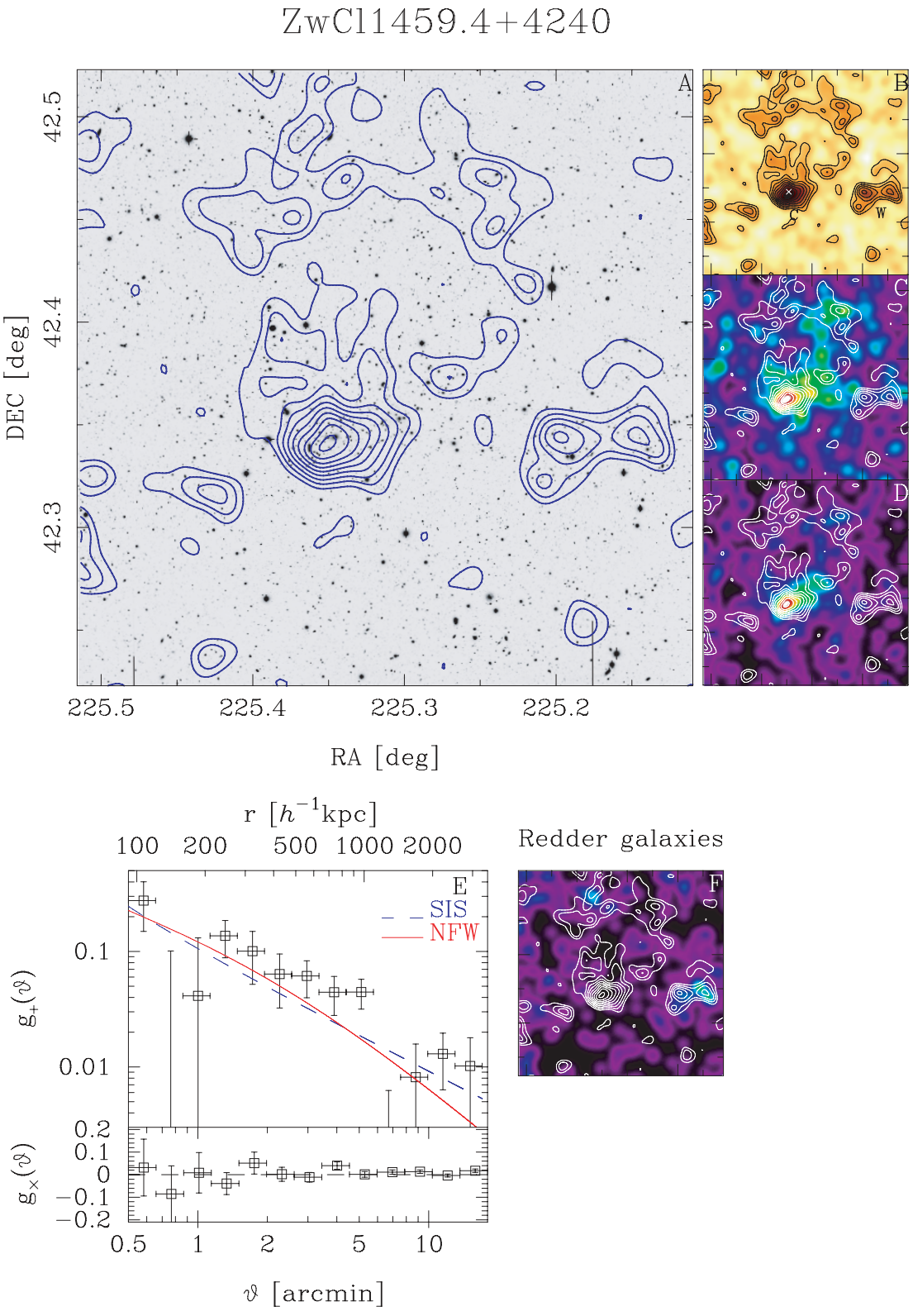

Fig. 37. Results for ZwCl 1459 ($z = 0.29$). The region shown is $18' \times 18'$, the smoothing scale FWHM $= 1.'0$, and the noise level $\sigma_\kappa = 0.025$. Panel F: Luminosity map of galaxies redder than the red-sequence, given as $(V - R_c) \simeq (V - R_c)_{\rm ZwCl1459} + 0.4$ with the width $|\Delta(V - R_c)| \simeq 0.1$.

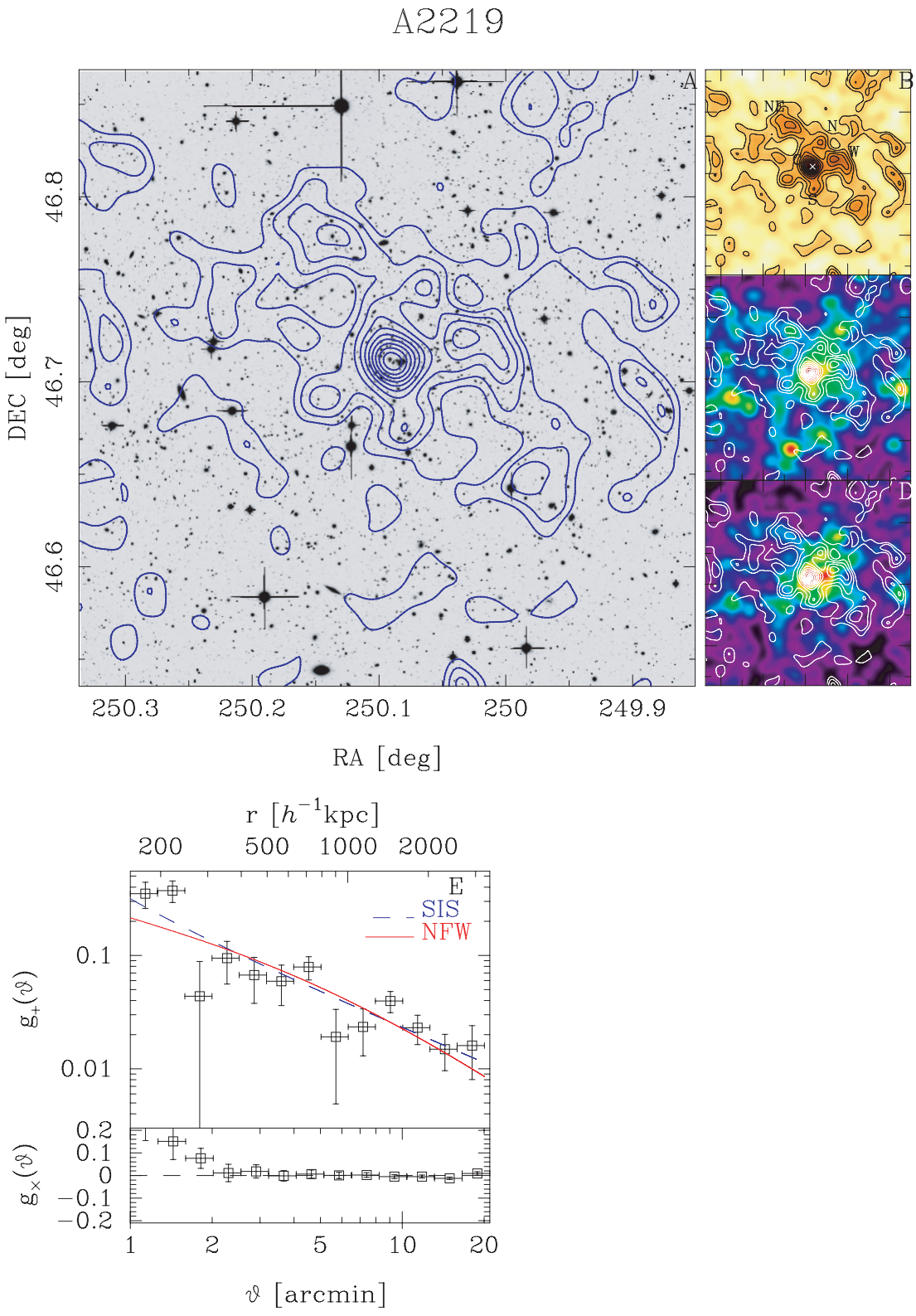

Fig. 38. Results for A 2219 ($z = 0.23$). The region shown is $20' \times 20'$, the smoothing scale FWHM $= 1'.2$, and the noise level $\sigma_\kappa = 0.034$.

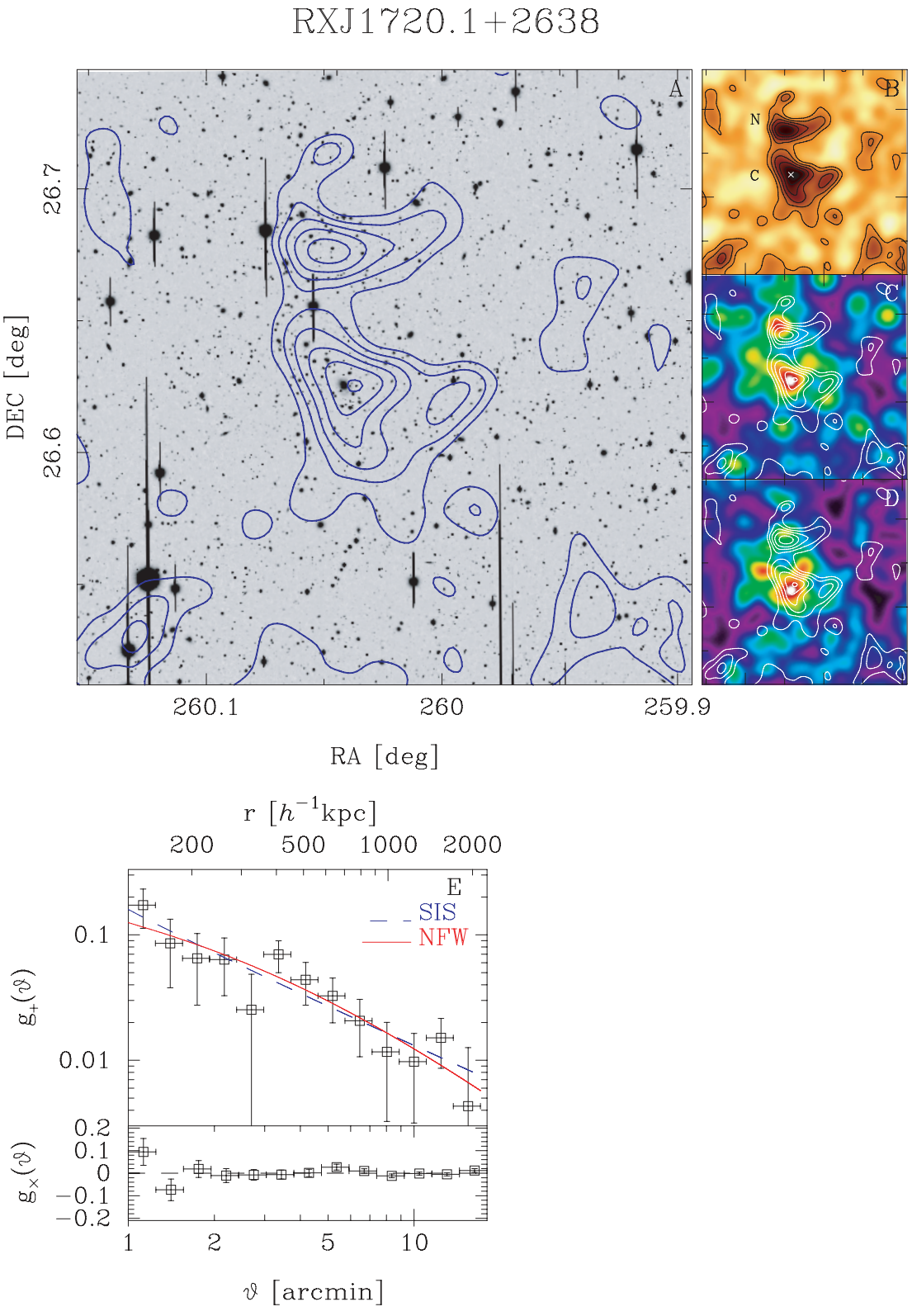

Fig. 39. Results for RX J1720 ($z = 0.16$). The region shown is $14' \times 14'$, the smoothing scale FWHM $= 1.'2$, and the noise level $\sigma_\kappa = 0.033$.

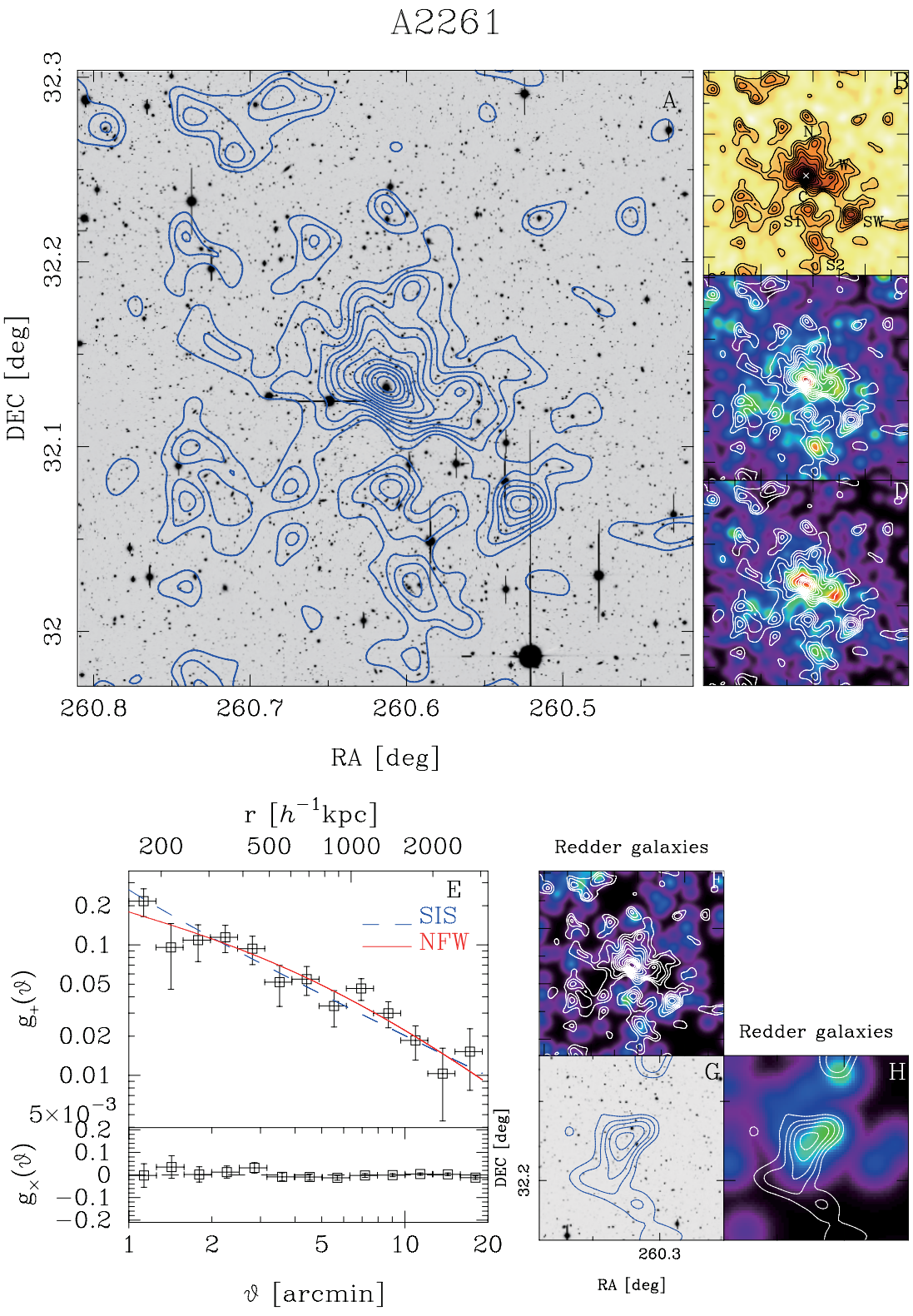

Fig. 40. Results for A 2261 ($z = 0.22$). The region shown is $20' \times 20'$, The smoothing scale FWHM $= 1.'0$, and the noise level $\sigma_\kappa = 0.029$. Panel F: Luminosity map of galaxies redder than the red-sequence of A 2261, given as $(V - R_c) \simeq (V - R_c)_{A2261} + 0.6$ with the width $|\Delta(V - R_c)| \simeq 0.1$ roughly corresponding to $z \sim 0.5$. Panel G: Sub-clump located at the north-west region from the cluster center, outside the mass map in the panel A. Panel H: Luminosity map of redder galaxies, as in panel G.

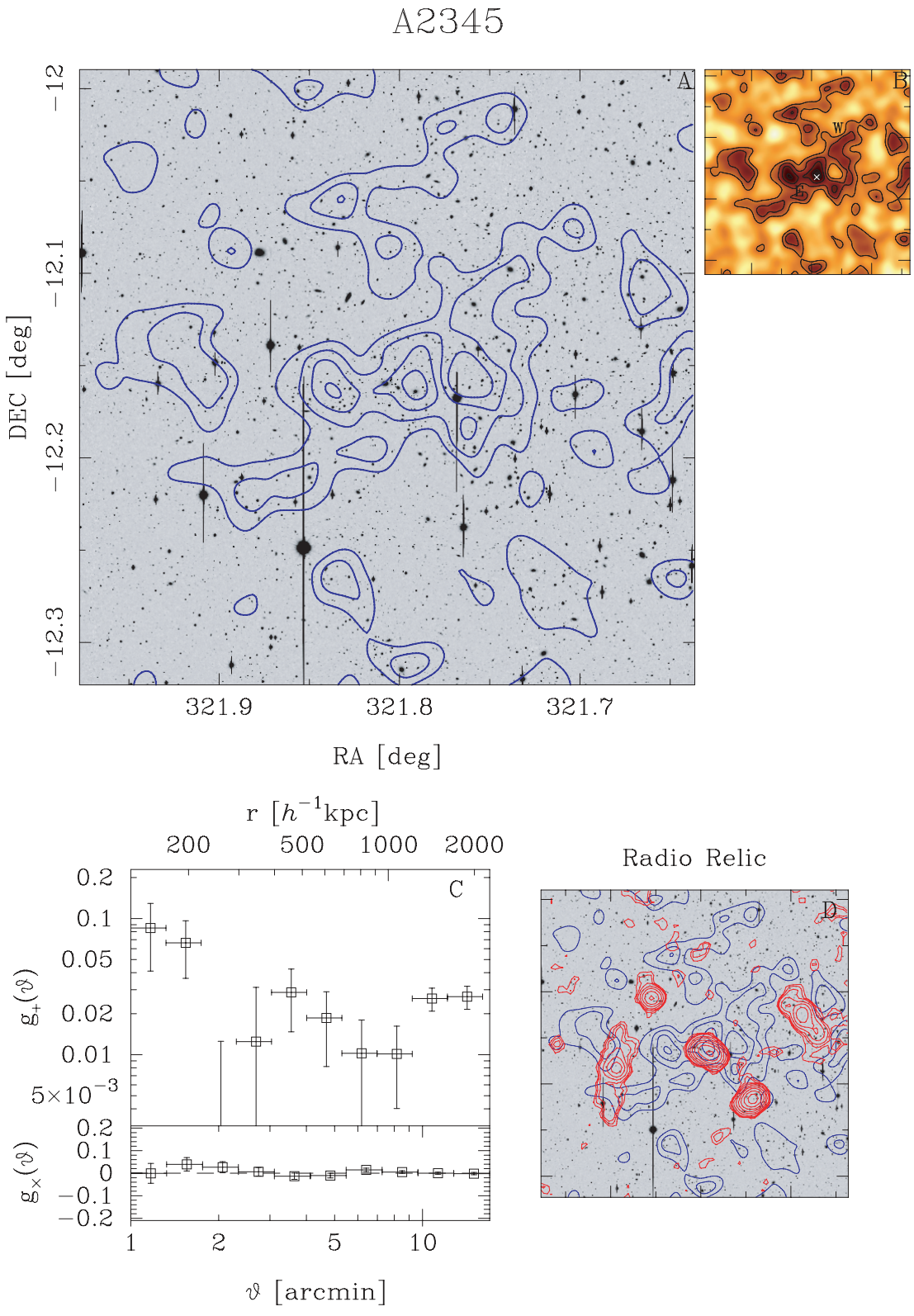

Fig. 41. Results for A 2345 ($z = 0.18$). The region shown is $20' \times 20'$, the smoothing scale FWHM $= 1'.2$, and the noise level $\sigma_\kappa = 0.037$. Panel D: Gray (red in E-version) contours show VLA diffuse sources, indicating double radio relics. The contour levels are spaced as 0.9, 1.35, 2, 4, 8, 16, 32, 64, 128, 256 mJy/beam. Panel E: As in figure 27, the measured profile was not used to constrain the spherical mass profile models, because of the presence of prominent substructures in the mass maps.

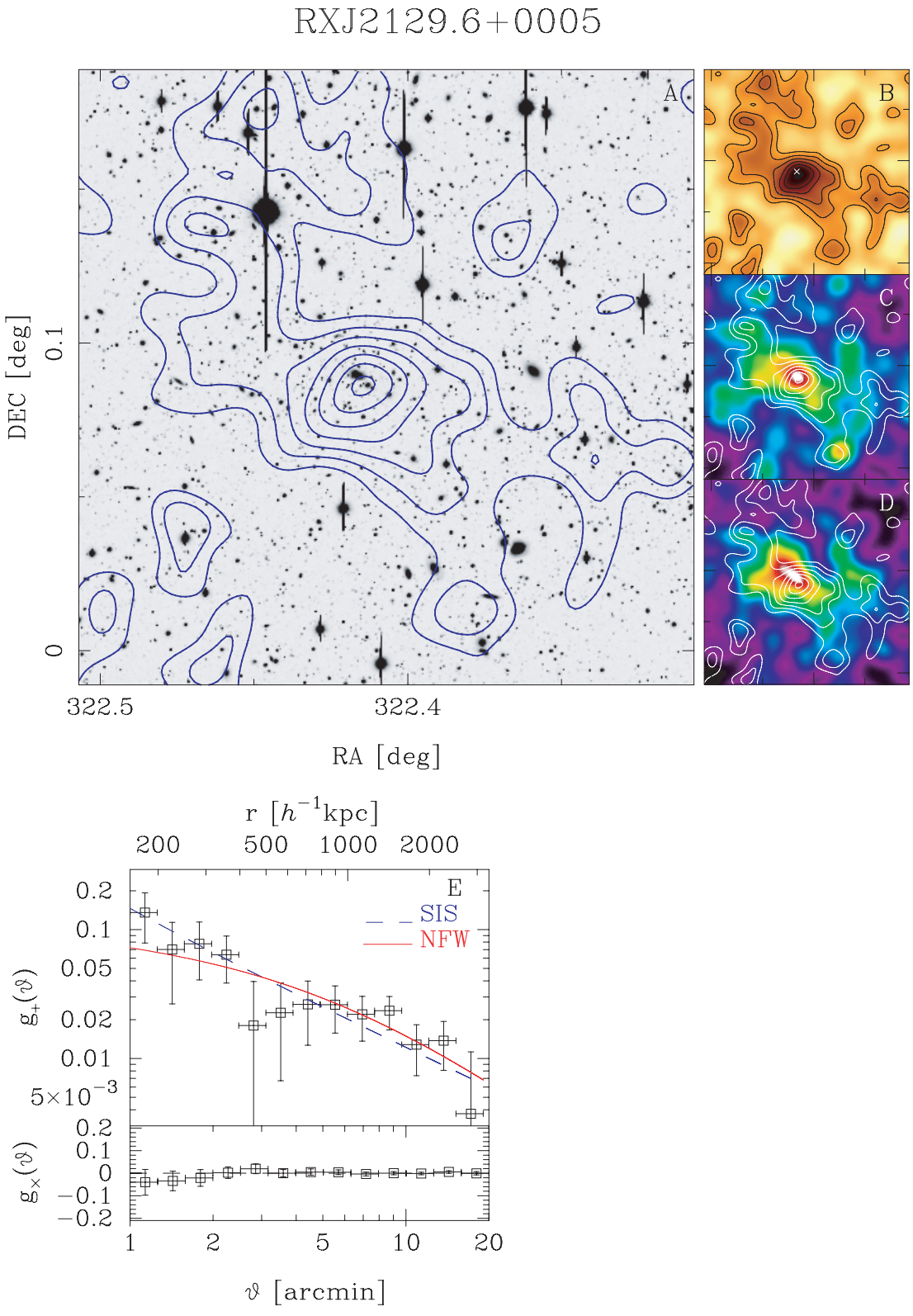

Fig. 42. Results for RX J2129 ($z = 0.24$). The region shown is $12' \times 12'$, the smoothing scale FWHM $= 1.'2$, and the noise level $\sigma_\kappa = 0.032$.

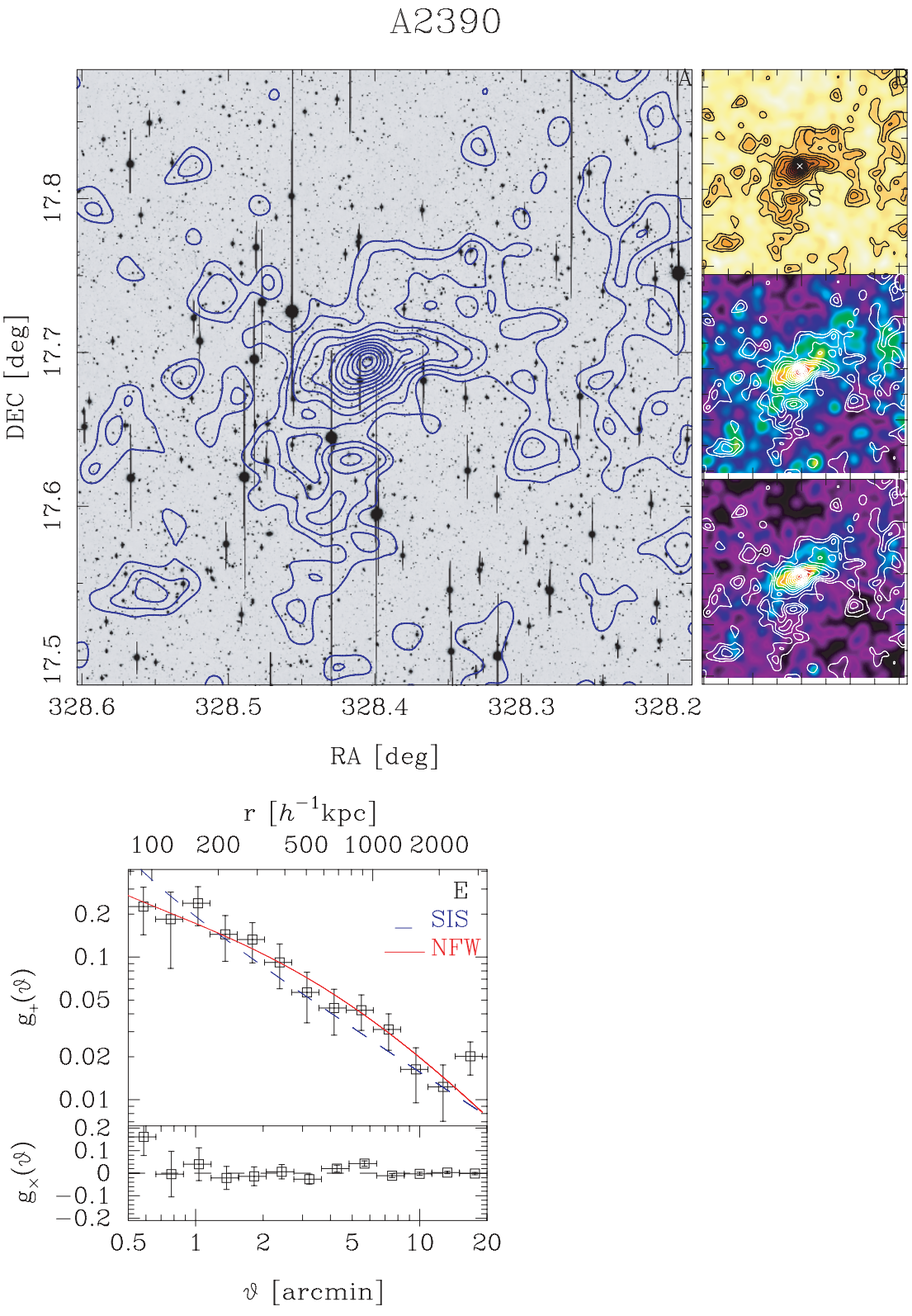

Fig. 43. Results for A 2390 ($z = 0.23$). The region shown is $24' \times 24'$, the smoothing scale FWHM $= 1'.2$, and the noise level $\sigma_\kappa = 0.028$.

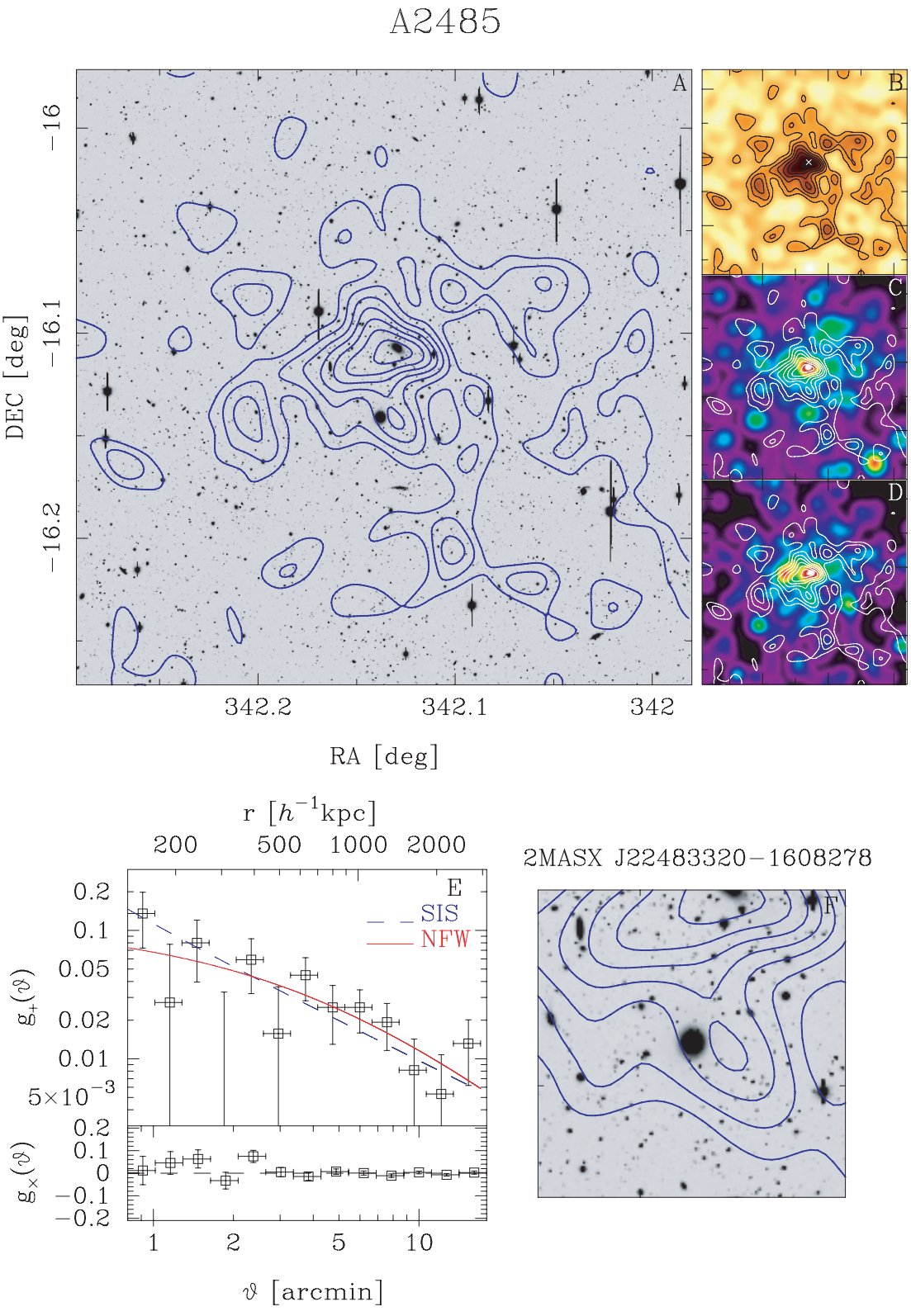

Fig. 44. Results for A 2485 ($z = 0.25$). The region shown is $18' \times 18'$, the smoothing scale FWHM $= 1'.2$, and the noise level $\sigma_\kappa = 0.026$. Panel F: Region of 2MASX J22483320−1608278 ($z = 0.119$).

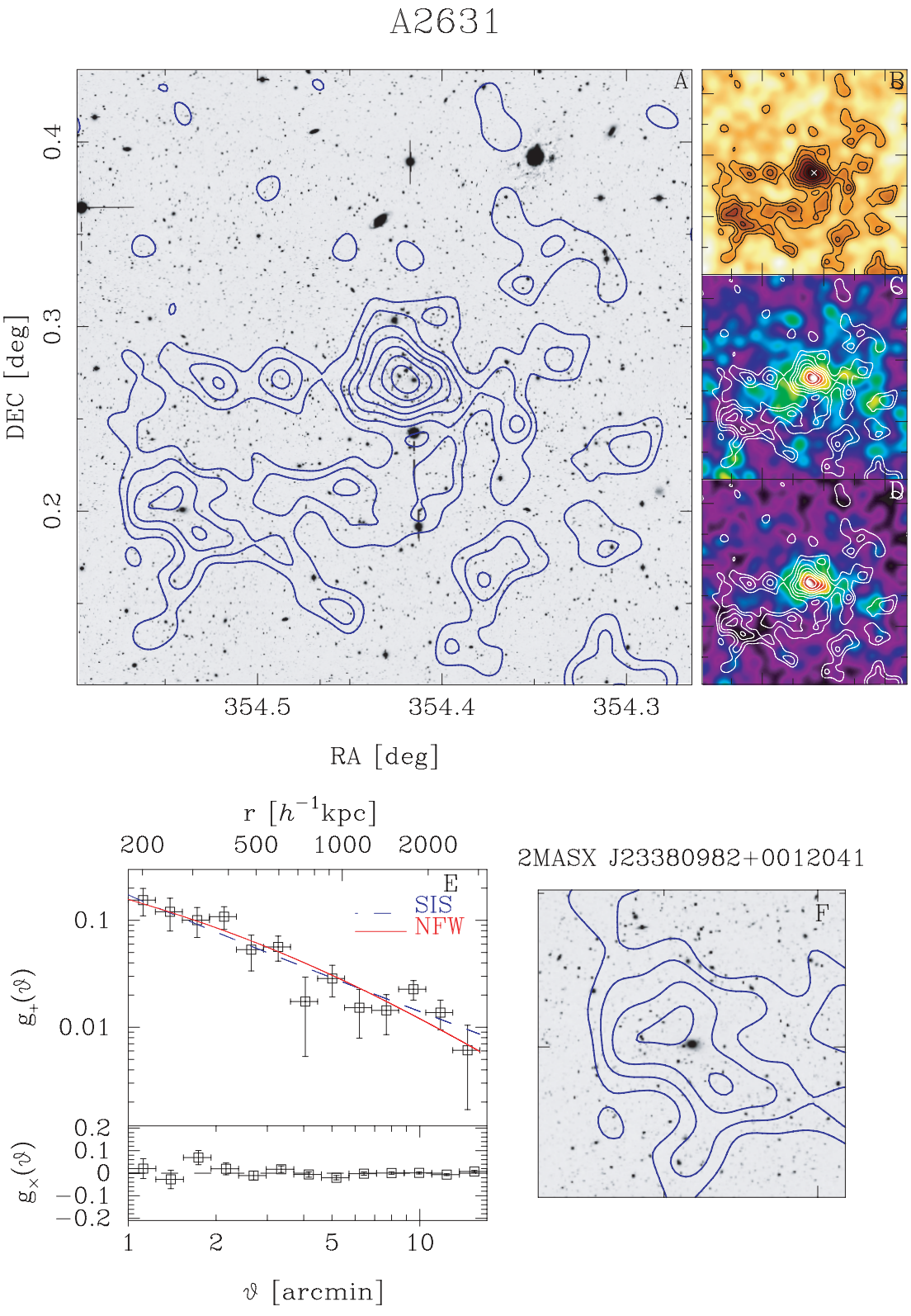

Fig. 45. Results for A 2631 ($z = 0.28$). The region shown is $20' \times 20'$, the smoothing scale FWHM $= 1'.2$, and the noise level $\sigma_\kappa = 0.025$. Panel F: 2MASX J23380982+0012041 ($z = 0.116$)

the background galaxy sample defined with the single color cut $|\Delta\mathrm{color}| = 0.3$ is used, compared to the results of our fiducial red + blue galaxy samples. It can be found that the results for two different samples are consistent within the statistical errors. Thus, our background galaxy selection is again considered to be robust. Even so, we believe that it is more secure to define the background galaxy catalog by setting the color cut on a cluster-by-cluster basis, because the slope and normalization of the red-sequence is different for each cluster, and the populations of member galaxies may also significantly differ for different clusters. More color information is needed to further refine the background galaxy selection based on improved photo-z information, which is our future project.

Appendix 2. 2D and 3D Aperture Masses for an NFW Model

The 3D mass enclosed within a sphere of a given radius r_Δ [see equation (11) for the definition of r_Δ in terms of the mean over-density Δ] is an important parameter to characterize the cluster mass. The lensing fields at the projected radius, $\theta_\Delta = r_\Delta/D_\mathrm{l}$, from the cluster center (D_l is the angular diameter distance up to the cluster) are sensitive to the 2D mass enclosed within a cylinder of radius θ_Δ between an observer and source galaxies. For an isolated NFW halo, the 2D and 3D masses are found to be related as

$$\frac{M_{\mathrm{2D}}^{\mathrm{NFW}}(<\theta_\Delta = r_\Delta/D_\mathrm{l})}{M_{\mathrm{3D}}^{\mathrm{NFW}}(<r_\Delta)} = f(c_\Delta)\, g(x = c_\Delta), \tag{A3}$$

where $f(c) \equiv 1/[\log(1+c) - c/(1+c)]$ and the function $g(x)$ is defined below equation (5) in Golse and Kneib (2002). By using the equation above, the 3D mass can be inferred from the 2D mass that is directly estimated from the lensing observables in a model-independent way. This inversion holds valid if the cluster mass distribution is well represented by an NFW profile (see subsection 4.2 for the detailed discussion).

Appendix 3. Mass Maps

The coherent distortion pattern measured from background galaxy images also allows one to directly reconstruct the two-dimensional map of the (projected) total matter distribution (Kaiser & Squires 1993). The mass density fields between different pixels in the mass map are highly correlated, so the correlations need to be properly taken into account when extracting some useful information from the mass map (e.g., Umetsu & Broadhurst 2008). Even so, the mass map is sometimes useful: comparing the mass map with other wavelength information (member galaxy distribution, X-ray and/or SZ maps, and so on), and inferring the dynamical stages of a cluster from the mass distribution (the presence of substructures and asphericity). For this reason, we show here the mass maps for the individual clusters of our sample, comparing with the number density and luminosity density maps of member galaxies.

In the following mass maps we also show significance contours of the mass density, relative to the $1\,\sigma$ noise level expected from the intrinsic ellipticity noise. Following the method developed in Van Waerbeke (2000) we use the Gaussian smoothing function to quantify the noise level at an arbitrary angular position in the mass map, which is given as

$$\sigma_\kappa^2 = \frac{\sigma_g^2}{2}\frac{1}{2\pi\theta_\mathrm{g}^2\bar{n}_\mathrm{g}}, \tag{A4}$$

where σ_g^2 is the intrinsic ellipticity noise computed in a similar manner as in equation (8): $\sigma_g^2 = \sum_i w_{(i)}^2\sigma_{g(i)}^2/[\sum_i w_{(i)}]^2$ using all of the galaxies used in the mass map reconstruction. The angular scale θ_g is the width of the Gaussian smoothing function, $W(\boldsymbol{\theta}) = 1/(\pi\theta_\mathrm{g}^2)\,\exp(-|\boldsymbol{\theta}|^2/\theta_\mathrm{g}^2)$, and $\bar{n}_\mathrm{g}$ is the mean number density of galaxies over the field. Thus, the noise level in the mass map varies for each cluster, depending on the number density of background galaxies and the smoothing scale used.

For the following mass maps, we use the faint background galaxy sample, because some of our cluster samples do not have color information, so only the background galaxy selection is available for the whole sample, yielding fair comparisons between the mass maps of different clusters. Note that we also show the measured radial profiles of the tangential and its 45° rotated components of the galaxy images for the clusters listed in table 6: the clusters whose lensing distortion profiles are used to constrain the cluster parameters (mass profiles and cluster masses).

References

Adelman-McCarthy, J. K., et al. 2008, ApJS, 175, 297
Baba, H., et al. 2002, in ASP Conf. Ser., 281, Astronomical Data Analysis Software and Systems XI, ed. D. A. Bohlender et al. (San Francisco: ASP), 298
Baltz, E. A., Marshall, P., & Oguri, M. 2007, arXiv:0705.0682
Bardeau, S., Soucail, G., Kneib, J.-P., Czoske, O., Ebeling, H., Hudelot, P., Smail, I., & Smith, G. P. 2007, A&A, 470, 449
Bartelmann, M. 1996, A&A, 313, 697
Bartelmann, M., & Schneider, P. 2001, Phys. Rep., 340, 291
Bergé, J. et al. 2008, MNRAS, 385, 695
Bertin, E., & Arnouts, S. 1996, A&AS, 117, 393
Bertschinger, E. 1985, ApJS, 58, 39
Böhringer, H., et al. 2000, ApJS, 129, 435
Böhringer, H., et al. 2004, A&A, 425, 367
Bridle, S., Kneib, J.-P., Bardeau, S., & Gull, S. 2002, in The Shapes of Galaxies and Their Dark Matter Halos, ed. P. Natarajan (New Jersey: World Scientific), 38
Broadhurst, T., Takada, M., Umetsu, K., Kong, X., Arimoto, N., Chiba, M., & Futamase, T. 2005, ApJ, 619, L143
Broadhurst, T., Umetsu, K., Medezinski, E., Oguri, M., & Rephaeli, Y. 2008, ApJ, 685, L9
Bullock, J. S., Kolatt, T. S., Sigad, Y., Somerville, R. S., Kravtsov, A. V., Klypin, A. A., Primack, J. R., & Dekel, A. 2001, MNRAS, 321, 559

Buote, D. A., Gastaldello, F., Humphrey, P. J., Zappacosta, L., Bullock, J. S., Brighenti, F., & Mathews, W. G. 2007, ApJ, 664, 123
Busha, M. T., Adams, F. C., Wechsler, R. H., & Evrard, A. E. 2003, ApJ, 596, 713
Busha, M. T., Evrard, A. E., Adams, F. C., & Wechsler, R. H. 2005, MNRAS, 363, L11
Clowe, D., et al. 2006, A&A, 451, 395
Clowe, D., Luppino, G. A., Kaiser, N., & Gioia, I. M. 2000, ApJ, 539, 540
Clowe, D., Gonzalez, A., & Markevitch, M. 2004, ApJ, 604, 596
Comerford, J. M., & Natarajan, P. 2007, MNRAS, 379, 190
Corless, V. L., & King, L. J. 2008, MNRAS, 390, 997
Corless, V. L., King, L. J., & Clowe, D. 2009, MNRAS, 393, 1235
Dahle, H., Kaiser, N., Irgens, R. J., Lilje, P. B., & Maddox, S. J. 2002, ApJS, 139, 313
Dodelson, S. 2004, Phys. Rev., D, 70, 023008
Dolag, K., Bartelmann, M., Perrotta, F., Baccigalupi, C., Moscardini, L., Meneghetti, M., & Tormen, G. 2004, A&A, 416, 853
Duffy, A. R., Schaye, J., Kay, S. T., & Dalla Vecchia, C. 2008, MNRAS, 390, L64 (Duffy08)
Ebeling, H., Edge, A. C., Allen, S. W., Crawford, C. S., Fabian, A. C., & Huchra, J. P. 2000, MNRAS, 318, 333
Ebeling, H., Edge, A. C., Böhringer, H., Allen, S. W., Crawford, C. S., Fabian, A. C., Voges, W., & Huchra, J. P. 1998, MNRAS, 301, 881
Erben, T., Van Waerbeke, L., Bertin, E., Mellier, Y., & Schneider, P. 2001, A&A, 366, 717
Fahlman, G., Kaiser, N., Squires, G., & Woods, D. 1994, ApJ, 437, 56
Ferrari, C., Maurogordato, S., Cappi, A., & Benoist, C. 2003, A&A, 399, 813
Fukushige, T., & Makino, J. 2001, ApJ, 557, 533
Gavazzi, R., Fort, B., Mellier, Y., Pelló, R., & Dantel-Fort, M. 2003, A&A, 403, 11
Giovannini, G., Feretti, L., Govoni, F., Murgia, M., & Pizzo, R. 2006, AN, 327, 563
Giovannini, G., Tordi, M., & Feretti, L. 1999, New Astron., 4, 141
Golse, G., & Kneib, J.-P. 2002, A&A, 390, 821
Gunn, J. E., & Gott, J. R., III 1972, ApJ, 176, 1
Haiman, Z., Mohr, J. J., & Holder, G. P. 2001, ApJ, 553, 545
Hamana, T., et al. 2003, ApJ, 597, 98
Hamana, T., Miyazaki, S., Kashikawa, N., Ellis, R. S., Massey, R. J., Refregier, A., & Taylor, J. E. 2008, PASJ, 61, 833
Hamana, T., Takada, M., & Yoshida, N. 2004, MNRAS, 350, 893
Hennawi, J. F., Dalal, N., Bode, P., & Ostriker, J. P. 2007, ApJ, 654, 714
Henry, J. P., Evrard, A. E., Hoekstra, H., Babul, A., & Mahdavi, A. 2009, ApJ, 691, 1307
Heymans, C., et al. 2006, MNRAS, 368, 1323
Hicks, A. K., Ellingson, E., Hoekstra, H., & Yee, H. K. C. 2006, ApJ, 652, 232
Hoekstra, H. 2001, A&A, 370, 743
Hoekstra, H. 2003, MNRAS, 339, 1155
Hoekstra, H. 2007, MNRAS, 379, 317
Hoekstra, H., Franx, M., Kuijken, K., & Squires, G. 1998, ApJ, 504, 636
Hudson, M. J., Gwyn, S. D. J., Dahle, H., & Kaiser, N. 1998, ApJ, 503, 531
Ilbert, O., et al. 2009, ApJ, 690, 1236
Jing, Y. P. 2000, ApJ, 535, 30
Jing, Y. P., & Suto, Y. 2002, ApJ, 574, 538
Johnston, D. E., et al. 2007, arXiv:0709.1159
Jullo, E., & Kneib, J.-P. 2009, MNRAS, 395, 1319
Kaiser, N., & Squires, G. 1993, ApJ, 404, 441
Kaiser, N., Squires, G., & Broadhurst, T. 1995, ApJ, 449, 460 (KSB)
Kempner, J. C., & Sarazin, C. L. 2001, ApJ, 548, 639
Kitayama, T., & Suto, Y. 1997, ApJ, 490, 557
Kneib, J.-P., Ellis, R. S., Smil, I., Couch, W. J., & Sharples, R. M. 1996, ApJ, 471, 643
Kneib, J.-P., Hudelot, P., Ellis, R. S., Treu, T., Smith, G. P., Marshall, P., Czoske, O., Smail, I., & Natarajan, P. 2003, ApJ, 598, 804
Komatsu, E., et al. 2009, ApJS, 180, 330
Kravtsov, A. V., Vikhlinin, A., & Nagai, D. 2006, ApJ, 650, 128
Lima, M., & Hu, W. 2005, Phys. Rev., D, 72, 043006
Limousin, M., et al. 2007, ApJ, 668, 643
Mahdavi, A., Hoekstra, H., Babul, A., & Henry, J. P. 2008, MNRAS, 384, 1567
Mandelbaum, R., Seljak, U., Cool, R. J., Blanton, M., Hirata, C. M., & Brinkmann, J. 2006, MNRAS, 372, 758
Mandelbaum, R., Seljak, U., & Hirata, C. M. 2008, J. Cosmology Astroparticle Phys., 8, 6
Massey, R., et al. 2007, MNRAS, 376, 13
Mazzotta, P., & Giacintucci, S. 2008, ApJ, 675, L9
Mazzotta, P., Markevitch, M., Forman, W. R., Jones, C., Vikhlinin, A., & VanSpeybroeck, L. 2001b, astro-ph/0108476
Mazzotta, P., Markevitch, M., Vikhlinin, A., Forman, W. R., David, L. P., & van Speybroeck, L. 2001a, ApJ, 555, 205
Medezinski, E., et al. 2007, ApJ, 663, 717
Metzler, C. A., White, M., & Loken, C. 2001, ApJ, 547, 560
Miyazaki, S., et al. 2002, PASJ, 54, 833
Miyazaki, S., Hamana, T., Elli, R. S., Kashikawa, N., Massey, R. J., Taylor, J., & Refregier, A. 2007, ApJ, 669, 714
Moore, B., Ghigna, S., Governato, F., Lake, G., Quinn, T., Stadel, J., & Tozzi, P. 1999, ApJ, 524, L19
Nagai, D., Vikhlinin, A., & Kravtsov, A. V. 2007, ApJ, 655, 98
Nakamura, T. T., & Suto, Y. 1997, Prog. Theor. Phys., 97, 49
Narayan, R., & Bartelmann, M. 1996, astro-ph/9606001
Navarro, J. F., et al. 2010, MNRAS, 402, 21
Navarro, J. F., Frenk, C. S., & White, S. D. M. 1996, ApJ, 462, 563
Navarro, J. F., Frenk, C. S., & White, S. D. M. 1997, ApJ, 490, 493
Neto, A. F., et al. 2007, MNRAS, 381, 1450
Oguri, M., et al. 2009, ApJ, 699, 1038
Oguri, M., Takada, M., Umetsu, K., & Broadhurst, T. 2005, ApJ, 632, 841
Oguri, M., Takada, M., Okabe, N., Smith, G. P. 2010, MNRAS in press
Okabe, N., & Umetsu, K. 2008, PASJ, 60, 345
Ouchi, M., et al. 2004, ApJ, 611, 660
Popesso, P., Biviano, A., Böhringer, H., Romaniello, M., & Voges, W. 2005, A&A, 433, 431
Prada, F., Klypin, A. A., Simonneau, E., Betancort-Rijo, J., Patiri, S., Gottlöber, S., & Sanchez-Conde, M. A. 2006, ApJ, 645, 1001
Press, W. H., & Schechter, P. 1974, ApJ, 187, 452
Press, W. H., Teukolsky, S. A., Vetterling, W. T., & Flannery, B. P. 1992, Numerical Recipes in FORTRAN: The Art of Scientific Computing, 2nd ed. (Cambridge: Cambridge University Press)
Richard, J., et al. 2007, ApJ, 662, 781
Richard, J., Pei, L., Limousin, M., Jullo, E., & Kneib, J. P. 2009, A&A, 498, 37
Richard, J., et al. 2010, MNRAS, 404, 325
Rines, K., & Geller, M. J. 2008, AJ, 135, 1837
Sanderson, A. J. R., Edge, A. C., & Smith, G. P. 2009, MNRAS, 398, 1698
Schneider, P. 2006, in Gravitational Lensing: Strong, Weak and Micro, ed. P. Schneider et al. (Berlin: Springer-Verlag), 273
Shaw, L. D., Weller, J., Ostriker, J. P., & Bode, P. 2006, ApJ, 646, 815

Sharon, K., et al. 2005, ApJ, 629, L73
Sheldon, E. S., et al. 2009a, ApJ, 703, 2217
Sheldon, E. S., et al. 2009b, ApJ, 703, 2232
Skrutskie, M. F., et al. 2006, AJ, 131, 1163
Smith, G. P., Edge, A. C., Eke, V. R., Nichol, R. C., Smail, I., & Kneib, J.-P. 2003, ApJ, 590, L79
Smith, G. P., Kneib, J.-P., Ebeling, H., Czoske, O., & Smail, I. 2001, ApJ, 552, 493
Smith, G. P., Kneib, J.-P., Smail, I., Mazzotta, P., Ebeling, H., & Czoske, O. 2005, MNRAS, 359, 417
Smith, G. P., Smail, I., Kneib, J.-P., Davis, C. J., Takamiya, M., Ebeling, H., & Czoske, O. 2002, MNRAS, 333, L16
Smith, G. P., & Taylor, J. E. 2008, ApJ, 682, L73
Takada, M., & Jain, B. 2003, MNRAS, 340, 580
Tomita, K. 1969, Prog. Theor. Phys., 42, 9
Tormen, G., Moscardini, L., & Yoshida, N. 2004, MNRAS, 350, 1397
Umetsu, K., et al. 2009, ApJ, 694, 1643
Umetsu, K., & Broadhurst, T. 2008, ApJ, 684, 177
Van Waerbeke, L. 2000, MNRAS, 313, 524
Venturi, T., Giacintucci, S., Dallacasa, D., Cassano, R., Brunetti, G., Bardelli, S., & Setti, G. 2008, A&A, 484, 327
Vikhlinin, A., et al. 2009a, ApJ, 692, 1033
Vikhlinin, A., et al. 2009b, ApJ, 692, 1060
Vikhlinin, A., Kravtsov, A., Forman, W., Jones, C., Markevitch, M., Murray, S. S., & Van Speybroeck, L. 2006, ApJ, 640, 691
White, M. 2002, ApJS, 143, 241
White, M., & Kochanek, C. S. 2001, ApJ, 560, 539
White, S. D. M., Navarro, J. F., Evrard, A. E., & Frenk, C. S. 1993, Nature, 366, 429
White, M., Van Waerbeke, L., & Mackey, J., 2002, ApJ, 575, 640
Wright, C. O., & Brainerd, T. G. 2000, ApJ, 534, 34
Yagi, M., Kashikawa, N., Sekiguchi, M., Doi, M., Yasuda, N., Shimasaku, K., & Okamura, S. 2002, AJ, 123, 66
Yoshida, N., Springel, V., White, S. D. M., & Tormen, G. 2000, ApJ, 544, L87
Zhang, Y.-Y., Böhringer, H., Finoguenov, A., Ikebe, Y., Matsushita, K., Schuecker, P., Guzzo, L., & Collins, C. A. 2006, A&A, 456, 55
Zhang, Y.-Y., Finoguenov, A., Böhringer, H., Kneib, J.-P., Smith, G. P., Czoske, O., & Soucail, G. 2007, A&A, 467, 437
Zhang, Y.-Y., Finoguenov, A., Böhringer, H., Kneib, J.-P., Smith, G. P., Kneissl, R., Okabe, N., & Dahle, H. 2008, A&A, 482, 451